Enhancement of nitrogen atom density using microwave pulsed discharges : Methodology combining laser-induced fluorescence and collisional-radiative model

Enrico Bisceglia

▶ **To cite this version:**

Enrico Bisceglia. Enhancement of nitrogen atom density using microwave pulsed discharges : Methodology combining laser-induced fluorescence and collisional-radiative model. Micro and nanotechnologies/Microelectronics. Université Paris-Nord - Paris XIII, 2021. English. NNT : 2021PA131046 . tel-03620582

HAL Id: tel-03620582

https://theses.hal.science/tel-03620582v1

Submitted on 26 Mar 2022

HAL is a multi-disciplinary open access archive for the deposit and dissemination of scientific research documents, whether they are published or not. The documents may come from teaching and research institutions in France or abroad, or from public or private research centers.

L'archive ouverte pluridisciplinaire **HAL**, est destinée au dépôt et à la diffusion de documents scientifiques de niveau recherche, publiés ou non, émanant des établissements d'enseignement et de recherche français ou étrangers, des laboratoires publics ou privés.

Thèse présentée par

Enrico BISCEGLIA

Pour obtenir le grade de

Docteur de l'Université Sorbonne Paris Nord

Discipline: Génie des Procédés

30 Juin 2021

Enhancement of nitrogen atom density using microwave pulsed discharges. Methodology combining laser-induced fluorescence and collisional-radiative model.

Jury:

Gérard HENRION	DR CNRS, IJL, Nancy	Rapporteur
Gabi-Daniel STANCU	Professeur, Centrale-Supélec, Gif-sur-Yvette	Rapporteur
Armelle CESSOU	DR CNRS, CORIA, Rouen	Examinateur
Louis LATRASSE	Directeur R&D Plasma, SAIREM, Décines-Charpieu	Examinateur
Savino LONGO	Professeur, Université de Bari, Italie	Examinateur
Jean-Pierre VAN HELDEN	Chercheur, INP-Greifswald, Allemagne	Examinateur
Swaminathan PRASANNA	CR CNRS, LSPM	Co-encadrant
Guillaume LOMBARDI	Professeur, Université Sorbonne Paris Nord	Directeur
Xavier AUBERT	IR CNRS, LSPM	Invité

Thèse préparée au sein du Laboratoire des Sciences des Procédés et des Matériaux

LSPM-CNRS, UPR 3407, Villetaneuse

Co-funded by the Horizon 2020 Framework Programmme of the European

H2020-MSCA-COFUND-2014
Grant Agreement Number: 665850

This project has received funding from the European Union's Horizon 2020 research and innovation program under the Marie Skłodowska-Curie grant agreement No 665850.

Acknowledgements with relative explanations

Why these acknowledgements? – what being a scientist means

This experience covered an important amount of time of my whole life (approximatively 13% of it), during which I have worked as an early stage researcher and have gained enough experience to become a scientist. What is the meaning of being a scientist? Who should a scientist be? The way I would answer these questions is the key to understand the following section.

The most diffused opinions in nowadays society define sciences as "static" topics, eternally valid and providing easily expendable skills in the job market. On the other hand, the knowledge of humanistic subjects, such as history and philosophy, is mostly seen as a non-profitable competence, having no connection nor use within the present society. I feel the necessity of going beyond the classification of different subjects to be taught independently one from another, as many theories can be fully understood when the context into which they were conceived is considered.

The understanding of the aforementioned concepts marks the difference between a "super technician", which I would define as a skilled scientist or engineer in his professional field, and an "enlightened scientist", who is aware of the history and the development of the tools and the protocols he/she is using, of the efforts that were made to reach the discovery of them. In fact, every development in art and in philosophy is generated by a "looking backwards", by a re-discovery, a Renaissance. The same actually happens as well when dealing with the advancing in technology and researchers should be conscious of being heirs of a millennial way of thinking, not simply being unaware actors in this process. As marked at the entry of the Italian studies institute of the Swiss Federal Institute of Technology in Zürich (ETHZ), "*Prima di essere ingegneri voi siete uomini*" (F. De Sanctis, 1856), before being engineers you are men, a sentence that I believe perfectly sums up this spirit of needed curiosity, that makes a scientist being a more complete person. This concept can also be found in a three centuries elder theory proposed by Andreas Libavius in his *Alchymia* (1596), in which the ideal chemist was depicted as citizen well inserted in the society, who "cultivates the *humanitas* in a civil society […]" and "[…] what we shall provide for him is a dwelling suitable for decorous participation in society and living the life of a free man, together with all the appurtenances necessary for such an existence" [1]. These critics were particularly addressed to the Danish astronomer Tycho Brahe, who transferred in 1576 his laboratory and workshop in a fortress on the island of Hven, so that he could devote himself exclusively to science [2].

The decision took by Brahe sounds tremendously actual, as the image of the scientist in nowadays society is mostly negative: there are plenty of examples in modern cinematography in which the villain roles are played by scientists, usually developing relational problems due to their working conditions in well isolated environments. This vision (alongside educational and cultural factors that are not the object of this dissertation and that will not be discussed here) is heavily affecting the appeal of scientific faculties among youngsters in many rich (according to GDP per capita) countries. To give an example, considering the case of Italy, during the last 50 years the percentage of students enrolled in scientific degree courses out of the whole university students dropped down from 47.3% in the '50s to 31.4% in 2000/2001 [3]. This situation is analogous in many other countries, where the governments are spending relevant efforts in treating the image of Science and of Research without collecting the expected success. The only exceptions to these cases are constituted by USA, where the income flux of foreign students is neutralizing this negative trend, and in Japan, where government investments have been consistently directed towards instruction and technology. Nevertheless, in most European countries Science is seen as something too far from everyday life, too hard to be understood and that is therefore demonised and feared: examples to this can be found in the discussions regarding the sphericity of our planet, the existence of chemtrails released by airplanes or in anti-vaccine protests to control the COVID pandemic currently spreading all over the planet. All this can even bring the European cultural scenario of the next generation to be deeply changed, as envisaged by Vincenzo Terreni, president of the Italian association of natural science teachers (ANISN), and can relegate subjects like math and physics to mere "taught sciences" [4].

In the light of these considerations, I firmly believe in the need of a better training to be provided to teachers in schools, as they are the sculptors of the future generations and society. The passions of very young people can be modelled at very early stages, it is necessary to make children curious and to show them the versatility of science in everyday life, by performing easy and practical experiments, retracing the path of the fathers of Science. I also strongly believe in the importance of showing how Science can be correlated and influenced by our cultural background, inevitably influenced by our historical, philosophical and literature heritages. All this would be in line with the etymology of the word "scientist", *i.e. scientia* meaning knowledge, which I would consider not as the understanding of the solely field of investigation, but a more global knowledge and understanding of the society in which the scientist has to be inserted.

Acknowledgements

During these years I had the luck to cooperate and interact with different people. Each of them has played a crucial role in the good ending of this adventure I lived and made me growing up as a better scientist, which is why I tend to show the results presented in the thesis using the first plural person rather than the singular. Moreover, they had all left a deep footprint in my heart, and I will do all my best to keep and preserve them with me as long as possible.

First of all, I thank the jury to have revised and advised on the manuscript.

I also definitely have to thank Khaled, which has always been a reference since I have arrived in France. He has always supported me in the hardest moments I lived during these years and pushed me in keeping going and not giving up. Khaled also taught me how to think as a scientist, how to look at problems with a wider sight and how to find solutions to them when considering similar issues experienced in a different field.

Similar reference role was played by Savino, my mentor during my bachelor and master studies, who created the connection between me and the LSPM and who made all this experience realisable. Savino also had a crucial role in supporting me when the morale was low and in building up my scientific skills.

The people I had cooperated with the closest during these years obviously had the greatest influence on me, namely Guillaume, Prasanna, Xavier and Corinne, and these are those that I thank the most.

Guillaume has been somehow like a father of mine. He was not directly involved in the practical problems that were faced during the research, but he was always following the situation and provided the team with useful advice to fix what was wrong. He was also a central figure for me, who kept a pragmatic approach, usually counterbalancing the excesses of emotional reactions I had in some episodes.

I felt Prasanna being like an elder brother of mine, always ready to support me with very warm advice and being available at any time to provide with help. Moreover, he has been inspiring in many situations due to his hard-working attitude and huge culture, supporting everyone with scientifically-corrected answers on a wide range of topics.

Xavier was like a friend, with whom I shared the joys and the frustrations lived while working (when possible) with the laser, and who taught me from scratch how a laser works, on what physical bases it is built on and how to be rigorous and precise while doing research. It was a real pleasure to chat with him about many different topics, ranging from the role of science in the society to enjoy life as a PhD student in Paris. This was crucial to keep alive my passions and

interests outside working hours, making me living better the whole experience and making me happy in going to the laboratory.

In a similar way as Xavier's, what I admired the most of Corinne was the rigorous approach while performing the experiments and treating the data. Despite being less involved in my PhD thesis supervision, I really have to thank Corinne for the time she spent in the laser room with me, the richness and the effectiveness of the scientific support she provided to me, as well as the morale support when needed.

Among the other employees of the LSPM, everybody would deserve to be mentioned, as I shared pleasant moments with everyone, which made the work being much easier and lighter than how it really was. A special thank goes to Armelle, who had always been helpful (especially on the day of the defence!) and with whom I had spent very pleasant lunch breaks. I also have to thank Ludo, Nico, Noel, Vianney and Ovidiu, for all the technical support and for the numerous funny moments I lived with them during celebrations, breaks or after-work hours. My "office mate" Cathy has also to be thanked, as she has always been helpful when I was looking for support. I also had many and prompt helps from Greg, Natalie, Christelle and Sandrine, who had always been very cheerful with me. I spent very pleasant breaks and train trips with Mamadou, one of few people in the lab with whom I could comment on football matches' results. I am also grateful to Rachid, his help in managing organisational issues has been very important to remove an important component of stress, allowing me to focus more on the research activities.

A major role was also played by my fellows early stage researchers and post-docs, for every coffee, laugh and scientific discussion. Among them, a special thank goes to those with whom I chatted or hung out the most, namely Gautier, Miguel, Lino, Ken, Benjamin, Roland, Ahmed and Nabil. I also want to thank those people who worked with me with the ns-pulsed laser, *i.e.* Mostafa, Hossein and Alice, having the possibility to explain them the functioning of the machine helped me a lot developing communication skills and in understanding better some aspects of the experimental setup. A special mention goes to the more experienced fellows, both in the laser room and not. The experience and passion of Kristaq has been extremely inspiring for me, while the nice words and thoughts of Laurent have also helped me a lot in the final part of the preparation of the manuscript. Outside the laser room, I have to thank Kader, Salima, Catalina, Mary and Mine for the useful hints they provided me over these years.

The tips and advice I have received during my Greifswald staying by Jurgen, Jean-Pierre and Andrei helped me a lot in understanding the meaning of being a researcher and in properly planning experiments. Those two months played an important role in shaping my research skills.

Outside the laboratory, I have to thank those people who had over the years taught me how to work hard and never give up, *i.e.* my swimming coaches Francesco, Dario, Donato, Michele, Dany and Farid. The laughs and the beer had in the water and after trainings also helped a lot, especially those with Julien, Camille, Margot, Tiphaine, Sadok, Matilde, Xavier, Jorge, Fred and Marion.

The support I have received from my family also played a crucial role in the well ending of this experience. The advice of my father in the hardest moments, the shoulder of my mother on which to cry when I needed to, the chats with Giulio (but also with Giulia and Bruno) who helped a lot in going through hard moments…or in enjoying some relax moments during the weekend football league matches! Also, the support and the continuous thoughts I have received from my grandparents, aunts and uncles gave me a lot of strength and will to continue. A special thank must also go to Alessandro, whose drawing skills helped me a lot in preparing some of the figures shown in the thesis.

I have to thank Alessio, his psychological support was crucial and helped me in not giving up during the hardest moments I lived during these years. Thanks to his advice and tips I was able to see this whole experience in a different way and to live it in a less obsessed way.

I also thank the friends of the Fantacalcio, those from Tressette, my Parisian friends Andrea, Mirta, Amalia and Ioanna and my dearest friend Gianluca, for all the laughs and the moral support they provided me with. I also dedicate a thought to my Theramex colleagues, to have been understanding during the final months of the preparation of the manuscript and to support me on the day of the defence, especially the French team members Archana, Lotfi and Magda.

At last, but not the least, I also thank my partner Agata, she had supported and stood next to me in every moment of this experience, especially in those I was particularly unbearable. Agata has been the only PhD student with whom I felt I could freely communicate about my fears, worries and joys. Despite the distance between us, she was the person I felt the closest to me. Alongside Agata, a special thank also goes to her family, who has been always nice and warm to me. Their support during the lockdown period has been very important in helping me to continue working on the project.

References

[1] Martelli M 2011 Greek Alchemists at Work: 'Alchemical Laboratory' in the Greco-Roman Egypt' *Nuncius* **26** 271–311

[2] Hannaway O 1986 Laboratory Design and the Aim of Science: Andreas Libavius versus Tycho Brahe *Isis* **77** 585–610

[3] Castellano R and Punzo G 2010 La crisi delle vocazioni scientifiche in Italia *Sis-Magazine*

[4] Mariano Longo T 2003 La crisi delle vocazioni scientifiche in Francia: un confronto *LE SCIENZE NATURALI NELLA SCUOLA NUMERO SPECIALE ESTATE*

Table of contents

Abstract

The primary objective of this thesis is to understand the mechanisms of dissociation of nitrogen molecule in microwave plasmas under low pressure conditions (1 – 150 Pa), in order to develop an optimized N-atom sources.

The first part of the thesis concerns the development of the methodology for measuring N-atom densities using Two-Photon Absorption Laser Induced Fluorescence in ns regime (ns-TALIF) for highly emissive plasmas, as encountered in this thesis. This methodology has been used to characterize two different microwave sources, namely a magnetized source working between 1 Pa to 20 Pa, and a non-magnetized source working between 20 Pa to 150 Pa, under stationary and pulsed operating modes.

The dissociation under stationary operating conditions is mainly driven by electron-impact processes and the vibrational ladder mechanisms. However, the dissociation is strongly limited by the vibrational translational relaxation process with N-atoms which suppresses the non-equilibrium nature of the vibrational distribution function and makes it difficult to enhance the dissociation of nitrogen.

The later part of the thesis is dedicated to study the enhancement of dissociation using pulsed plasmas. Firstly, unusual sharp changes called Surge and Crash in N-atom densities caused by the conversion between N-atom and its metastables $N(^2D^o)$ and $N(^2P^o)$ during the change in the phase of the MW power were demonstrated. Further, it was shown that pulsed operation of MW plasmas can effectively enhance the dissociation of N-atoms by fine-tuning the different process parameters such as duty cycle, pulsation frequency etc.

Keywords: nitrogen plasma, microwave, TALIF, collisional-radiative model.

Résumé

L'objectif de cette thèse est de contribuer à la compréhension des mécanismes de dissociation de l'azote moléculaire dans des plasmas micro-ondes basse pression (1 - 150 Pa), afin de développer une source optimisée d'atomes d'azote, pour de nombreuses applications.

La première partie du travail concerne le développement de la méthode de mesure de la densité de N à l'aide de fluorescence induite par laser à deux photons, en régime nanoseconde (ns-TALIF). Les plasmas étudiés sont fortement émissifs et la méthode a été adaptée en conséquence. Deux sources micro-ondes différentes ont été caractérisées, *i.e.* une source magnétisée fonctionnant entre 1 Pa et 20 Pa, et une source non magnétisée fonctionnant entre 20 Pa et 150 Pa.

La seconde partie traite de la dissociation de N_2 dans des conditions de fonctionnement continues. La dissociation est gouvernée par des processus d'impact électronique et des mécanismes vibrationnels. Cependant, cette dissociation est fortement limitée par le processus de relaxation vibration-translation avec les atomes d'azote. Ceci a tendance à supprimer le déséquilibre de la fonction de distribution vibrationnelle de N_2, et rend difficile l'augmentation de la dissociation.

La dernière partie est consacrée à l'optimisation de la dissociation en utilisant des plasmas pulsés. Des changements brusques dans les densités de N sont observés durant l'allumage et l'extinction de la puissance microonde. Ceci est dû à la conversion entre N et les métastables $N(^2D^o)$ et $N(^2P^o)$. Le fonctionnement pulsé des plasmas microondes peut nettement améliorer la production de N, en ajustant des paramètres du processus tels que le rapport cyclique et la fréquence de pulsation.

Mots clés : plasmas d'azote, micro-ondes, fluorescence induite par laser, modèle collisionnel-radiatif.

Chapter 1 – Introduction

1.1 Global context

The present manuscript is focused on the quantification of nitrogen and hydrogen atomic densities in reactive plasmas and on the mechanism to generate these two species, with a greater focus devoted on the first one. As it will be explained in this chapter, the dissociation of nitrogen is nowadays (and since a long time) a challenging procedure and it is the core of the collaborative project for which I have been working in. On the other hand, hydrogen plasmas' physico-chemical properties are better known and mastered by the scientific community, with particular regard to the laboratory in which I have carried out my research, LSPM, where this gas has been the object of many studies since the early '90s because of its relevance in diamond synthesis in plasma environments [1–3]. Therefore, in the work described here hydrogen was mostly adopted as an auxiliary gas that worked as calibration and test species and as a precious tool to assemble the experimental setup.

1.2 Etymology and biological importance of nitrogen

The interest of this study lies in the plethora of nowadays applications in which both species are involved, including almost the totality of the activities performed and developed by *Homo Sapiens*. Information related to their very first applications of interest and chemical reactivity lie within the name of these elements. Hydrogen term was coined because of its property to generate water after combustion reaction and the importance of this process is so well recognized that hydrogen name contains a reference to water in every European language. Curiously enough, the ways into which nitrogen is called can be divided into two bigger families, which both highlight two apparently contrasting chemical properties of this element. As explained by Greenwood [4] and Malvaldi [5], this divergence was born in the second half of 18th century, when two French chemists proposed two different names. As a matter of fact, Chaptal, in an analogous way as hydrogen name, proposed *nitrogène* after remarking its indispensable use to generate niter salts (mostly the well-known saltpeter). This name was initially the solely adopted one to define the 7th element of the periodic table in all European languages, and it is still nowadays used in some idioms such as English and Spanish. The other way in which this gas was baptized was *azote* (from shortening of the Greek word *azōtikós*, non-producer of life), suggested by Lavoisier who realized that this gas was not

sustaining the life of both animals and plants. This name is adopted in many languages, such as French, Italian, Polish and German, in the latter even specifying the reason of the antithesis with life (*stickstoff* literally means "substance that suffocates"). Figure 1.1 shows the roots of the most adopted term to name N element in each country across Europe and the Mediterranean basin.

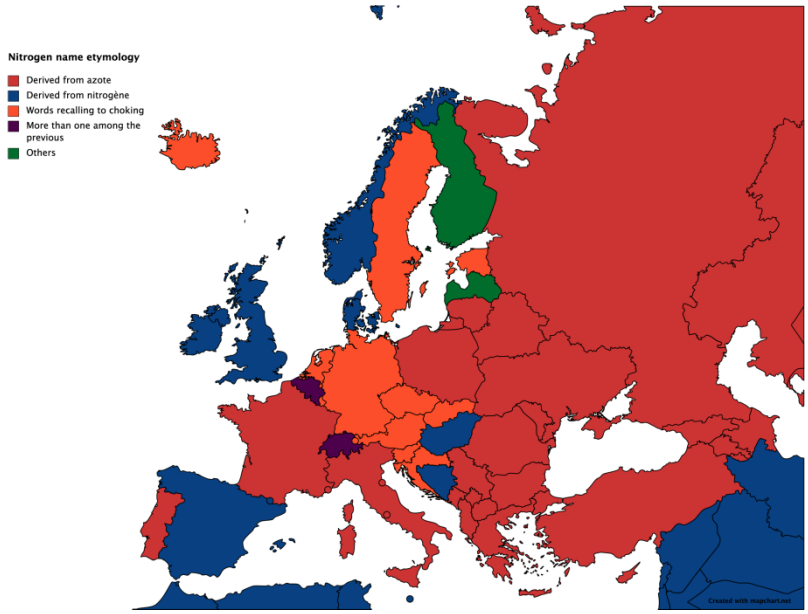

Figure 1.1: Etymology of the main word used in each European country to name N element. Drawing by the author on https://mapchart.net

Despite the absolute need of oxygen to perform both lung and cellular respirations, nitrogen too covers a vital role in sustaining life [6–8], contrary to the suggestion made by Lavoisier. As a matter of fact, the fixation of dinitrogen, *i.e.* the dissociation of molecular nitrogen, is the first step of the nitrogen cycle [6,8,9], the trigger for making this molecule part of a number of transformations to convert the inert molecular form into biologically-relevant compounds. Nitrogen is an unavoidable element in both animals and plants to constitute the proteins and to occupy those sites of the amino acids that define the cells structures, functions and duplications [6,8,10]. Nitrogen cycle, represented in Figure 1.2, describes the most relevant chemical transformations in which nitrogen is involved in atmosphere, biosphere, hydrosphere, and lithosphere [10]. Among these processes, that are mostly carried out by microorganisms, N_2 fixations, highlighted in bold characters, are of main interest in the thesis, as they strictly relate to the dissociation of molecular nitrogen.

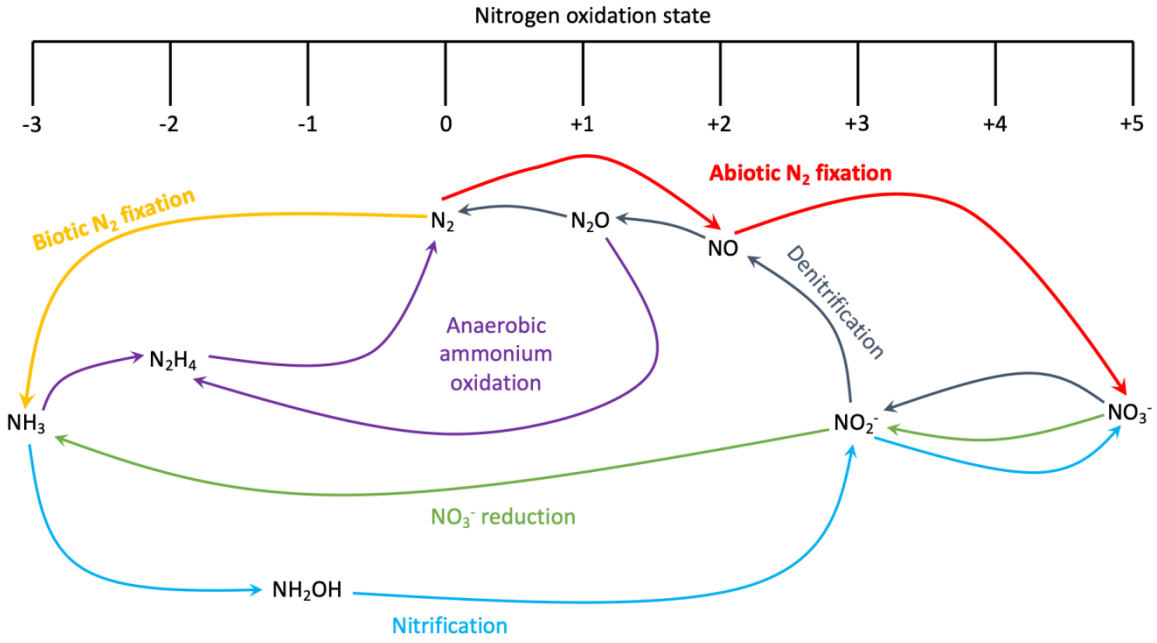

Figure 1.2: Schematic illustration of nitrogen cycle. Drawing by the author, based on [10].

The trigger of all these processes is then the breakage of dinitrogen triple bond [7], featured by a very high energy threshold of 945.41 kJ mol^{-1}, *i.e.* 9.8 eV [4,11]. On the early Earth, this dissociation was exclusively possible to be achieved *via* abiotic fixation phenomena [12]. These processes relies on the energy provided by lightning discharges that dissociate both dioxygen (threshold energy of 493.4 kJ mol^{-1}, *i.e.* 5.1 eV [4]) and dinitrogen molecules. The recombination of the atoms so generated produces nitric oxide and lately nitrates in aqueous environment. These are an essential input among dietary products which benefits blood flow regulation, cell signaling, energetics and tissue responses to hypoxia [13] and are therefore well inserted in nitrogen cycle. Reaction (R1.1) sums up the processes described:

$$\left.\begin{array}{l} N_2 \xrightarrow{\Delta} 2N \\ O_2 \xrightarrow{\Delta} 2O \end{array}\right\} \longrightarrow N + O \rightarrow NO \xrightarrow[H_2O]{} NO_3^- \qquad \text{(R1.1)}$$

A biotic path arose when atomic N supply otherwise provided was not sufficient to fulfil the demand of it [12], with this path nowadays releasing much more atomic N to the cycle than the abiotic production: neglecting the contribution of anthropogenically created N, 100-140 Tg $year^{-1}$ of N are biotically produced while 5 Tg $year^{-1}$ are created by abiotic processes [7]. The main actors of biotic N_2 fixation are prokaryotes belonging to the domain of *Archaea* and *Bacteria* named

diazotrophs, featured by the presence of nitrogenase enzyme that reduces nitrogen to ammonia [7,14,15]. The so produced ammonia and the amino acids generated by smaller organisms are the only available nitrogen inputs for higher animals to build up new nitrogen compounds, while plants, bacteria and fungi can acquire nitrogen from inorganic molecules mostly present in the lithosphere [10]. The synthesis of ammonia is nevertheless a very energetically expensive transformation requiring the dissociation of 16 molecules of adenosine triphosphate (ATP) to allow diazotrophs producing two moles of product from one of N_2 [7]. As a matter of fact, the production of ATP requires the oxidation of organic molecules as sugars and the fixation of each g of N_2 demands a C source consumption ranging from 7 mg to 26 mg, according to the bacterial species and the molecular energy source involved in the process [7]. Such a high cost is not only due to the difficulty in the dissociation of molecular nitrogen, but also in other chemical processes involved in nitrogen fixation, such as the reduction of two protons involved in the reaction, the need to keep the environment anaerobic to avoid the denaturation of the nitrogenase proteins as well as the importance to expel synthetized ammonia that would be toxic for the whole organism [7,14], with the effects on bacteria cells being not clear yet [16]. These inconveniences are usually bypassed by the symbioses of different species, as it happens between the rhizobia bacteria and legumes, so that part of the energy produced by the plant *via* photosynthesis can compensate the energy cost required by the bacterium to perform N_2 fixation [7]. In the light of a drastic increase of world population (estimated to reach 8.3 billion by 2025), a number of researches are then nowadays focused in a deeper understanding of these symbioses mechanisms to increase nitrogen production yield and balance the input in the cycle that sees the accumulation of pollutants due to a too high demand for nitrogen [6–9].

1.3 Non-biological applications of atomic nitrogen and challenges in energy production

Nitrogen is also a central element in a number of other products, having both natural and industrial origins [6]. As a matter of fact, the external membrane of wool fibers, the epicuticle, is composed by the 78% of proteins, mostly keratin [17], whose amino acids are a potential source for the production of nitrogen-based fertilizers [18]. Nitrogen-containing compounds are also present in many drugs. Bisphosphonates containing nitrogen proved to be effective in healing osteoporosis, as they coordinate with Lys200 and Thr201, the latter in particular being bonded to N atom, of the osteoclast farnesyl pyrophosphate synthase preventing proteins prenylation that causes bones degradation [19]. Other examples of nitrogen-containing drugs' efficiency can be also found in

recently-released patents, which highlighted their ability in inhibiting enzymes activity (*e.g.* Rho kinase [20]) and regulating receptors actions (*e.g.* CCR5 [21]). These properties are useful in both preventing and treating a wide amount of illnesses and diseases, as the likes of inflammatory and immunological diseases, infections with human immunodeficiency virus, allergies and in those illnesses that are caused by cells morphologies alterations, as osteoporosis, cancers or cerebral disfunctions [20,21]. The use of nitrogen in industrial applications covers a wide range of sectors, which are mostly dependent on the fixation yield, henceforth called dissociation yield, of the molecular species. As already shown in Figure 1.2, the dissociation process can take place after both reductive and oxidative processes, transforming N_2 molecule in NH_3 or NO_3^- respectively. The oxidative path, which occurs exclusively in inorganic processes, transforms nitrogen into nitrate, whose subsequent conversion into nitrite is carried out by metalloenzymes of diazotrophs [22]. Nitrate reduction releases an important amount of energy that can be used by organisms to sustain life, which makes them suitable candidates as fertilizers. As a matter of fact, this process can either end up with the release of molecular nitrogen in the atmosphere (denitrification) or with the conversion into ammonia in presence of electron donors. Both transformations are strongly exothermic, as can be seen by the Gibbs formation free energy ΔG^0 values of reactions (R1.2) and (R1.3) [10]:

$$2NO_3^- + 2H^+ + 5H_2 \rightarrow N_2 + 6H_2O \qquad \Delta G^0 = -1121 \text{ kJ mol}^{-1} \qquad \text{(R1.2)}$$

$$N(^2D^o) + N_2 \rightarrow N(^4S^o) + N_2 \qquad \Delta G^0 = -591 \text{ kJ mol}^{-1} \qquad \text{(R1.3)}$$

Despite researches are nowadays focusing in a deeper comprehension of biological transformation of nitrogen cycle, the industrial treatment of nitrogen products is by far the preferred way to sustain the needs of world population according to the economic systems most followed in this age, because of much faster kinetics [23]. Since the end of the 19th century, a number of techniques have been developed to effectively perform nitrogen fixation, including the Franck-Caro, Birkeland-Eyde and Haber-Bosch processes [23], synthetizing calcium cyanamide, nitric acid and ammonia respectively. Because of a much higher efficiency and a wider versatility of the final product, the latter was by far the preferred process and it is still nowadays object of studies and improvements to enhance ammonia production [24]. As a matter of fact, the process is nowadays at the base of the sustenance of approximatively 40% of the planet population and it is still used as its dissociation yields of 15-20% [25,26], making it the most efficient way to dissociate nitrogen molecule. Despite these impressive achievements, to which it can be added that this process is regarded by many as one of the greatest inventions of the 20th century, an alternative way of

fixation is still the object of a number of studies, as the optimal experimental conditions of Haber-Bosch process require the presence of high temperatures and pressures (850 K and 2×10^7 Pa) and therefore of high energy expenses (0.48 MJ/mol NH_3), consuming the 2% of world's total energy [23,25,27–30].

1.4 Alternatives to the Haber-Bosch process: recent studies on novel technologies and historical applications of atomic nitrogen

Alongside the biological fixation and the Haber-Bosch process, a novel technique has been taken under consideration to fulfil the need of molecular nitrogen dissociation since the second half of 20^{th} century, based on the formations of plasmas. This was clearly inspired by the abiotic fixation or by the Birkeland-Eyde process, where the presence of sparks, or in a more general way the application of an electrical current through a gas, was assuring the breakage of nitrogen triple bond as well as ionization phenomena [23]. Plasma is a very common state of matter, representing the 99% of visible entities in universe [31], whose natural manifestations observable on the Earth are lightning and the aurora [32]. Plasmas are featured by strongly interacting ionized gas in which ions and electrons have high and almost equal densities (in the bulk region, not in the sheaths where electron densities are much lower). This composition induced Langmuir in naming plasmas as such since this multi-component nature reminded him of the rich blood plasma [33,34]. The natural phenomena in which plasmas occur strongly depend on the physical property of the gas, namely the density and the temperature of electrons, as shown in Figure 1.3, where some representative phenomena are sorted according to these two parameters.

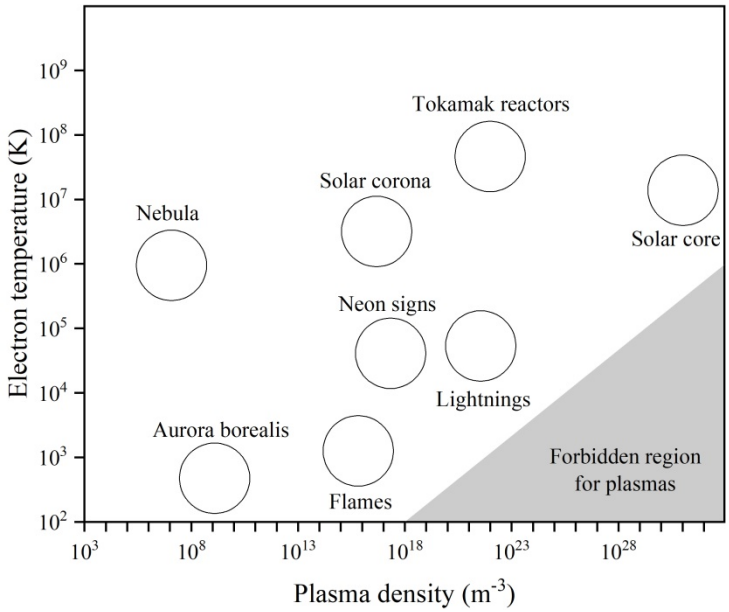

Figure 1.3: Some plasma manifestations with their approximate densities (in m^{-3}) and electron temperatures (in K). Drawing by the author, based on [32,35]

It is clearly visible how plasmas can be discriminated according to their electron temperatures, defining hot and cold plasmas when their temperatures (the concept of temperatures in a plasma will be further discussed in chapter 2) are higher or lower than approximatively 10^5 K and how hot plasmas are essentially confined in outer space. An exception to this is represented by the tokamak reactors, which have been developed since the middle of 20th century or more recently in the frame of the ITER project with the goal of reproducing fusion reactions of hydrogen isotopes as they take place in outer space to power stars. This ambitious project might open new horizons in the energy balances on our planet and the high hopes and resources placed in its success are clearly understandable. Obviously, the high costs and the very long-time scales in which the project is evolving forces researches to be focused on milder and more affordable technologies, namely the cold plasmas. The scientific community has then focused its researches on low temperature plasmas since the first discoveries of them and common efforts and strategies were concretely shared since 2012 when a first roadmap about the topic was released [36], definitely highlighting the novelty and the widely recognized importance of the topic.

Focusing the attention on nitrogen fixation, the plasma approach has been the object of a number of studies to become a concrete candidate to replace Haber-Bosch process. Besides the drastic experimental conditions, the already mentioned high energy costs of the latter are strictly connected with the use of fossil fuels and the consequences of their exploitation. Despite non-renewable energy sources are the only able to provide the necessary high energy densities to sustain the whole process, a side production of 3×10^{11} kg of CO_2 per year [27–30] is not an affordable cost in the light

of a world whose population keeps growing at great pace. This is why sustainable technologies are becoming more attractive to do the job, with the most avant-garde and promising ones relying on metallo-complexes to perform homogeneous catalysis at ambient pressure [28] and the plasmas discharges. The latter in particular, since they essentially require the application of electric energy, which can be produced by eco-friendly technologies such as solar cells and wind [30].

Alongside ammonia synthesis, which is a process involving both hydrogen and nitrogen, molecular plasmas are the main target of a number of nowadays researches, as they can potentially find application in many fields. To give the reader an idea, chemical properties of hydrogen plasmas are well known to suit the needs of deposition of diamond or diamond-like films [37–40], selective etching of materials [37,39], sustained nuclear fusion [41], polycrystalline silicon coatings [37] and many more employments. Similarly, nitrogen plasmas researches have proved to play a central role too in nowadays society. In fact, nitrogen molecule dissociation has been largely studied as its atomic form has been found out to be a crucial component in many applications, such as the in synthesis of dielectric materials [42–44] or of high thermal conductivity materials as hexagonal BN [45–47], surface nitriding [44,48–56], tools sterilization (especially when combining the properties of N_2 molecules and derivative radicals with other species like O_2, CH_4 or H_2) [50,52,54,57–62], thin film deposition, material processing [54,63], exhaust gas abatement [44,53,64–66], astronautics area appliances [67] and more recently into brand new fields that benefited of the use of microwave (MW) plasma sources, *e.g.* in medicine-based applications [23,68,69] or in the field of plasma-assisted combustion [65,70–72]. Other radical and atomic species generated by electron-impact dissociation are currently spread in the use of gas lasers, surface treatments and in electronic devices technologies [73,74].

1.5 Influence of physical properties of plasma discharges on the applications and importance of diagnostics

Beyond the chemical composition of the feeding gas, the different deployment of these discharges is also related with their physical features. The most common anthropogenic plasma is the glow discharge, easily observable in fluorescent lamps, which can be ignited by both direct current (DC) (in an old-fashion short-living configuration) and alternating current (AC) supplies. These discharges have been used for a couple of centuries to study both discharges and atomic and molecular physics in low pressure conditions due to their very simple geometry and they are still used for chemical analysis of gases and solid substrates *via* optical emission spectroscopy (OES) and mass spectrometry (MS) [75].

DC power generators are certainly cheaper than AC ones, but their effectiveness can mostly be observed in low pressure conditions and when external circuit is provided with high resistance [76]; their use is then confined to illumination and gas lasers, while at higher pressure regimes the most noteworthy use is in display panels (60 kPa) [75]. Even if some researches have been addressed to adjust DC supplied dielectric barrier discharges (DBD) in order to improve their performances at higher pressures [75,77,78] on biological substrates [76,77], AC power suppliers conquered the market of industrial applications thanks to their effectiveness in manufacturing inorganic materials, mainly intended as semiconductors. In fact, the main drawback of DC glow discharges is the inevitable sputtering of the cathode, since both the electrodes are in direct contact with the feeding gas and the positively charged ions will be attracted to the negatively charged cathode. Among AC supplied discharges, two notable plasma generation systems are based on the incidence of radiofrequency (RF) or the aforementioned MW on the gas feed, both working in the industrial, scientific and medical (ISM) frequency band. RF plasmas, mostly operative at 13.56 MHz, were developed for analytical intents, *e.g.* inductively coupled plasmas (ICP) torches for mass spectrometry (MS) applications, and industrial purposes related to etching, sputtering and deposition on metal surfaces [79]. During the last two decades, MW sustained plasmas, usually working at 2.45 GHz, proved to be more efficient and more economically attractive than RF ones. These advantages are linked to the higher gas ionization yields achieved and, being this system electrodeless, the non-sputtering of any electrode. Their applications ranges from those already mentioned for RF plasmas to many more, such as in the biomedical [80] and environmental [81] fields and in diamond deposition [82].

Despite such a large number of applications, the sectors in which plasmas have imposed themselves as the best industrial competitor are still limited. To give an idea, microelectronic technology is robustly based on plasma applications, while agriculture and food cycles started experimenting potential benefits of plasmas features only in the last decade [83]. Limited understanding of scientific aspects alongside economic constraints are currently prevailing over the huge environmental benefits provided by low temperature plasmas and their full implementation at industrial scale is only foreseen in a half-century timescale [84]. Alongside agriculture, many other fields are affected by a lack of understanding of the physico-chemical properties of the discharges, and are therefore not eligible yet for industrial applications. Deeper analysis on this matter can remarkably boost industrial applications, whose development has up to now effectively relied on engineering and commercial considerations, while modern age technological advancements demands manipulation of theoretical aspects of science, such as plasma chemistry features [85]. In

this scenario, the development of appropriate diagnostics techniques is therefore a vital aspect of research focused on plasmas.

The main parameters whose understanding can trig this further development are the energy distribution functions of the involved particles (mainly electrons, ions and vibration for molecular species), the kinetic of collision reactions, gas and electron temperatures, density of reactive species or pressure, in order to well predict the effectiveness of the process adopted according to the analysis' goal. As highlighted in [86], plasma features have always been hard to be determined and experimental observations have usually proved to hardly stick with model predictions. Then, the choice of which diagnostics to be applied should be addressed towards the matching the most among what the needs are, especially regarding the parameter aimed to be measured, the targeted precision, the possibility of performing non-invasive analysis and the possibility to best interpret the measured data [84].

1.6 Challenges in atomic nitrogen production

The wide range of applications in which atomic nitrogen is involved and the importance of improving nitrogen dissociation yields relying on sustainable technologies have been widely discussed in this introduction and have been the main reason for the author to perform the presented studies. The interest in these topics made the project receive funding from the European Union's Horizon 2020 research and innovation program under the Marie Skłodowska-Curie grant agreement No 665850, for my PhD salary. Furthermore, this work is embedded in a wider project funded by the "Agence Nationale de la Recherche" (ANR), namely the ANR-16-CE30-0004 project entitled "Atomic Species Production via Electronically excited states in high eNergy density Plasmas" (ASPEN), which is based on the cooperation of three different research institutes, namely the "Laboratoire Énergetique Moleculaire et Macroscopique, Combustion" (EM2C), the "Laboratoire de Physique des Plasmas" (LPP) and the "Laboratoire des Sciences des Procédés et des Matériaux" (LSPM), with the latter being the hosting institution where the investigations here described were carried out. My thesis project is also closely linked to a research collaboration program with the French company SAIREM, provider of advanced MW power supplies for research and industry [87].

Each of the three ANR partners has contributed to the study by analyzing nitrogen discharges generated in specific sources and sustained at different pressures. To proper understand the whole explored conditions, it is necessary to point out that in a generic process of molecular dissociation, the reaction rate r_D depends on the reduced electric field (defined as the ratio between the applied

electric field over the gas number density, usually expressed in Townsend – 1 Td = 10^{-17} V cm^{-2}) E/N, which influence the kinetic constant k and on the densities of electrons and of the generic diatomic gas X_2, n_e and n_{X_2} respectively, as shown in equation (1.1):

$$r_D = k(E/N) \cdot n_e \cdot n_{X_2} \tag{1.1}$$

Plasmas can then be organized according to their pressure regime, recognizing discharges operative at high or low pressures, *i.e.* high or low gas densities n_{X_2}, as represented in Figure 1.4. In the first group, we may definitely identify non-stationary discharges, like Nanosecond Repetitively Pulsed (NRP) ones and Fast Ionization Waves (FIW), which both exhibit high reduced electric field (estimated above 100 Td [88] and between 150 Td and 300 Td [89,90], respectively), *i.e.* high kinetic constants, but over short time ranges of small duty cycles. These two techniques were adopted by two of the partners, in particular EM2C has examined nitrogen discharges in NRP discharges, being operative between 10^2-10^6 Pa [88], and LPP studied FIW potentially working between 2000-10^4 Pa [90,91]. Plasmas can also be ignited using stationary MW microplasma sources, as those presented by Hopwood *et al.* [92], generating discharges extended up to 500 μm in a wide pressure interval ranging between 80 Pa to atmospheric one [93]. These plasmas rely on very high electron densities over large time scales which compensate the moderate applied electric fields to successfully dissociate molecular species. The analysis of these discharges is the object of studies too within the ASPEN project, alongside different microwave microplasmas sources based on the principles described in [94], which presented the structure of coaxial transmission line resonators. A specimen of this source was conceived by [95]. This source generates plasma jets few mm long, but its use in the described work was sharply reduced as stable pressures conditions within the reactor chamber were not assured. This induced the researchers from LSPM in conceiving a new source based on the same principles, capable of sustaining plasma jets between 50 Pa to 10^5 Pa. Another MW plasma source examined in the frame of the ASPEN project is the metallic resonant cavity described by [96–98], largely adopted within the LSPM in the past years to study diamond nanoparticle growth between 2500 Pa and 3×10^4 Pa. Remaining within MW sources, low pressure plasmas can be generated using magnetized sources or not. In the first case, electron confinement and a hot component of the electron population can produce very high electron densities and kinetic constants, while in non-magnetized sources the discharge is characterized with lower electron densities and a significant electron temperature. All the studies presented in this work were performed on this kind of low-pressure microwave plasma sources, namely the magnetized one SAIREM Aura-Wave® and the non-magnetized SAIREM Hi-Wave®, whose functioning and

mechanical features will be detailed in Chapter 2. Figure 1.5 sums up all the sources previously described and involved in the ASPEN project.

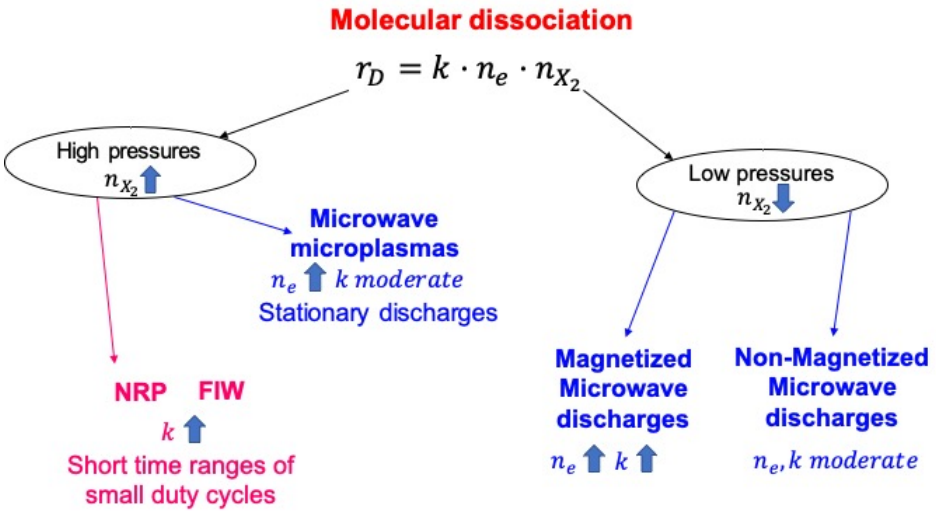

Figure 1.4: Diagram illustrating adopted ways in molecular dissociation within ASPEN project.

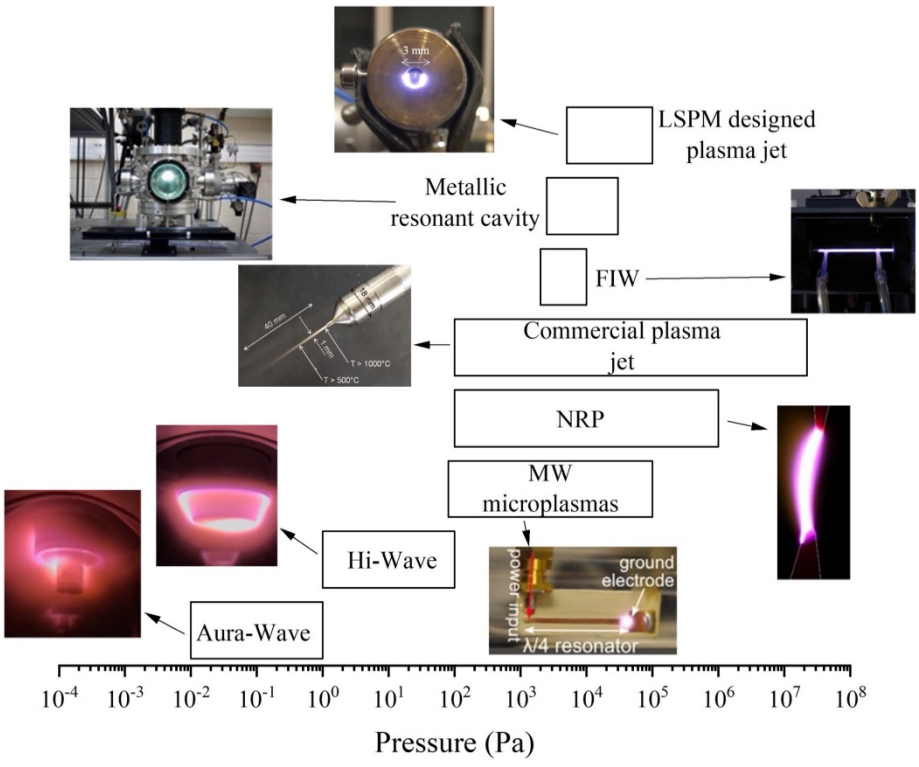

Figure 1.5: Plasma sources investigated in the ASPEN project. These sources, listed in order of increasing operating pressures, are: SAIREM Aura-Wave (10^{-2}-1 Pa) and Hi-Wave (1-10^{2} Pa), MW microplasmas (80-10^{5} Pa) [92,93], NRP discharges (10^{2}-10^{6} Pa) [88], MW plasma flame (10^{2}-2×10^{7} Pa) [95], FIW discharges (2×10^{3}-10^{4} Pa) [89–91], bell jar reactor (2.5×10^{3}-2×10^{4} Pa) [96–98] and toroidal plasma source (5×10^{3}-10^{5} Pa).

The strategy followed to achieve satisfying nitrogen dissociations that brought to the decision of using the aforementioned sources lies in the results obtained in past analysis on oxygen plasmas

[89,99–101], or even air plasmas [72,102]. In these works, atomic oxygen was proved to be produced in high reduced electric field environments, with values between 100 and 400 Td, in a step-wise process that involves the formation of excited molecular nitrogen, as shown in reactions (R1.4) and (R1.5), already proposed by [103]:

$$N_2 + e \rightarrow N_2^* + e \quad \text{(R1.4)}$$

$$N_2^* + O_2 \rightarrow N_2 + 2O \quad \text{(R1.5)}$$

with N_2^* representing many excited states, as $A^3\Sigma_u^+$, $B^3\Pi_g$, $C^3\Pi_u$ (see Figure 1.6).

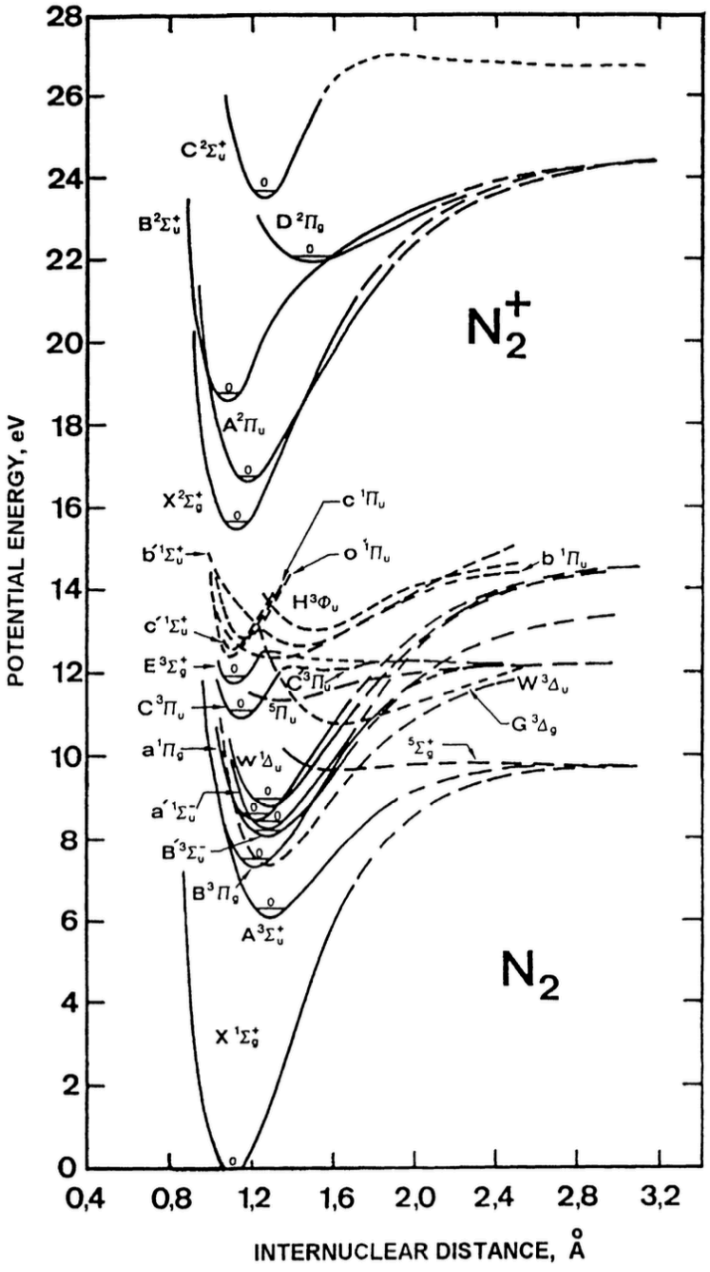

Figure 1.6: Molecular nitrogen and its molecular ion's electronic states and their potential energy [104].

Stancu *et al.* [100] proved that at the peak conduction current in a pulsation cycle, both N_2 second positive system (SPS) temperature and densities $N_2(B^3\Pi_g)$ and $N_2(C^3\Pi_u)$ drastically increase, with the concentrations undergoing to a rapid decay followed by a steep increasing of $O(^3P)$ density, proving the dissociation of molecular species and validating the proposed two-step mechanism. A stronger confirmation of this arrived when the experimental results of [101] describing both rotational temperatures of $N_2(B^3\Pi_g)$ and $N_2(C^3\Pi_u)$ levels and $O(^3P)$ density well matched with the kinetic simulations performed by [105], as shown in Figure 1.7.

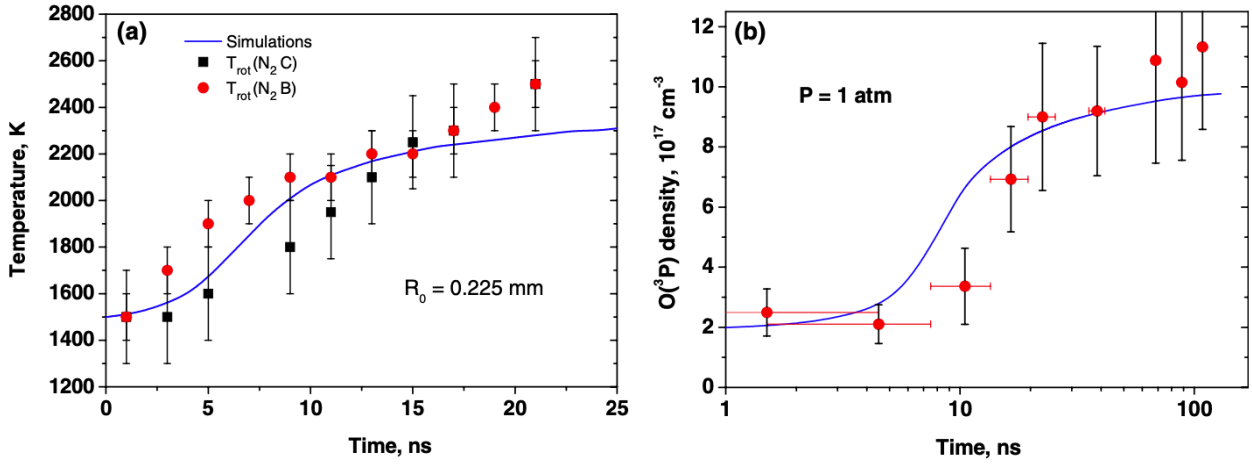

Figure 1.7: Time evolutions of (a) gas temperature and (b) atomic oxygen density estimated by experimental results (symbols) [101] and to simulations (lines) [105]. Figure produced by [101]

Big efforts have been made to better understand nitrogen dissociation kinetic in non-equilibrium plasmas. In particular, many researches were addressed to the impact of vibrational ladder [106–109] and on the efficiency of pulsation [109]. High dissociation yields, reaching even the 70%, were observed in low pressure conditions (few Pa) and in presence of argon [43], while at atmospheric pressure these fractions are extremely low, barely reaching few percentages [110]. Therefore, a deeper understanding of the mechanisms lying behind molecular dissociation is required and different plasmas in a wide range of pressure conditions have to be tested in order to obtain high dissociation yields and absolute atomic concentrations, also consuming the lowest possible amount of power to make a real difference in all the applications of atomic nitrogen.

It was already shown that in low pressure plasmas, main dissociation path follows the reactions shown in reaction (R1.6) [109]:

$$N_2(X^1\Sigma^+_g,v) + e \rightarrow N_2^* + e \rightarrow N(^4S^o) + N(^4S^o,^2D^o,^2P^o) + e \qquad \text{(R1.6)}$$

with N_2^* also including those states with energy greater than dissociation energy, having energies even beyond 12 eV, and $N(^4S^o)$ indicating ground state of nitrogen atoms, while $N(^2D^o)$ and $N(^2P^o)$ are the first excited metastable states. This step-wise mechanism featuring highly energetic states justifies then the need increasing the reduced electric field.

In environments of atmospheric pressures or greater densities, collisions between heavy particles are much more dominant and atomic nitrogen is created following different pathways [111]. One of the main processes sees pooling reactions between excited states followed by collisional dissociation, as shown in reactions (R1.7) and (R1.8).

$$N_2(M) + N_2(N) \rightarrow N_2(M+1) + N_2(N-1) \quad \text{(R1.7)}$$

$$N_2^* + N_2 \rightarrow N(^4S^o) + N(^4S^o) + N_2 \quad \text{(R1.8)}$$

where $N_2(M)$ and $N_2(N)$ stand for two generical excited states of molecular nitrogen (including the possibility of $N_2(M) = N_2(N)$). An iteration of processes as the one shown in reaction (R1.7) will lead to the generation of a N_2^* state that will trig reaction (R1.8) to take place. Ionization processes caused by electron impact reactions can also be a mid-step for atomic nitrogen production, as seen in reaction (R1.9):

$$N_2(X^1\Sigma^+_g,v) + e \rightarrow N_2^+ + e \rightarrow N(^4S^o) + N(^2D^o \quad \text{(R1.9)}$$

The ASPEN project is then aimed at analyzing a wide range of pressures and sources to promote all the proposed mechanisms.

It is worthy to point out that explorative measurements were performed in presence of oxygen by EM2C and LPP laboratories as N_2-O_2 mixtures are usually used in the study of combustion phenomena, for which these two institutions have long-time tradition [99,112].

1.7 Objectives of the thesis

One may distinguish two main effective strategies in N-atom production in non-equilibrium N_2 plasmas. The first strategy is based on the search for discharge conditions that ensure very high reduced effective electric field so as to minimize energy losses in the electron-vibration transfer channel and to maximize the electron energy relaxation on the electron-neutral collisions leading to the excitation of the high lying electronically excited states [101,112,113]. It is in particular of great interest to favor the formation of those states that are pre-dissociative or dissociative in nature or

can lead to dissociation through collisional quenching under the considered pressure conditions [101,112,113]. The second strategy relies on the use of the vibrational pumping mechanism that makes use of an effective excitation of the first few vibrational levels and a subsequent v-v relaxation kinetics that results in significant population of the upper vibrational levels that may easily dissociate through collisions with neutrals [114,115], as summed in reaction (R1.10).

$$N_2(X^1\Sigma^+_g,v) + N_2(X^1\Sigma^+_g,w\text{-}1) \rightarrow N_2(X^1\Sigma^+_g,v\text{-}1) + N_2(X^1\Sigma^+_g,w) \quad \text{(R1.10)}$$

Yet, the so called "vibrational ladder climbing" may be strongly hindered by vibrational-translation energy transfer through either N_2-N_2 (v-$T_{N_2-N_2}$) or N-N_2(v-T_{N-N_2}) collisions that lead to gas heating and effective de-activation of the upper vibrational states, *i.e.*

$$N_2(X^1\Sigma^+_g,v) + N_2 \leftrightarrow N_2(X^1\Sigma^+_g,w) + N_2 \quad \text{(R1.11)}$$

$$N_2(X^1\Sigma^+_g,v) + N \leftrightarrow N_2(X^1\Sigma^+_g,w) + N \quad \text{(R1.12)}$$

especially when the energy difference between two neighboring vibrational levels is of the order of the thermal energy. The vibrational dissociation channel requires an optimal pressure, or gas density, conditions. The pressure should be high enough to insure effective second order kinetics for v-v relaxation process that populates the upper vibrational levels, but not too much large so as to avoid excessive de-excitation of these upper vibrational levels through v-t and v-T processes. The pressure window in which the vibration pumping mechanism takes place therefore depends on the relative ordering between e-v, v-v, v-t and v-T characteristic times.

Therefore, the aim of the thesis is to investigate the effectiveness of different channels of dissociation of nitrogen in a low pressure (1 – 150 Pa) and MW plasmas. For this purpose, we will specifically focus on two plasma sources, namely the magnetized SAIREM® Aura-Wave source based on Electron Cyclotronic Resonance (ECR) and the non-magnetized SAIREM® Hi-Wave source. The ECR source pertains to the conditions where electron impact processes are efficient, while the Hi-Wave source corresponds to a condition where both the electron impact processes as well as vibrational pumping mechanisms are expected to be dominant. Therefore, through this thesis we will try to address the effective dissociation channels under these conditions. Further, we will explore the effectiveness of pulsing of the plasma, which is expected to improve the electron impact processes, towards enhancement of degree of dissociation of nitrogen.

1.8 Table of contents

On these bases, the present work is aimed in studying nitrogen atomic production (hence, dissociation yield of molecular species) in MW plasmas generated by two different sources in low pressure regime, a magnetized one and a non-magnetized one, namely SAIREM Aura-Wave [116,117] and SAIREM Hi-Wave [118]. The results from the latter have also benefitted of 0D simulations to properly study the reactions taking place in the discharge.

The structure of the present work can then be deduced:

- Chapter 2 will discuss briefly the experimental setup that includes the description of MW sources used in this thesis along with the optical diagnostics namely, optical emission spectroscopy (OES) to measure gas temperature and Two photon absorption laser induced fluorescence (TALIF) used for estimating the atomic concentrations.
- Chapter 3 will discuss the methodology used to measure atom-densities from TALIF signals. The chapter will discuss in detail the consequences of strong background emission on the measurement of N-atom densities and the filtering techniques adopted to obtain a fairly good estimate of N-atom densities. The efficacy of the methodology will be demonstrated for Aura-wave source which work at very low pressures (<20 Pa) resulting in very high background and low atomic densities resulting in conditions less ideal for making N-atom measurements.
- Chapter 4 describes the collisional radiative (CR) model developed in the thesis to study the chemical kinetics of MW assisted nitrogen discharges.
- Chapter 5 will present the experimental results of stationary plasma associated with Hi-wave source. The experimental results are complemented with numerical simulations to understand the important mechanisms leading to the dissociation of Nitrogen at low pressures. Further, the degree of dissociation of the Hi-wave source for hydrogen and nitrogen gases would be determined.
- Chapter 6 will present in detail the kinetic mechanisms occurring during the pulsed nitrogen plasma. Especially the chapter will focus on the very fast mechanisms that occur at the instant when the plasma is switched off or switched on. Finally, the chapter will discuss the enhancement of N-atom production in a pulsed nitrogen plasma and determine the important parameters responsible for the same.
- Chapter 7 will outline the future perspectives of research related to atomic sources based on the learning of the present thesis.

Chapter 2 – Experimental setup

2.1 Introduction

The present chapter describes the experimental setup, comprising of the plasma sources, the laser system and the acquisition system for performing Two-photon Absorption Laser Induced Fluorescence (TALIF). The experimental setup is provided in Figure 2.1. Also, details of Optical Emission Spectroscopy (OES) used to measure gas temperature are also presented.

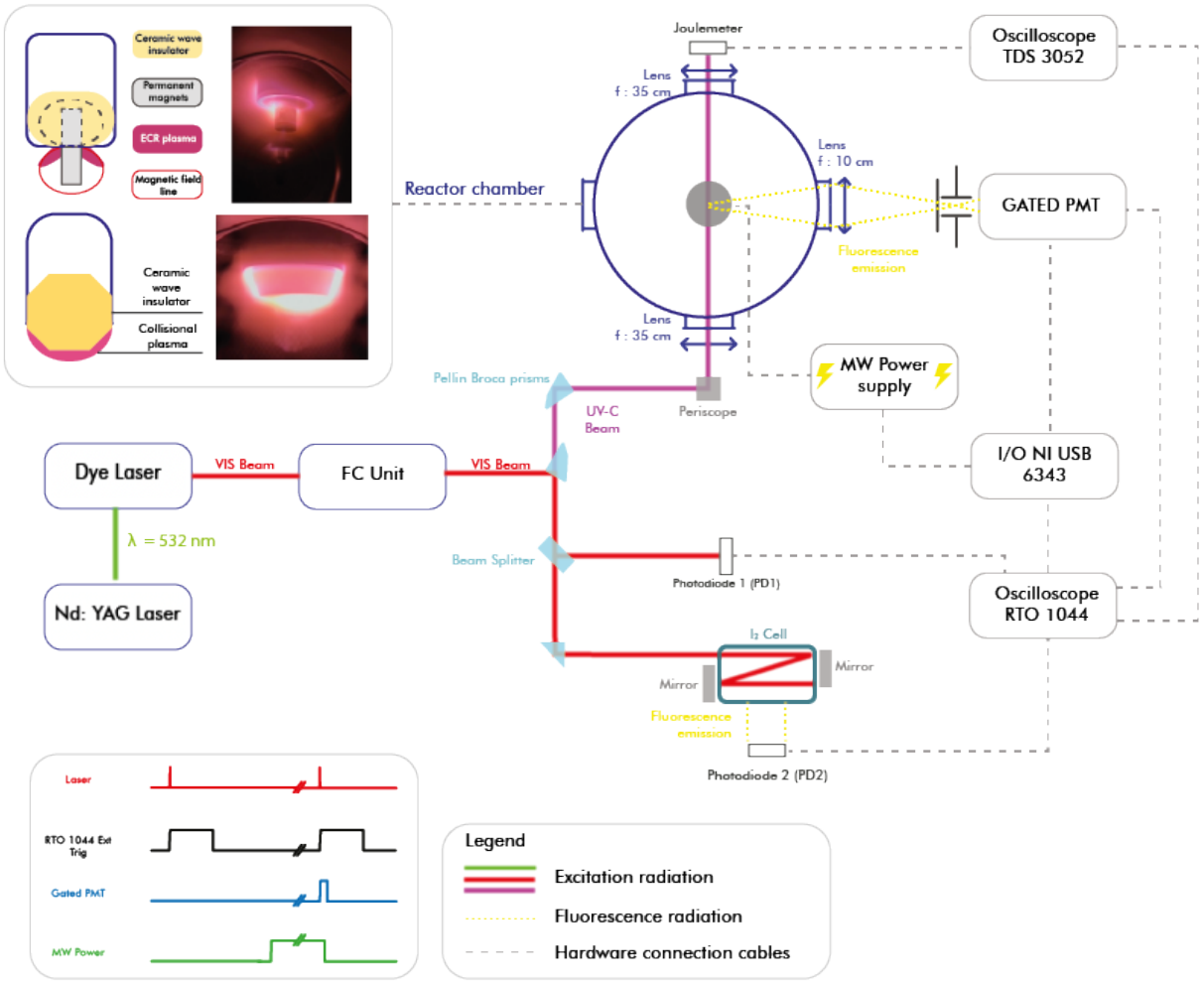

Figure 2.1: Experimental setup adopted to perform atom densities measurements by mean of ns-TALIF [119].

A panoramic view of the main elements of the experimental setup, namely the adopted lasers, the reactor and the MW power supply, is represented in Figure 2.2.

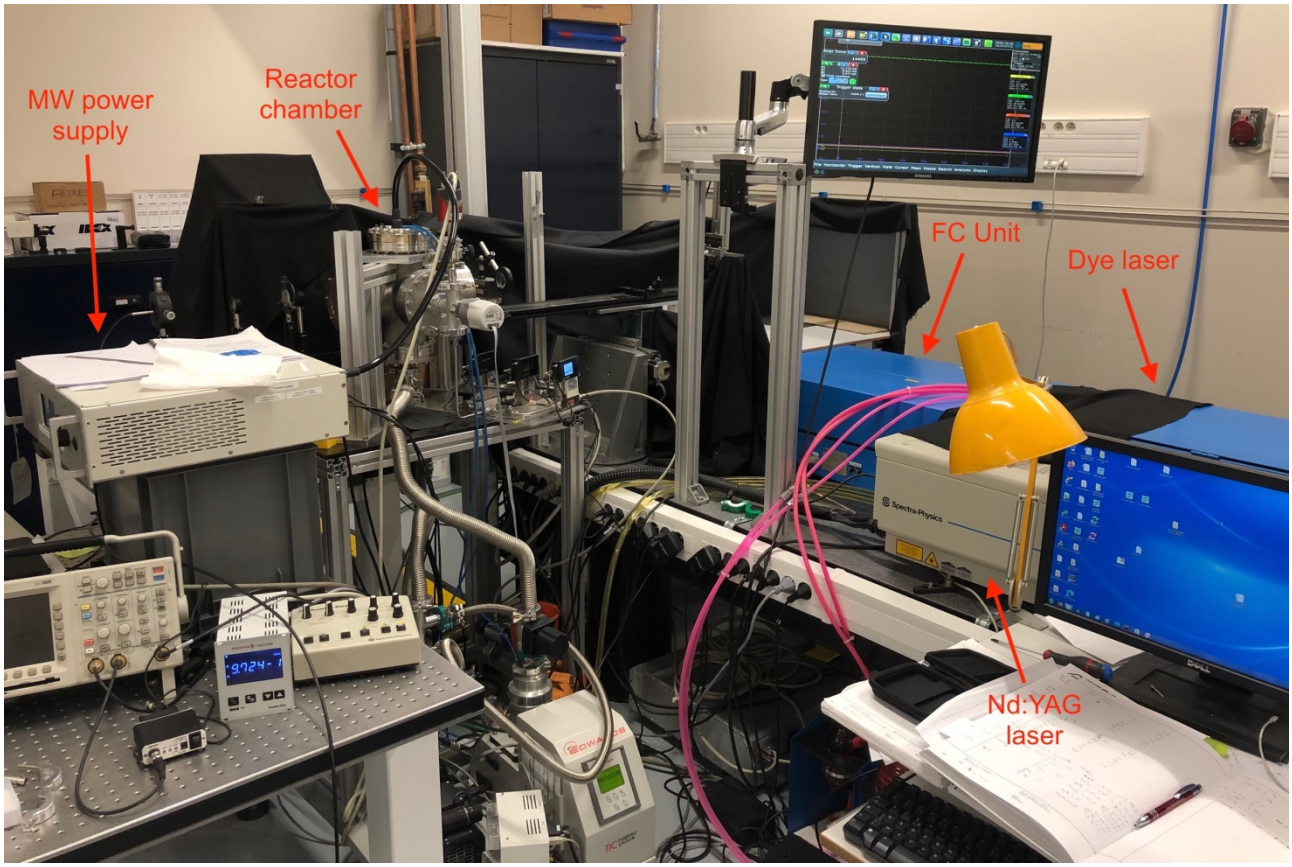

Figure 2.2: Photograph of the experimental setup where the presence of the laser units, the reactor chamber and the MW power supply is highlighted.

The chapter is composed of three main sections, namely (I) section 2.2, which describes the adopted plasma source, (II) section 2.3, devoted on both theoretical and experimental aspects to be followed to properly perform ns-TALIF and (III) section 2.4, focused on the OES technique.

2.2 The plasma sources

The microwave (MW) assisted plasma was generated either using a commercial magnetized source (Sairem Aura-Wave) or non-magnetized plasma source (Sairem Hi-Wave) as detailed in [117].

Aura-Wave is a magnetized source conceived to work in very low-pressure conditions, in the range between 10^{-2} Pa and 1 Pa [116], so that electron cyclotron resonance (ECR) is achieved. The application of a permanent magnetic field makes the gyration frequency of the electrons equal to the frequency of the applied microwaves enabling electrons to reach high threshold energies, promoting enhanced dissociation and ionization phenomena. However, to take full advantage of the ECR regime, the collisional frequencies ν must be much lower than the MW frequency ω_0 [118]. Optimal ratio ν/ω_0 values that would sustain the ECR regime are between 10^{-2} to 10^{-4} [116], which

define the suggested operational pressure between 10^{-2} Pa and 1 Pa. Nevertheless, the plasma source could be operated at higher pressures up to 20 Pa in both nitrogen and hydrogen environments (which overlaps on purpose with the pressure range studied in Hi-Wave plasma generated). In this case, one must expect the ECR regime associated with the source should not be very effective. The schematic of the Aura-Wave source is shown in Figure 2.3. The magnet is placed on the plasma source such that the magnetic field ensuring the ECR regime is directed toward the center of the reactor chamber, thus minimizing the electron losses at the walls. The magnetic field has an intensity of 0.0875 T (875 gauss) and the resulting plasma has a toroidal shape.

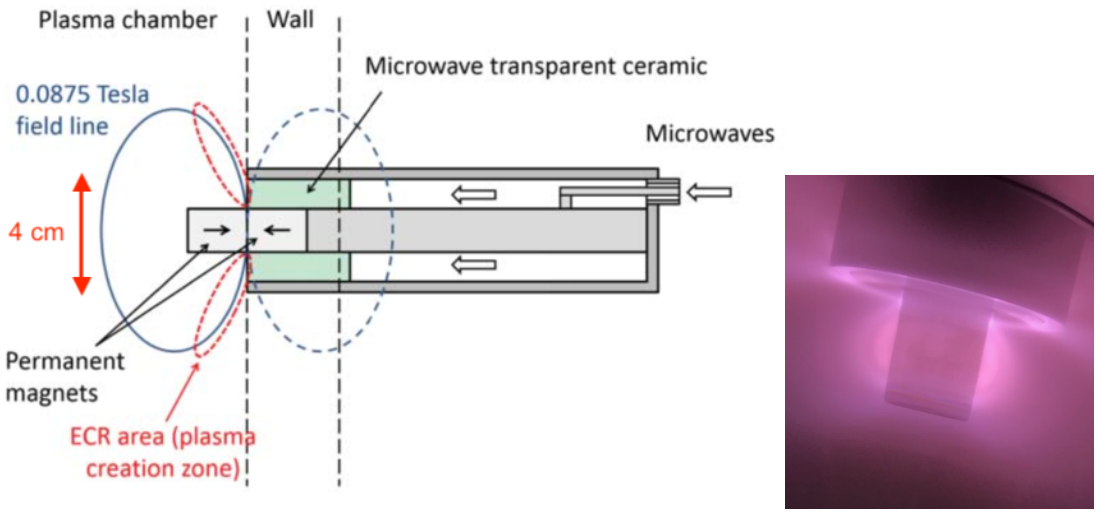

Figure 2.3: Structure of Aura-Wave source and areas of formation of a plasma when ECR conditions are met. Picture published by [117] (left). Photograph of a hydrogen plasma sustained at 5 Pa and 200 W (right).

On the contrary, Hi-Wave is not provided with a magnet and operates at much higher pressure regimes *i.e.* approximatively 1-100 Pa according to the gas [118]. The plasma is collisional and is confined close to the alumina surface. The shape of the alumina surface has been designed to ensure maximum transfer of MW to the plasma volume [117,120]. A schematic of the Hi-wave plasma source is shown in Figure 2.4.

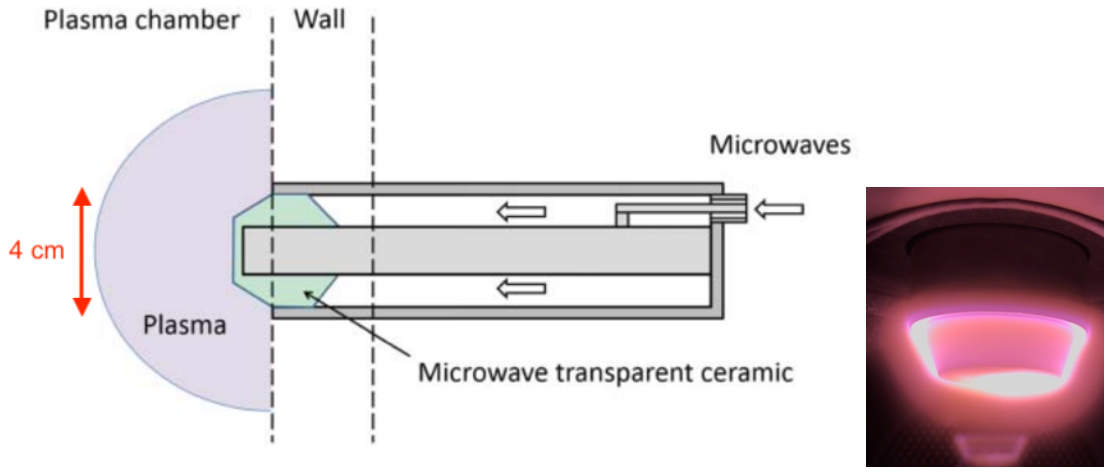

Figure 2.4: Structure of Hi-Wave source and areas of formation of a plasma. Picture published by [117] (left). Photograph of a nitrogen plasma sustained at 5 Pa and 200 W (right)

The MW power is supplied through a coaxial feed from a solid-state MW generator (Sairem GMS 200) that delivers a maximum power of 200 W. The operating MW frequency was tuned between 2.4 and 2.5 GHz in order to achieve optimal impedance matching between the source and the discharge system. The plasma may be operated in both continuous and pulsed modes. The pulsed mode regime makes use of square waveform power pulse and is characterized by the pulse period, the peak power and the duty cycle, which represents the ratio of the high power phase duration to the pulse period. The sequence and the triggering of the pulsations of both acquisition system and plasma is explained in section 2.3.2.

The source was embedded in a 100 mm-diameter stainless-steel 6-way cross and was placed on a specifically designed flange at the top of the cross, as shown in Figure 2.5.

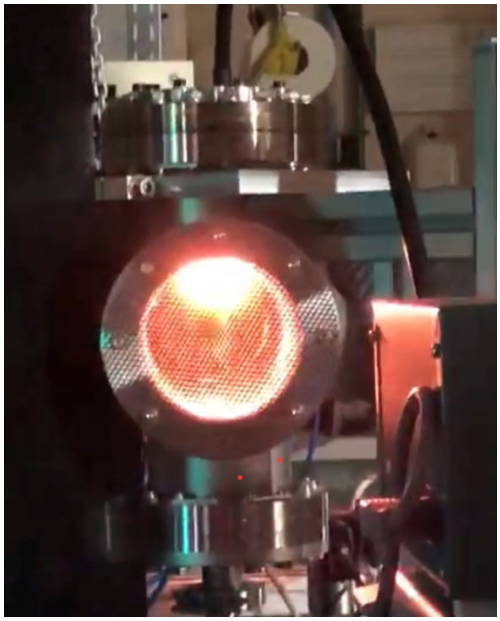

Figure 2.5: 6-way cross reactor where the studied plasma sources were placed.

Three flanges were dedicated to optical viewports. The laser beam enters and exits the plasma reactor through two fused silica viewports 10 mm thick (90% transmission at 205 nm). The fluorescence was collected perpendicularly to the laser beam through a borosilicate viewport. A metallic grid was placed at each viewport in order to prevent MW leakage outside the cavity with a slit 6 cm height and 1 cm width. The vacuum was obtained using a set of turbo-molecular and rotary pumps (Edwards EXT75DX and Pfeiffer Duo 6M), allowing to achieve a residual pressure of 10^{-5} Pa. The working pressure in the chamber was monitored using a capacitive gauge (Pfeiffer CCR363) working in the range 0.133-1333 Pa. The gases were injected in the reactor using mass flow controllers (Bronkhorst EL flow), the flowrate Q being set at 5 sccm. This implies that, being the reactor volume V_R approximatively equal to 3.61×10^{-3} m^3, *i.e.* 3.61 L, the residence time τ of the species can be calculated using the equation (2.1), as proposed by [121,122], to 8.55 s, assuming the pressure p being 20 Pa.

$$\tau = \frac{p \times V_R}{Q} \tag{2.1}$$

2.3 ns-TALIF for atom density measurements

The development of two-photon absorption laser induced fluorescence (TALIF) [123,124] brought many important improvements on the experimental determination of atomic densities in terms of space-and time-resolution, accuracy and flexibility. Two TALIF schemes were proposed for N-atom. The first one makes use of the [$(2p^3)$ $^4S^o$, (3p) $^4D^o$, (3s) ^4P] state system with a two-

photon absorption at 2×211.00 nm and a subsequent fluorescence at 869 nm [124], while the second one makes use of the [($2p^3$) $^4S^o$, (3p) $^4S^o$, (3s) ^4P] system with a two photon absorption at 2×206.67 nm and subsequent fluorescence lines at 742.364, 744.230 and 746.831 nm [125]. The latter system is generally preferred due to larger two-photon absorption cross section and more easily detectable fluorescence, since $\sigma_{207}^{(2)}/\sigma_{211}^{(2)} = 3.5$ [42].

TALIF scheme for hydrogen consists of exciting the ground hydrogen atoms (1s) with a two-photon absorption centred at 205.08 nm to populate the n = 3 excited states 3s and 3d and fluorescence line observed at 656.28 nm (Balmer α) [126–128].

Whatever the adopted system, the use of TALIF to monitor absolute N-atom and H-atom density requires calibration. A straightforward and reliable calibration method for both H-atom and N-atom is based on the use of the TALIF signal of krypton that was proposed two decades ago [127]. In fact, krypton is a rare gas that provides a TALIF system, *i.e.* [($4p^6$)$^1S_0$, 5p'[3/2]$_2$, 5s[3/2]$_1$], with wavelength values for laser-two-photon-absorption (2×204.13 nm) that are close to those of N-atom and H-atom. Thus, the same dye (rhodamine 640) is used for performing TALIF on nitrogen, hydrogen and krypton. The main fluorescent decays of krypton 5p'[3/2]$_2$ state are observed at 826.32 nm and 587.09 nm and, although the radiative decay from 826.32 nm is more prominent than the 587.09 nm, 587.09 has been used to capture the fluorescence signal of krypton. This is mainly due to the possibility of 826.32 nm radiation line containing spurious Kr radiation lines emanating from other excited states of Kr [129]. The TALIF schemes for the three atoms are provided in Figure 2.6.

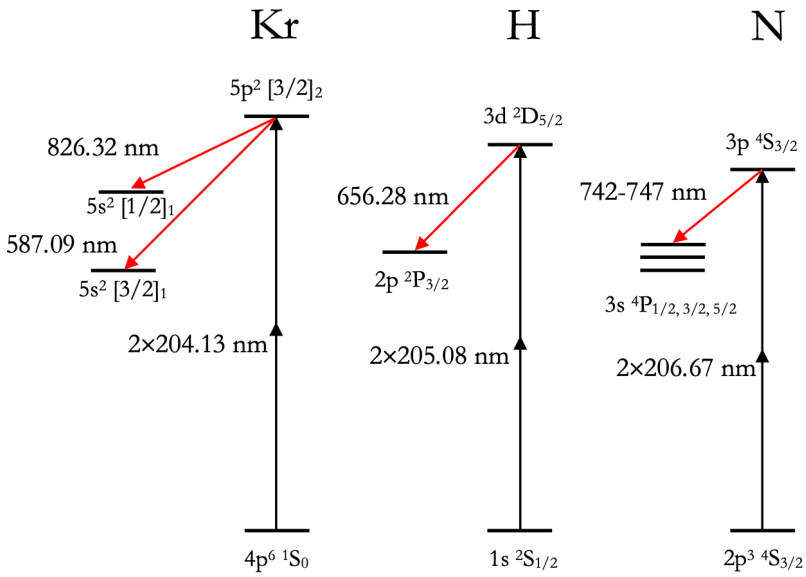

Figure 2.6: Adopted TALIF transition scheme to determine N-atom and H-atom densities

H-atom detection and quantification after two-photon excitation and detection of the Balmer α (656.28 nm) fluorescence emission is a well-established method, adopted since the work of [123] and reported in many recent researches [130–132]. This method was also successfully used for space- and time-resolved measurements of the absolute N-atom density in a variety of moderately-emissive plasmas and plasma post-discharges [44,48,50,51,53,57,58,67,90,133,134]. Surprisingly, despite this large success, achieving N-atom absolute density measurements in highly emissive nitrogen plasmas remains a challenging task from an experimental point of view [53,133,135]. As a matter of fact, N-atom fluorescence takes place inside the emission domain of the first positive system (FPS) of molecular nitrogen as shown in Figure 2.7. It is therefore often very difficult to extract the fluorescence signal in strongly emissive non equilibrium nitrogen-containing plasma [133,135].

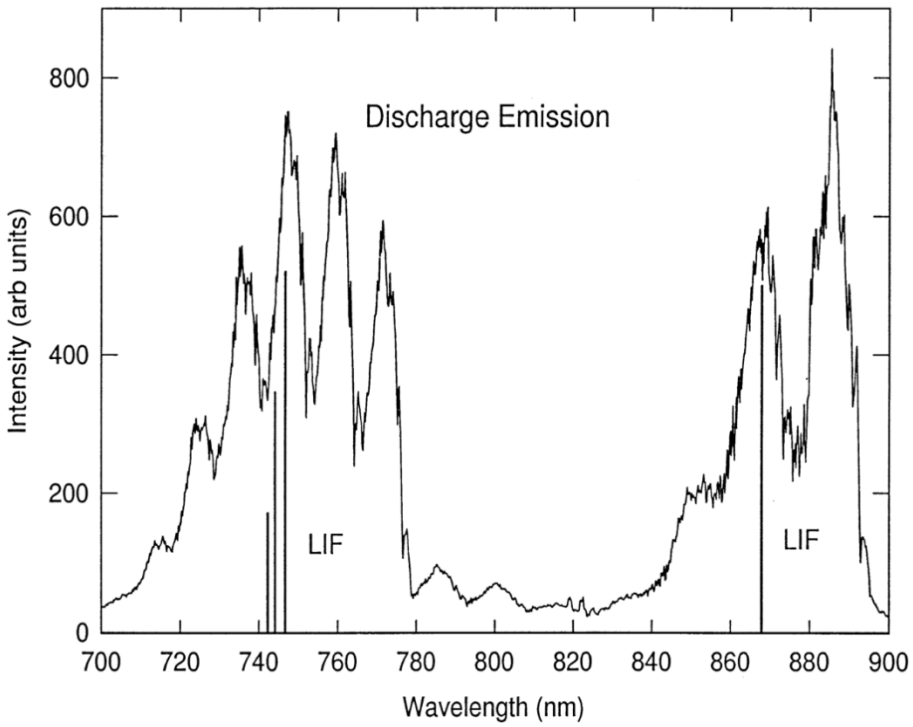

Figure 2.7: N-atom emission lines produced by the transitions illustrated in Figure 2.6 and molecular FPS emission. Figure produced by [42]

Several solutions have been proposed to circumvent this issue. The first type makes use of space and wavelength filtering around the probed volume and the fluorescence wavelength, respectively [42,44,133]. Unfortunately, although this approach usually results in the decrease in the FPS emission, it also leads to the decrease in the fluorescence intensity, which introduces significant uncertainty on the measured value of the N-atom density. The second approach used to get rid of the FPS emission consists of operating the plasma in a pulsed mode and performing TALIF

measurements under post-discharge conditions during the plasma-off phase [44,135,136]. The N-atom absolute density in the plasma-on phase is estimated by time-extrapolating the absolute density-values determined during the post-discharge phase. In this case, it is usually assumed that N-atom depletion mechanism is driven by diffusion/wall recombination process [136]. Beside the uncertainty that may result from the extrapolation procedure, the validity of this approach requires the absence of fast kinetic effects that alter the N-atom density during the early stage of the plasma-off phase. For instance, the authors of reference [53] have clearly shown that the change in the discharge characteristics, electron density and temperature, etc., when transitioning from the plasma-on to the plasma-off phase in pulsed microwave plasma can yield unexpected N-atom time-variations during the very early post-discharge phase. In such a situation the determination of plasma-on N-atom density by extrapolating the time evolution of the atom density during the post-discharge phase is not valid. This shows that direct measurement of N-atom density during the plasma-on phase is still needed for such strongly emissive discharges. The methodology of TALIF measurement of N-atom in strongly emissive plasmas will be treated in detail in chapter 3.

The ns-TALIF diagnostic was carried out using a dye laser pumped by a pulsed Nd:YAG laser, the TALIF signal being acquired with a gated photomultiplier tube. In the following, a detailed description of each component of this setup is given (cf. Figure 2.1).

2.3.1 The laser system

The ns-TALIF spectroscopy was performed using a tunable dye laser (SirahLasertechnik Cobra-Stretch) pumped by the second harmonic of a 500 mJ/pulse Nd:YAG laser (Spectra-Physics Quanta-Ray Lab-Series 170-10). The dye laser beam was subsequently processed by two BBO crystals, which yielded a laser beam linearly polarized with three harmonics that were separated using two fused silica Pellin-Broca prisms. The desired third harmonic that may be tuned between 204 nm and 207 nm was spatially selected by the Pellin-Broca prisms. A typical energy value obtained for this harmonic is 2.5 mJ/pulse. The laser wavelength was systematically calibrated during LIF experiments using an iodine cell. A specimen of iodine fluorescence emission spectrum in a wavelength range close to the N-atom fluorescence one is displayed in Figure 2.8:

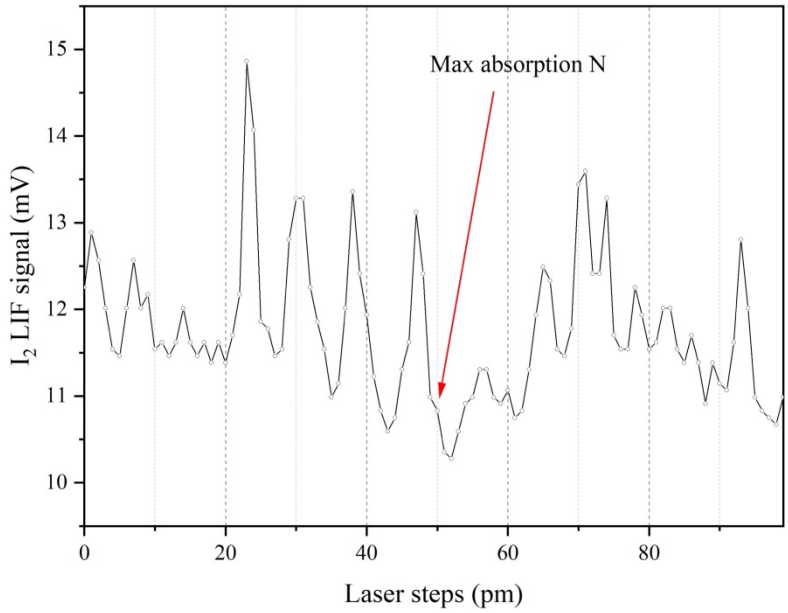

Figure 2.8: Iodine fluorescence spectrum in the wavelength range 619.5 nm to 620.5 nm in order to induce N-atom fluorescence after triplication of the laser frequency [125]. The optimum of N-atom fluorescence is marked by the red arrow.

The obtained pure UV-C radiation was shifted vertically by means of a periscope and then focused with a 35 cm-focal-length lens at the center of the reactor chamber. In order to measure the laser energy, the beam exiting the chamber was collimated and collected with a calorimeter (Coherent J-10MB-LE), which was connected to an oscilloscope (Tektronix TDS 3052, 500 MHz, 5 GS/s).

2.3.2 Fluorescence collection system

One of the difficulties encountered with the investigated discharge is the very high level of the background emission obscuring the relatively weak TALIF signal. The collection of N-atom fluorescence was therefore performed with a photomultiplier tube that allows for gated operations (Hamamatsu H11526-20-NF) and provides a linear regime up to 30 mA current. Furthermore, a focusing lens (f = 10 cm) in a 4f configuration along with a 600 µm slit, and appropriate band-pass filters, were used to limit the probed volume, and the wavelength range to the fluorescence domain, respectively. With this configuration, the amount of background emission collected by the photomultiplier tube is reduced and the TALIF signal-to-noise ratio (S/N) is improved. In this spectral region, the residual background emission corresponds to the FPS emission. This background emission signal of N_2 plasmas will also be referred to as FPS emission in the rest of the thesis.

The performed time-resolved TALIF experiments require the synchronization of the microwave power pulse that ignites the plasma, the laser source that generates the fluorescence and the gated

photomultiplier tube that collects the fluorescence signal. For this purpose, the whole system was triggered using the visible component of the dye laser that was directed to a photodiode (PD1, ThorlabsSM05PD2A) connected to a 4 GHz-20 GS/s oscilloscope (Rohde & Schwartz RTO 1044). This oscilloscope converts the nanosecond signal received from the photodiode to a 1 ms signal that triggers a multifunction I/O device (National Instruments USB 6343, 500 kS/s, 1 MHz). This device generates the triggers for the plasma and the photomultiplier tube.

Actually, for a single TALIF measurement, two laser pulses are needed: the first is to trigger the system and the second is actually needed to generate and monitor the fluorescence signal. Therefore, a delay is imposed between the triggering laser shot and the 5 µs photomultiplier-tube gate so as to capture the whole 400 ns fluorescence signal. Similarly, the delay between the triggering laser shot and the trigger to the microwave is varied so as to explore the temporal evolution of the plasma.

Two different solutions for triggering the plasma were undertaken. In the first, the trigger from the multifunction I/O device is directly used to trigger the plasma directly. This means the plasma pulsation frequency was fixed at 10 Hz, while the duty cycle could be varied (c.f. Figure 2.9).

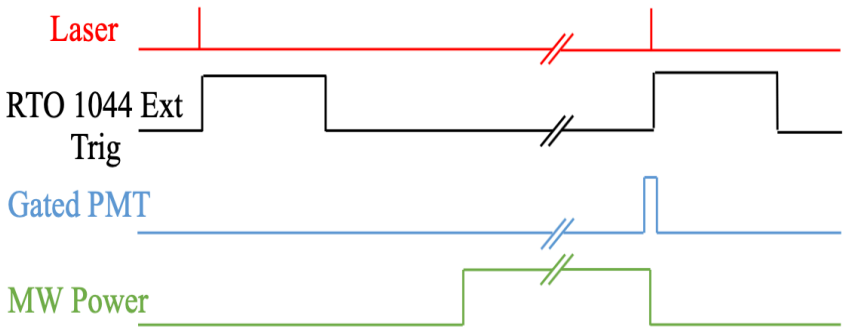

Figure 2.9: Scheme of time delays adopted to synchronize the devices involved in the acquisition of the fluorescence signal in time-resolved experiments.

In the second, a trigger signal from the multifunction I/O device was sent to an intermediate function generator (FG) which is then used to send a trigger signal to the MW generator in burst mode (c.f. Figure 2.10). It is thus possible to send at least one pulse during the period. This solution allowed performing experiments at various pulsation frequency and constant time-average MW power but the duty cycle was fixed at 0.5. Both the methods of triggering have been used to study the effect of duty cycle and pulsation frequency on the plasma parameters.

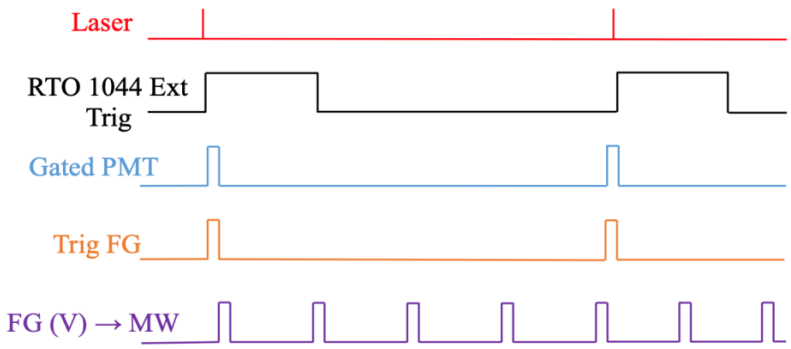

Figure 2.10: Scheme of the fixed delays when the function generator is used to change MW source pulsation frequency.

The control of the whole platform, along with the signal acquisition and data processing was performed using a dedicated LabVIEW™ application.

A typical TALIF experiment performed in the frame of this work consisted in scanning the laser frequency (ν_l) around the 206.67 nm, 205.03 nm and 204.13 nm for N-atom, H-atom and Kr-atom, respectively, and acquiring for each value of ν_l: (i) the time-resolved fluorescence signal $d^2s_f(\nu_l, t)$ recorded during a time-duration *dt* around *t*, i.e. during [*t*-d*t*/2, *t*+d*t*/2], generated by the laser radiation in the frequency range [ν_l-dν_l /2, ν_l+dν_l /2], (ii) the laser pulse energy signal E_l, and (iii) the iodine fluorescence signal used for wavelength calibration.

2.4 Gas temperature measurement

The gas temperature of non-equilibrium plasmas is often estimated using optical emission spectroscopy. Reviews on gas temperature measurement using OES is given in [137,138]. In our experiments, the gas temperature of nitrogen plasmas is measured from the emission emanating from second positive system ($N_2(C^3\Pi_u) \rightarrow N_2(B^3\Pi_g)$, $\Delta\nu = -2$) of N_2 while Fülcher band was used to measure for hydrogen plasmas [139]. The system represented in Figure 2.1 was adjusted to perform gas temperature measurements. In fact, a lenses-collection system was located in place of the joulemeter, so that plasma emission could be channeled into an optical fiber connected to an Acton SpectraPro 2500i spectrometer.

The assumption of rotational equilibrium with the gas temperature ($T_{rot,N_2(C^3\Pi_u)} = T_g$) may be questionable for $N_2(C^3\Pi_u)$ system in some cases. However, under the considered discharge conditions, the $N_2(C^3\Pi_u)$ is predominantly produced by electron-impact excitation of N_2 ground states and lost by radiative de-excitation. The Franck-Condon principle makes the rotational distribution of the ground ($X^1\Sigma^+_g$) and excited ($C^3\Pi_u$) states identical and in thermal equilibrium with gas temperature [137]. Therefore, we can use the rotational temperature of $N_2(C^3\Pi_u)$ system as

a measure of the gas temperature. The rotational temperature inferred from the rotational structure of the emission band varied between 500 K and 850 K in the investigated range of MW power.

Specifically, SPS Δv = -2 with band head at 380.49 nm is used for measuring the gas temperature of nitrogen plasmas. The gas temperature is estimated by overlapping the experimentally obtained spectrum with a synthetic spectrum and minimizing the difference between the two spectrums [140,141]. An in-house code was written to determine the gas temperatures. Figure 2.11 shows a comparison of the synthetic and the experimental spectrums obtained for Aura-wave source at 20 Pa and 200 W.

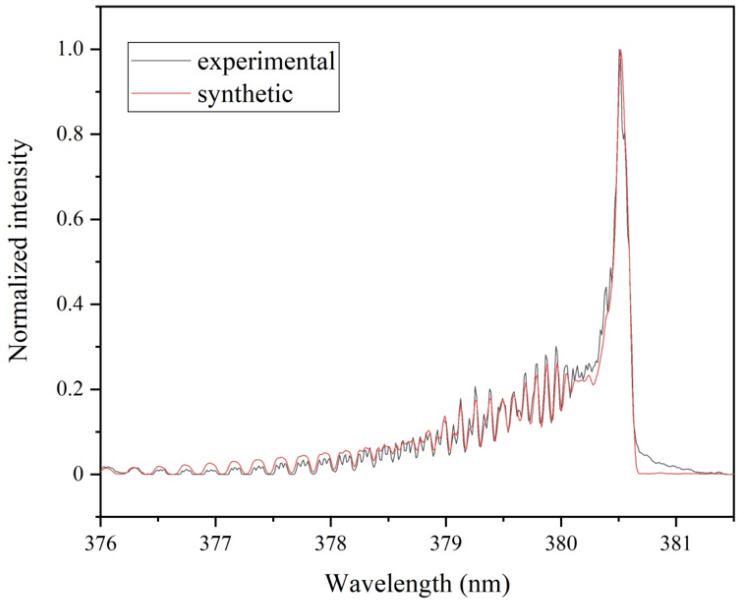

Figure 2.11: Experimental and fitted signals to determine gas temperature from the bandhead of N2-SPS Δv = -2.

Fülcher (2-2)Q band has been chosen to determine the gas temperature for hydrogen plasmas which can be reasonable for the range of pressures used in the current studies [142]. In the conditions of the present study, the excited states of molecular hydrogen are expected to be populated by electron impact from the ground state. It is also assumed that the rotational sublevels of the ground state obey Boltzmann distribution and are under thermal equilibrium with the gas temperature. Thus, the gas temperature estimation follows identification of the relevant peaks of the (2-2)Q band and representing the same on a Boltzmann plot such that:

$$\ln(I) = \frac{1}{T_g} E_{X0N} + const \qquad (2.2)$$

where I and E_{X0N} is the intensity of the transition lines and the corresponding rotational energy of the ground state of hydrogen molecule.

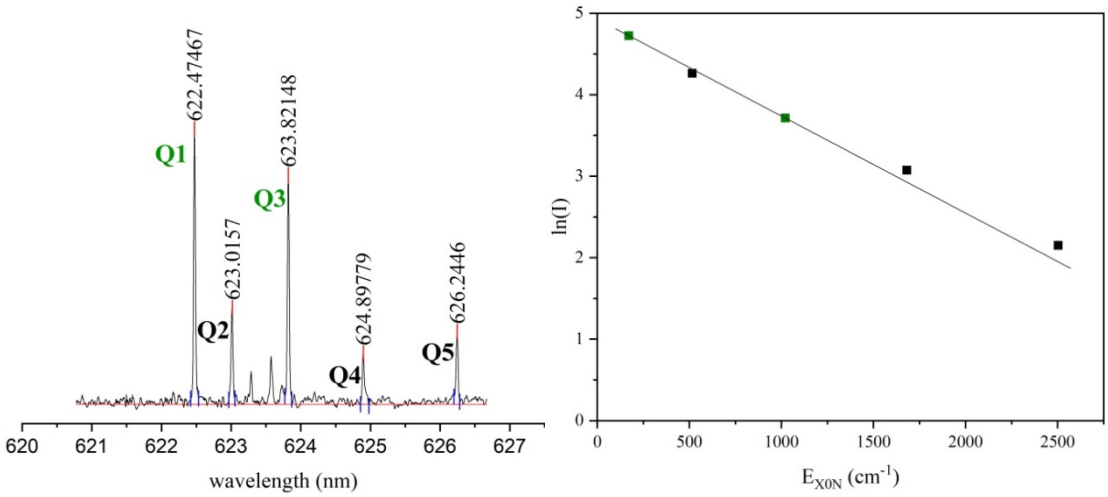

Figure 2.12: Fulcher (2-2)Q peaks used to determine H_2 gas temperature (left) and its corresponding Boltzmann plot (right).

Figure 2.12 shows an example of the experimental spectrum along with the identified peaks belonging to the (2-2)Q branch and its corresponding Boltzmann plot. As detailed in [142], the gas temperatures can be derived considering the ratios of the rovibronic lines Q1 and Q3 when the gas temperature assumes a value lower than 1200 K. This condition was met in all the experiments illustrated in the thesis (see chapter 3 and chapter 5) and the intensities of lines Q1 and Q3 were highlighted in green in Figure 2.12.

2.5 Conclusions

The present chapter illustrated the features of the experimental setup as well as the principles of gas temperature measurements. The structure of the laser setup and the functioning of the MW plasma sources have been thoroughly detailed; in addition, the principles of the adopted diagnostics to perform proper gas temperature measurements, namely the OES, on both nitrogen and hydrogen plasmas have been explained.

Next chapter is focused on the description of TALIF theoretical bases to properly determine atomic densities. Moreover, a detailed explanation about its application on nitrogen plasmas and experimental results obtained using magnetized plasma source are provided.

Chapter 3 - Atomic densities of a strongly emissive plasma using ns-TALIF

3.1 Introduction

As discussed in chapter 2, one of the main roadblocks for measuring N-atom densities by means of TALIF is the presence of the strong emission background at the position of the signal of fluorescence of interest. The objective of this chapter is to present the treatment of fluorescence signals to obtain fairly good estimates of N-atom densities even in a highly emissive plasma. This chapter will also compare the two commonly methods used for determining the atomic densities from the fluorescence signal, so called Full Excitation Method and Peak Excitation Method. In the first method one, the atomic densities are estimated from the temporally and spectrally integrated fluorescence signals of the atoms [65,136,143]. This means that one measurement will require temporal acquisitions from several laser shots, the laser frequency being varied systematically around the peak excitation frequency of the atom. The obtained time integrals must be further spectrally integrated [143]. This method is very robust and accurate, and we refer to it as the Full Excitation Method (FEM) in the thesis. Alternatively, atomic densities can be obtained from a single laser shot with the laser central frequency tuned to the absorption peak [143]. We refer to it as the Peak Excitation Method (PEM) in the thesis. The present chapter will explicitly discuss and investigate the conditions permissible for using the simpler PEM. For the purpose of demonstration of the methods proposed in the chapter, the atomic densities have been measured for Aura-Wave which operating at low pressures and produce extremely strong background with low fluorescence signals. The contents of this chapter have been presented in the paper titled "*Investigation of N(^{4}S) kinetics during the transients of a strongly emissive pulsed ECR plasma using ns-TALIF*" and has been accepted for publication in Plasma Source Science and Technology at the time of writing this thesis.

3.2 N-atom density determination using krypton calibration

We have used the TALIF scheme proposed by Bengtsson et al. [125], represented in Figure 3.1, that shows much larger sensitivity [42] than the very first scheme proposed by Bischel et al. [124]. As explained in chapter 2, the second scheme proposed different excited states involved in the fluorescence decay phenomenon: the state [$(2p^3)\,^4S^o$, $(3p)\,^4D^o$, $(3s)\,^4P$] is reached with a two-photon absorption at 2×211.00 nm and a subsequent fluorescence is recorded at 869 nm. This is generally

less preferred as the two-photon absorption cross section at 211 nm is significantly smaller than the one at 207 nm, *i.e.* $\sigma_{207}^{(2)}/\sigma_{211}^{(2)}$ = 3.5 [42]

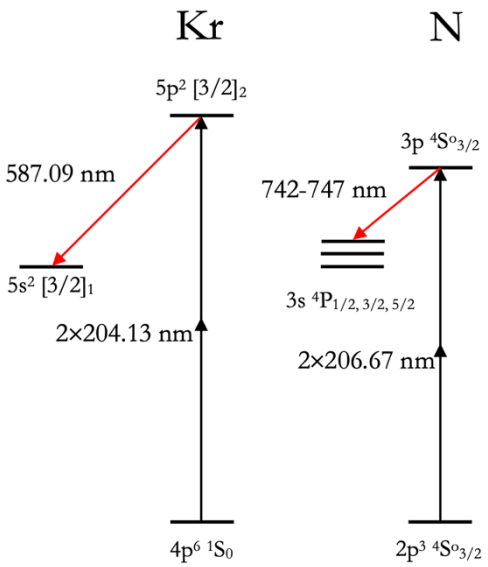

Figure 3.1: Adopted TALIF transition scheme to determine N-atom densities, as proposed by [125]

In this scheme, N-atom in the $(2p^3)^4S_{3/2}^o$ ground state, denoted as N or N($^4S^o$) in the rest of the thesis, absorbs two photons produced by a laser pulse centred around 206.67 nm, and undergoes an electronic transition to the $(3p)^4S_{3/2}^o$ excited state hereafter denoted N*. Assuming that the laser-atom interaction is dominated by the two-photon absorption, the density of the produced excited state is directly related to the offset frequency $\delta\nu_N = 2\nu_l - \nu_N$ where ν_l and ν_N are the laser central frequency and atomic transition frequency of the absorption line respectively. After the laser pulse, N* undergoes a first-order de-excitation through radiative decay and collisional quenching. The radiative de-excitation to the $(3s)^4P_{1/2,\ 3/2,\ 5/2}$ degenerate state produces three fluorescence lines at 742.364, 744.230 and 746.831 nm, which were collected after placing a Semrock® FF01-740/13-25 filter (spectral width 13 nm centered at 740 nm) in front of the photomultiplier. Thus, during the de-excitation phase just after the laser pulse, N* density follows an exponential decay, with a time constant $\tau_{f,N} = \frac{1}{\sum_i A_{i,3p\to3s} + Q}$, $A_{i,3p\to3s}$ being the Einstein coefficient of the i^{th} radiative de-excitation process [144] and Q being the rate of collisional quenching of N*. The resulting incremental time-variation, $d^2n_{N^*}$, during dt, of the instantaneous density of the excited state, $dn_{N^*}(\nu_l \pm d(\nu_l),t)$, resulting from a laser pulse centred at a laser frequency $\nu_l \pm d(\nu_l)$, corresponding to an offset frequency $\delta\nu_N \pm d(\delta\nu_N)$, can be expressed as:

$$d^2 n_{\mathrm{N}^*} = G^{(2)} \sigma_N^{(2)} n_N \left(\frac{I_l T(t)}{h\nu_l} \right)^2 \mathrm{g}(\delta\nu_N)\mathrm{d}(\delta\nu_N)\mathrm{dt} - \frac{dn_{\mathrm{N}^*}(\nu_l \pm \mathrm{d}(\nu_l), \mathrm{t})}{\tau_{f,N}} dt \qquad (3.1)$$

where $G^{(2)}$ and $\sigma_N^{(2)}$are the two-photon statistical factor and the two-photon excitation cross-section (m^4) for the 2p→3p transition at a frequency ν_N, respectively. I_l and $T(t)$ are the radiant exposure ($J \cdot m^{-2}$) and the normalized time profile (s^{-1}) of the laser pulse. $\mathrm{g}(\delta\nu_N)$ is the statistical overlap factor between the nitrogen absorption line and the normalized laser line such that $\int_{-\infty}^{+\infty} \mathrm{g}(\delta\nu_N) d(\delta\nu_N) = 1$. $\mathrm{g}(\delta\nu_N) d(\delta\nu_N)$ also represents the laser energy fraction that is actually used to excite the atoms.

The measured fluorescence signal $d^2 s_{f,N}(\nu_l, t)_N$ during a time interval *dt* is proportional to the instantaneous density of the excited state $dn_{\mathrm{N}^*}(\nu_l \pm \mathrm{d}(\nu_l), t)$:

$$d^2 s_{f,N}(\nu_l, t) = K_g \eta_N \sum_i T_{i,3p\to3s} A_{i,3p\to3s}\, dn_{\mathrm{N}^*} dt \qquad (3.2)$$

with $T_{i,3p\to3s}$the transmittance of the optics used for collecting the fluorescence signal and η_N the sensitivity of the sensor over the spectral width of the fluorescence signal. K_g is a geometrical factor that depends on several optical parameters that are difficult to estimate, *e. g.*, the probed volume, the solid angle of the fluorescence volume subtended on the sensor. This factor shows the same value for N and Kr TALIF systems, which will allow a simplification.

Substituting $dn_{\mathrm{N}^*} dt$ by its value as a function of $d^2 s_{f,N}(\nu_l, t)$ as given by equation (3.2) in equation (3.1), and integrating over a long time period, one gets:

$$\begin{aligned} d\Psi_N &= \frac{\int_{t=0}^{\infty} d^2 s_{f,N}(\nu_l, t)}{\left(\frac{E_l}{h\nu_l}\right)^2} \\ &= \frac{K_g}{S^2} \eta_N \sum_i T_{i,3p\to3s} A_{i,3p\to3s}\, G^{(2)} \sigma_N^{(2)} n_N \tau_{f,N} \mathrm{g}(\delta\nu_N)\mathrm{d}(\delta\nu_N) \int_0^{\infty} T^2(t) dt \end{aligned} \qquad (3.3)$$

where E_l is the laser pulse energy recorded by the photodiode such that $I_l = E_l/S$, S being the cross-section of the laser beam. The factor $d\Psi_N = \frac{\int_{t=0}^{\infty} d^2 s_{f,N}(\nu_l, t)}{(E_l/h\nu_l)^2}$ is the ratio of the number of

detected fluorescence photons during *dt* to the square of the number of laser photons for a laser central frequency in the range $\nu_l \pm \mathrm{d}(\nu_l)$.

In order to eliminate the unknown geometrical factors and to determine N-atom density, krypton is used as calibrating gas as described by Niemi et al. [127]. A factor $d\Psi_{Kr}$ may also be defined for krypton and expressed as function of the Kr-atom density using an equation similar to (3.3):

$$d\Psi_{Kr} = \frac{K_g}{S^2}\eta_{Kr}T_{Kr}A_{Kr5p\rightarrow 5s}G^{(2)}\sigma_{Kr}^{(2)}n_{Kr}\tau_{f,Kr}\mathrm{g}(\delta\nu_{Kr})\mathrm{d}(\delta\nu_{Kr})\int_0^{\infty}T^2(t)dt \qquad (3.4)$$

where $T_{Kr}$and $\eta_{Kr}$are the transmittance and the sensitivity of the photomultiplier tube for the spectral range used for the detection of Kr-atom. $A_{Kr5p\rightarrow 5s}$ is the radiative decay rate for the Kr 5p→5s transition observed [145].

Taking the ratio of equations (3.3) and (3.4) one may express the ground state N-atom density as a function of the known Kr-atom density:

$$n_N = \frac{\eta_{Kr}}{\eta_N}\frac{T_{Kr}A_{Kr5p\rightarrow 5s}}{\sum_i T_{i,3p\rightarrow 3s}A_{i,3p\rightarrow 3s}}\frac{\sigma_{Kr}^{(2)}}{\sigma_N^{(2)}}\frac{\tau_{f,Kr}}{\tau_{f,N}}\frac{\mathrm{d}\Psi_{\mathrm{N}}}{\mathrm{d}\Psi_{\mathrm{Kr}}}\frac{\mathrm{g}(\delta\nu_{Kr})}{\mathrm{g}(\delta\nu_N)}n_{Kr} \qquad (3.5)$$

The ratio of the generalized two-photon excitation cross-sections $\sigma_{Kr}^{(2)}$and $\sigma_N^{(2)}$, for the Kr $(4p^6)^1S_0\rightarrow 5p'[3/2]_2$ and N $(2p^3)^4S_{3/2}^o\rightarrow(3p)^4S_{3/2}^o$, respectively, is taken from [127].

In equation (3.5), all the quantities except the ratio $\frac{\mathrm{g}(\delta\nu_{Kr})}{\mathrm{g}(\delta\nu_N)}$ are readily available after capturing the fluorescence generated by one laser pulse. The estimation of this ratio requires the knowledge of the profiles of the laser beam and the absorption lines of N-atom and Kr-atom. In particular, the absorption line profiles depend on the local plasma conditions and are not always easy to determine from the experiments.

This difficulty is generally circumvented by capturing the fluorescence signals generated by several laser pulses with different central frequency values ν_l around $0.5\nu_A$ $(A = N\ or\ Kr)$ and integrating $\mathrm{d}\Psi_A$ over the whole laser central frequency range. As a matter of fact, if we consider the case of N-atom fluorescence, integrating equation (3.3) over the laser frequency domain yields the following relationship:

$$\int_{\delta\nu=-\infty}^{\infty}\mathrm{d}\Psi_N = \frac{K_g}{S^2}\eta_N\sum_i T_{i,3p\rightarrow 3s}A_{i,3p\rightarrow 3s}\,G^{(2)}\sigma_N^{(2)}n_N\tau_{f,N}\int_0^{\infty}T^2(t)dt \qquad (3.6)$$

Similar equation can be derived for Kr-atom which is:

$$\int_{\delta\nu=-\infty}^{\infty} \mathrm{d}\Psi_{\mathrm{Kr}} = \frac{K_g}{S^2}\eta_{Kr}T_{Kr}A_{Kr5p\to5s}G^{(2)}\sigma_{Kr}^{(2)}n_{Kr}\tau_{f,Kr}\int_0^{\infty} T^2\,(t)dt \tag{3.7}$$

Taking the ratios of equation (3.6) and (3.7), yields the following expression for the N-atom density:

$$n_N = \frac{\eta_{Kr}}{\eta_N}\frac{T_{Kr}A_{Kr5p\to5s}}{\sum_i T_{i,3p\to3s}A_{i,3p\to3s}}\frac{\sigma_{Kr}^{(2)}}{\sigma_N^{(2)}}\frac{\tau_{f,Kr}}{\tau_{f,N}}\frac{\int_{-\infty}^{\infty}\mathrm{d}\Psi_{\mathrm{N}}}{\int_{-\infty}^{\infty}\mathrm{d}\Psi_{\mathrm{Kr}}}n_{Kr} \tag{3.8}$$

Equation (3.8) is therefore an alternative way to determine N-atom densities, in addition to equation (3.5). The different cases in which one formula can be preferred over the other are illustrated in section 3.7.

3.3 H-atom density determination using krypton calibration

The measurement of H-atom densities using ns-TALIF follows the similar principle as that of N-atom. We adopt the TALIF scheme proposed by Bokor et al [123] where the H-atom in the ground state (n = 1) denoted as H in the following, absorbs two photons produced by a laser pulse centred around 205.08 nm, and undergoes electronic transition to 3s and 3d. Following the laser pulse, the excited atom state undergoes de-excitation through radiative decay to H(n = 2) level though the Balmer α (656.28 nm) transition along with collisional quenching. The fluorescence signal is captured by placing a Semrock® FF01-655/15-25 filter centred at 655 nm in front of the photomultiplier. Thus, the H-atom densities can be determined using the methodology presented for N-atom so that

$$n_H = \frac{\eta_{Kr}}{\eta_H}\frac{T_{Kr}A_{Kr5p\to5s}}{T_{H3\to2}A_{H3\to2}}\frac{\sigma_{Kr}^{(2)}}{\sigma_H^{(2)}}\frac{\tau_{f,Kr}}{\tau_{f,H}}\frac{\int_{-\infty}^{\infty}\mathrm{d}\Psi_{\mathrm{H}}}{\int_{-\infty}^{\infty}\mathrm{d}\Psi_{\mathrm{Kr}}}n_{Kr} \tag{3.9}$$

where $T_{H3\to2}$ and $A_{H3\to2}$ are the transmissivity and Einstein coefficient for Balmer alpha transition.

3.4 Evaluating temporal fluorescence signals $\int_{t=0}^{\infty} d^2 s_{f,A}(\nu_l, t)$

The detailed methodology adopted to extract the signal is described in the following. The temporal integral $\int_{t=0}^{\infty} d^2 s_{f,A}(\nu_l, t)$ with A = N, H or Kr and τ_f are directly determined from the analysis of the time-resolved TALIF signal.

As the signal captured by the photomultiplier from N-atom is composed of strong background emission making it difficult to extract the fluorescence signal necessary to calculate the N-atom densities, the methodology has been described for a signal from N TALIF. However, the methodology is also used for H and Kr.

The raw photomultiplier signal for nitrogen was composed of two parts: (I) the time varying N^* atom fluorescence and (II) a plasma background emission identified as the N_2 FPS, *i.e.*, $N_2(B^3\Pi_g \rightarrow A^3\Sigma_u^+, \Delta v = -2)$, that was collected in the 728-750 nm wavelength range (this will be denoted 728-750 nm FPS emission). The overlap between these two components resulted in very poor signal-to-noise ratios, varying between 8 for the (rare) best case and 1.6 for most cases. Therefore, the photomultiplier signal was post-processed using a non-linear least square fit prior to performing the temporal integration. Figure 3.2 shows a typical raw photomultiplier signal along with its non-linear least-square fit. As indicated in Figure 3.2, one may distinguish three different sections of the signal: (I) the N_2 FPS emission region before the initiation of the laser pulse at a time t_0, (II) the fast increase of the fluorescence signal during the laser pulse and (III) the exponential decay with time constant τ_f after time t_1.

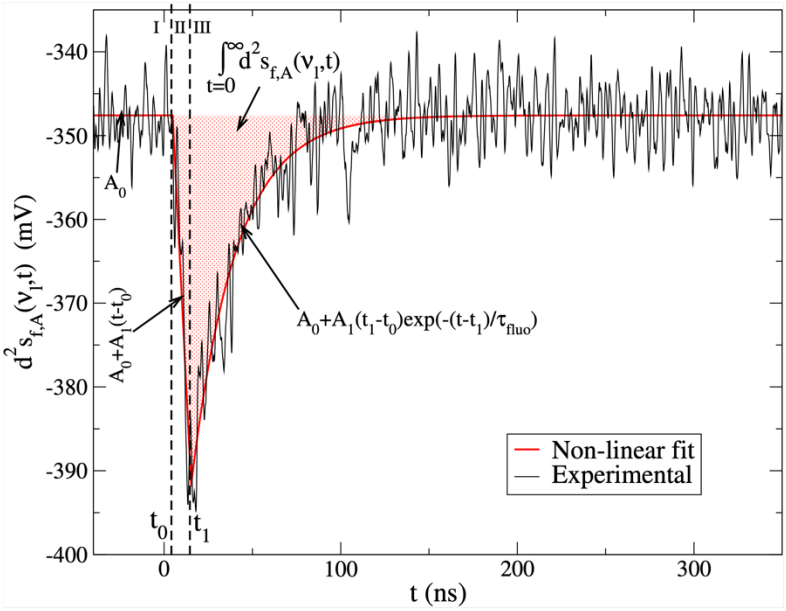

Figure 3.2: A sample raw photomultiplier signal (black line) and the corresponding fit, indicating the three regions, I, II and III, of the signal ((I) the constant plasma background region before the initiation of the laser pulse at a time t_0, (II) the fast increase of the fluorescence signal during the laser pulse and (III) the exponential decay with time constant τ_f after time t_1.) and the corresponding temporal integral of the signal $\int_{t=0}^{\infty} d^2s_{f,A}(\nu_l,t)$.

The fitting function is given by:

$$d^2s_{f,A}(\nu_l,t) = \begin{cases} t < t_0: & A_0 \\ t_0 < t < t_1: & A_0 + A_1(t-t_0) \\ t > t_1: & A_0 + A_1(t_1-t_0)exp\left(-\dfrac{t-t_1}{\tau_f}\right) \end{cases} \tag{3.10}$$

All the parameters of the fit (τ_f, A_0, A_1, t_1 and t_0) are obtained simultaneously. Thus, the time-integrated signal (filtered) for N-atom can be written as follows:

$$\int_{t=0}^{\infty} d^2s_{f,A}(\nu_l,t) = -\tau_f A_1(t_1-t_0) - \frac{1}{2}A_1(t_1-t_0)^2 \tag{3.11}$$

The time-integral signal determined in equation (3.11) corresponds to the term $\int_{-\infty}^{\infty} d\Psi_A$ presented in equation (3.8) and it covers a major role in the calculation of N- or H-atom densities.

3.5 Power dependence

The different standard procedures used to determine atomic densities from TALIF measurements are generally valid only if the laser instantaneous and local power density remains low enough to

avoid additional laser-atom interaction phenomena such as field coupling, photoionization, photodissociation and stimulated emission [65,146]. The analysis of the TALIF signal intensity dependence to the laser energy, i.e., the so called power dependence or power dependence factor [147], makes it possible to check if the experimental conditions ensure a laser-atom interaction dominated by the processes involved in the TALIF scheme. A value of 2 for this factor, i.e., a quadratic regime of excitation, indicates that the fluorescence dominates the laser-atom interaction processes.

From the experimental point of view several methods may be used to vary the laser energy in order to determine the power dependence value. In this work, we tested three approaches. (I) In the first one the energy was changed using a half-wave plate and a Glan-Taylor polarizer. (II) In the second one, the energy was varied by modifying the angle of the second BBO crystal in the dye laser. (III) The third one was based on the use of a set of neutral density (ND) filters.

The method based on Glan-Taylor polarizer is very sensitive to the beam polarization, which resulted in repeatability issue since it was very difficult to inject the laser beam at the exact Brewster angle, *i.e.* the angle at which the whole radiation is transmitted and no reflection can be observed, in the Pellin-Broca prism. As for the second method, the laser shape changed significantly with the energy, which prevented using equation (3.1) that assumes a constant gaussian beam shape. The last method was in fact the most reliable and straight forward. It yielded a power dependence of ~2 for both nitrogen and hydrogen TALIF at 20 Pa and krypton TALIF at 1 Pa over the laser energy range 100-300 μJ (cf. Figure 3.3).

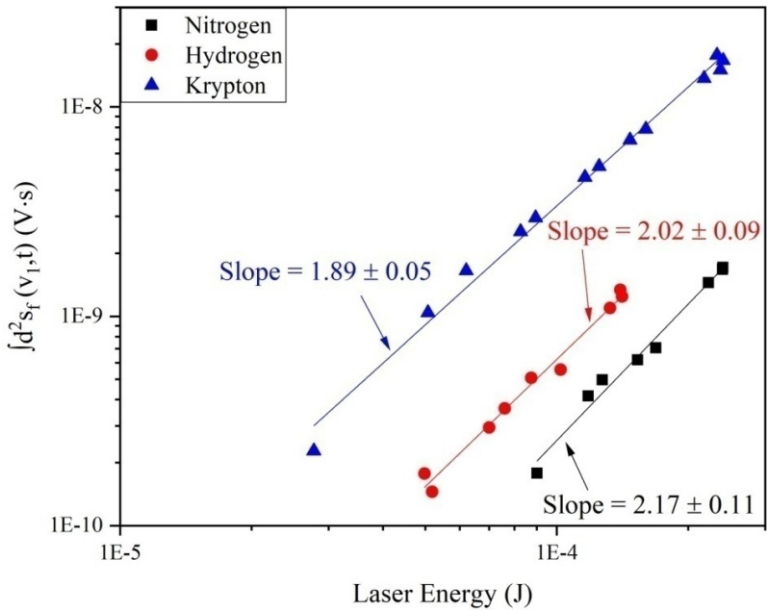

Figure 3.3: Measured variations of the time-integrated TALIF signal intensities as a function of the laser energy for nitrogen, hydrogen and krypton. For these measurements, the laser frequency was set at the peak of absorption ($\nu_l = \nu_A/2$).

3.6 Fluorescence decay time measurements

The determination of atom densities requires determining the ratio of the fluorescence decay times of krypton and nitrogen/hydrogen. The decay time for the krypton fluorescence line intensity at 587.09 nm was measured at 10 Pa and a value of 31.0 ± 1.2 ns was found. In fact under the low pressure conditions considered, the quenching is negligible and the fluorescence decay time is almost equal to the 5p'[3/2]$_2$ radiative lifetime. Using the quenching rate-constant values given in [127] we estimated a value of 31.8 ± 1.3 ns for this radiative lifetime. This value is slightly lower than those previously reported in [127], i.e. 34.1 ns, and [126], i.e. 35.4 ns, but on the other hand slightly larger than the value of 26.9 ns given in [148]. On the average our result seems satisfactory.

The fluorescence decay-time for N(^{4}S^o) atoms was measured at 20 Pa and was found equal to 26.0 ± 1.4 ns for all the investigated plasma conditions (cf. Figure 3.4). Using the rate-constant values given in [42] and [127] for the quenching of N(^{4}S^o) by N_2-molecules, we found a value of 26.2 ± 2 ns for the N((3p)^{4}S^o) radiative life time in agreement with [42,67,125]. As expected, the collisional quenching by N_2-molecules is negligible and does almost not reduce the fluorescence decay-time.

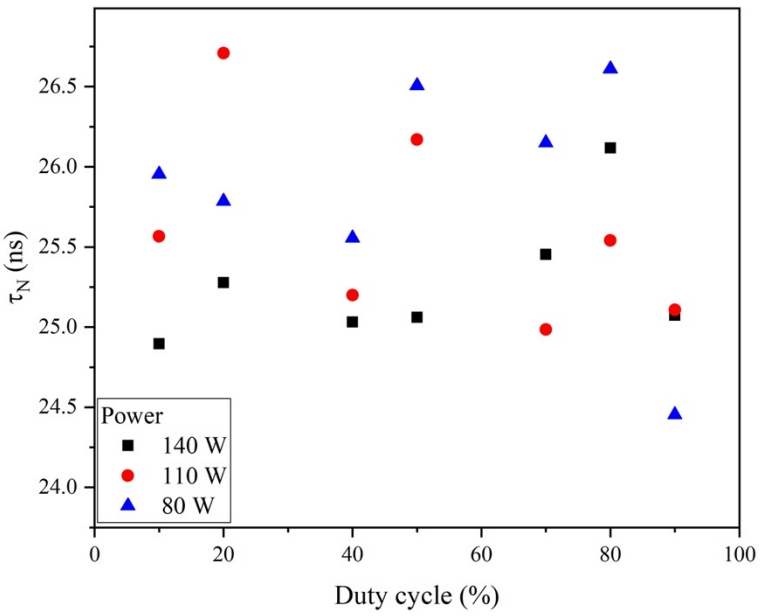

Figure 3.4: Decay time of N-atom fluorescence as a function of the duty cycle for different average input power values. The mean value of N((3p)^{4}S^o) fluorescence decay time estimated from all these data was assessed to be 26 ± 1.4 ns.

Figure 3.5 shows the $\tau_{f,H}$ calculated from the signals collected for hydrogen plasmas generated by Aura-Wave as a function of pressure. $\tau_{f,H}$ at 1 Pa and 2 Pa is around 14 ns and remain constant around 10 ns at higher pressure. The saturation of decay constant at high pressures occurs as the

fluorescence decay is smaller than the time width of the ns-laser pulse. The decay constant $\tau_{f,H}$ can be determined experimentally provided $\tau_{f,H}$ is much larger than the time width of the ns-laser pulse. One may have to use picosecond or femtosecond laser pulses along with a photomultiplier having similar temporal response in order to obtain a reliable estimate of $\tau_{f,H}$ from the experiments [88,149].

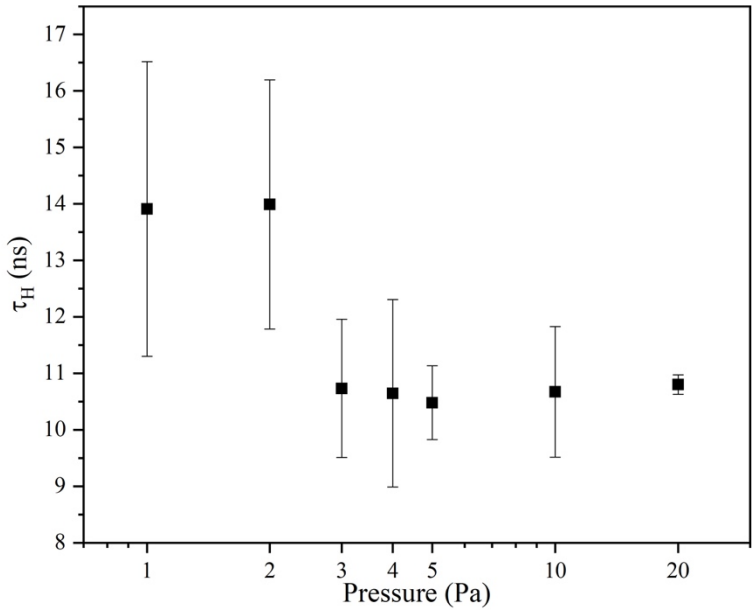

Figure 3.5: Calculated $\tau_{f,H}$ from signals generated by Aura-Wave source in different pressure conditions

Even if the LSPM owned recently a ps TALIF setup, it was not within the scope of this work to realize this kind of decay-time measurements. Instead, $\tau_{f,H}$ has been estimated using kinetic models for the excited states of 3p and 3d. There can be two possible kinetics schemes available to describe the depletion of states 3p and 3d [131]: (I) the isolated scheme and (II) fully mixed scheme. Figure 3.6 illustrates the states of H-atoms involved in these mechanisms. In general, the actual mode of kinetic scheme should lie between the two asymptotic cases and would require a detailed state to state model to determine the different mixing ratios of the n=3 states as a function of temperature and pressure.

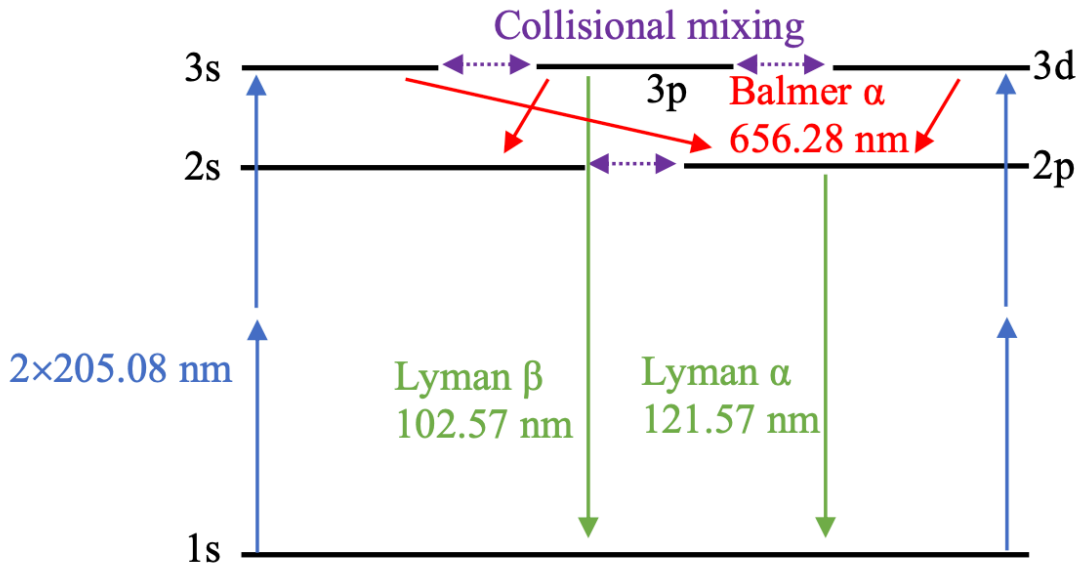

Figure 3.6: Transitions occurring to H-atoms after two-photon excitation.

The first scheme assumes that the states 3p and 3d remain isolated and the respective states deplete through radiative decay and collisional quenching. As the two-photon cross-section of 1s→3d transition are much larger than 1s→3p transition, the populations of 3d is expected to be about 85% of the n = 3 states. Moreover, the radiative decay time for 3p→2s and 3d→2p transitions are 159 ns and 15 ns [131] respectively.

The second kinetic scheme considers perfect mixing of the 3s, 3p and 3d states so that the population distribution of the n = 3 states is defined by their statistical weights. Additionally, one would have to consider the strongly emissive Lyman beta transition from 3p to ground state ($A = 1.67\times10^{-8}$ s^{-1} or decay time of 5.981 ns [150]). For the pressures (1-100 Pa) and the dimensions of the laser volume (~500 μm), this radiation is expected to be optically thin. Assuming that self-absorption is zero for the Lyman beta transition, the effective radiative decay time of such a transition is equal to 10.02 ns [150].

For both the kinetic schemes, the main mode of collisional quenching of n=3 states would be through collisions with hydrogen molecules ($\sigma = 6\times10^{-15}$ cm^2 [130]). As the degree of dissociation of H_2 for the pressure conditions is expected to be small, the collisional quenching by atomic hydrogen can be neglected.

Table 3.1 tabulates the fluorescence decay calculated by the two schemes as a function of pressure at a temperature of 450 K (Figure 3.12 shows the temperature measured for hydrogen plasma for a similar source). The fluorescence decay constants observed in the experiments are in a better agreement with fully mixed kinetic scheme, with the exception of 1 Pa and 2 Pa cases in which intermediate decay constants between the two schemes are observed. It is interesting to note

that the collisional time scales become important only for pressures greater than 100 Pa for both kinetic scheme 1 and scheme 2.

Table 3.1: Fluorescence decay times in ns calculated for the two considered schemes at different pressure and at a constant temperature of 450 K

Pressure (Pa)	Scheme non-mixed (ns)	Scheme fully-mixed (ns)
1	17.19	9.98
2	17.09	9.95
5	16.80	9.85
10	16.34	9.69
20	15.50	9.39
50	13.41	8.58
100	10.95	7.50
150	9.26	6.66

As the effective fluorescence decay would lie between these two extreme kinetic schemes, we assume in this work the effective fluorescence decay time to be 10 ns for all the conditions except at 1 Pa and 2 Pa where the measurement of $\tau_{f,H}$ was possible. Such an approximation is reasonable, considering the large uncertainties of the different parameters involved in the calculation of H-atom densities.

3.7 Spectral integration of TALIF signals $\int_{\delta\nu_N=-\infty}^{\infty} d\Psi_N$

Equation (3.8) and (3.9) for N-atom and H-atom densities respectively, referred to as **full excitation method** (FEM) in the thesis, is widely used in the literature to determine atom densities by TALIF experiments [39,48,50,52,90,127,128,149]. It implicitly captures the overlap factor without any assumption.

$\int_{\delta\nu_N=-\infty}^{\infty} d\Psi_N$ is determined from the laser excitation spectral profile of $d\Psi_N(\delta\nu_N)$. For this purpose, the fitting procedure was applied to a set of 70 photomultiplier signals (cf. Figure 3.2), each resulting from the average of 256 raw signals generated by the fluorescence induced by laser pulses with central frequencies varying between 96743 cm^{-1} and 96754 cm^{-1} (103.35-103.37 nm). The as determined laser excitation spectral profiles of $d\Psi_N(\delta\nu_N)$ is shown in Figure 3.7. For the

experimental conditions of the study, the excitation spectra can be well approximated by a Gaussian profile, since the spectral shape of the laser is Gaussian and also the spectral broadening of absorption lines is dominated by Doppler broadening $\Delta\lambda_D$ for all the atomic species considered, *i.e.* N-atom, H-atom and Kr-atom. This broadening can be mathematically represented by the formula proposed by [151], reported here as equation (3.12):

$$\Delta\lambda_D = 7.162 \times 10^{-7} \lambda_0 \sqrt{\frac{T_{gas}}{M}} \tag{3.12}$$

where λ_0 is the wavelength expressed in nm, T_{gas} the gas temperature in K units and M the atomic mass of the gaseous species in mass units.

The LIF signal of I_2 is also depicted in Figure 3.7 and it is seen that the excitation spectra extends over several I_2 fluorescence maxima, which indicates a fairly high broadening of the laser line, typically 2 cm^{-1}.

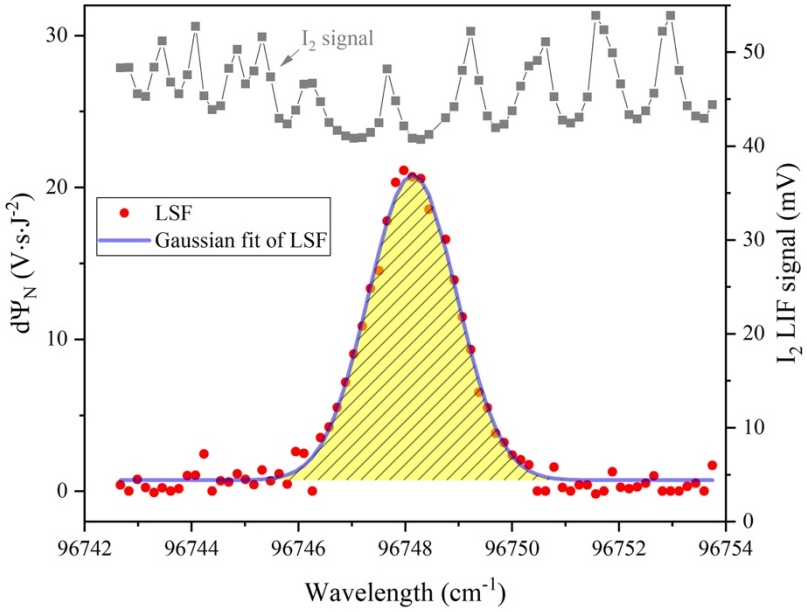

Figure 3.7: N-atom TALIF laser excitation spectra obtained from data processed using the nonlinear least-square fitting procedure (red solid circles) and their Gaussian fit (blue line). The pressure is equal to 20 Pa and the maximum MW power is equal to 140 W. The I_2 LIF laser excitation spectrum (grey solid squares) used for absolute calibration of the laser wavelength is also plotted above.

However, the use of FEM requires the determination of the time and frequency integrated fluorescence signals for each density value measurements. In our experiments, the time taken for acquiring 70 spectral points typically took 20 minutes of acquisition, during which the wavelength

proved to be stable. This is obviously not suitable for time-resolved measurements required in the context of the present thesis on pulsed plasma.

To circumvent this issue, we first make use of the specific discharge conditions investigated here in order to estimate $g(\delta\nu_A)d(\delta\nu_A)$, with A = N, H or Kr, and subsequently use equation (3.5) to readily determine atom density using a single laser shot at the central frequency of $0.5\nu_A$. The procedure used for this purpose is discussed in the following.

From the experimental point of view, $g(\delta\nu_A)d(\delta\nu_A)$ may be determined from the full excitation spectrum. As a matter of fact, taking the ratio of equations (3.3) and (3.6), one obtains for an atom A = N, H or Kr:

$$g(\delta\nu_A)d(\delta\nu_A) = \frac{d\Psi_A}{\int_{\delta\nu=-\infty}^{\infty} d\Psi_A} \tag{3.13}$$

Actually, $g(\delta\nu_A)d(\delta\nu_A)$ depends on the spectral profiles of the laser and the absorption lines. The spectral profile of the laser used in this study is Gaussian and this is also the case for the absorption lines in our conditions. In this case, the overlap factors may be easily expressed as:

$$g(\delta\nu_A)d(\delta\nu_A) = \frac{\sqrt{4ln2/\pi}}{\Delta\nu_{G,A}^{eff}} e^{-4ln2\left(\frac{\delta\nu_A}{\Delta\nu_{G,A}^{eff}}\right)^2} d(\delta\nu_A) \tag{3.14}$$

where $\Delta\nu_{G,A}^{eff} = \sqrt{2\Delta\nu_{G,l}{}^2 + \Delta\nu_{G,A}{}^2}$ is the effective Gaussian Full-Width at Half Maximum (FWHM) due to convolution of the laser ($\Delta\nu_{G,l}$) and the transition profiles ($\Delta\nu_{G,A}$). $\Delta\nu_{G,A}^{eff}$ is experimentally obtained from the full excitation spectrum.

The laser broadening $\Delta\nu_{G,l}$ was determined from the TALIF signal of krypton at 300 K (without plasma). In such a condition, the Doppler broadening of the krypton absorption line is estimated to be 0.13 cm^{-1}. The measured broadening of the krypton full excitation spectrum line is 1.59 cm^{-1} which is much greater than the Doppler broadening of krypton at 300 K. The resulting value of the laser line broadening is 1.10 cm^{-1}. It is worthy to mention that this value is significantly larger than those usually reported in the literature, for e.g. 0.25 and 0.36 cm^{-1} in [48] and [57] respectively, due to experimental setup differences.

The determination of the absorption line broadening, $\Delta\nu_{G,N}$, for N-atom in the plasma requires the knowledge of the gas temperature. This was estimated from the rotational temperature of

$N_2(C^3\Pi_u)$ electronically excited state, using optical emission spectroscopy (OES) applied to the transition $N_2(C^3\Pi_u \rightarrow B^3\Pi_g, \Delta v = -2)$ and for stationary operation of the MW plasma. The rotational temperature varied between 450 K and 600 K for the investigated range of MW power as shown in Figure 3.8. The resulting absorption linewidth for nitrogen remained almost constant at a value of approximately 0.46 cm^{-1}, which is two times smaller than the laser broadening.

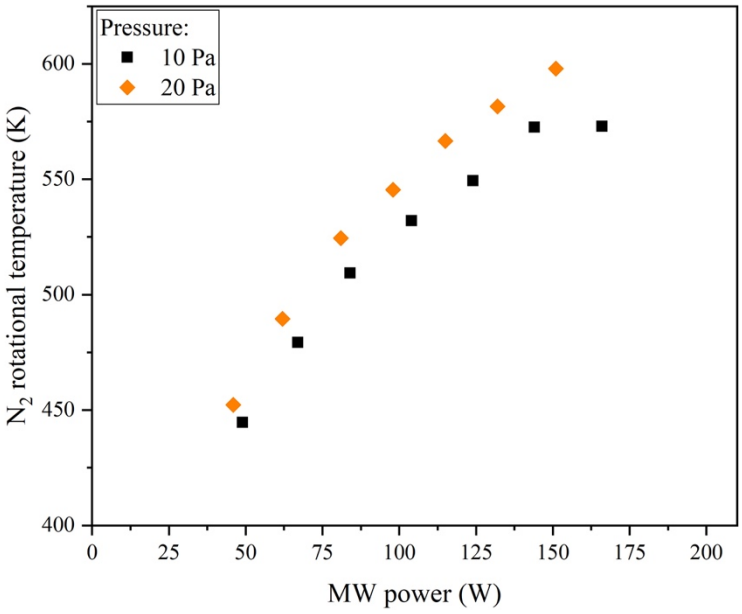

Figure 3.8: Rotational temperatures of N_2 plasmas generated in Aura-Wave source.

In any case, since the gas temperature does not change significantly (standard deviation being approximately 5% of the mean value), the Doppler broadening of N-atom, and thus $\Delta\nu_{G,N}$ and $g(\delta\nu_N)$, should remain almost constant for the considered discharge parameters. This was confirmed by measuring the FWHM of the excitation spectrum $\Delta\nu_{G,N}^{eff}$ over a wide range of plasma conditions as shown in Figure 3.9.

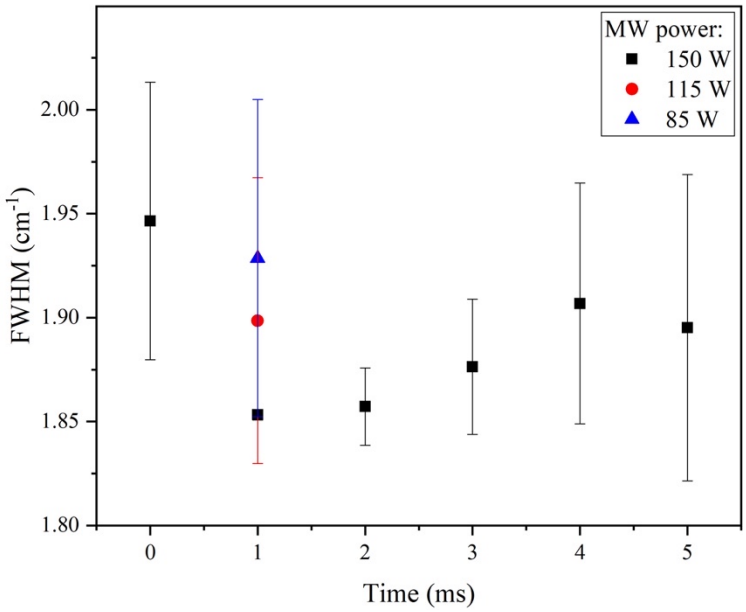

Figure 3.9: Experimental spectral width in cm^{-1}, measured at the fundamental wavelength of the dye laser (16125.135 cm^{-1}), and deduced from the laser excitation spectra for several phases and three MW powers and 20 Pa.

This finding resulted in a significant simplification of the measurement procedure. As a matter of fact, the experiments to estimate the full integral $\int_{\delta\nu=-\infty}^{\infty} d\Psi$ have to be performed only once in order to obtain $g(\delta\nu_A)$. The N-atom density can then be readily determined through equation (3.5) using a single laser shot at a central frequency of 0.5 ν_A, which significantly simplifies the measurement procedure. The use of the peak value at 0.5 ν_A enables achieving the maximum overlap between the laser and the absorption lines, thus limiting the uncertainties on the measured N-atom density. This method is referred to as **Peak excitation method (PEM)**.

Figure 3.10 shows the variation of N-atom densities measured using the full excitation method (FEM) and the peak excitation method (PEM) at different instants during the decay phase of the pulsed plasma operation (graph on the left) and as a function of the power coupled to the plasma (graph on the right). The considered discharge conditions correspond to a pulsed plasma operation with a duty cycle of 0.4 and frequency 10 Hz. The results obtained by the two approaches are in a very good agreement.

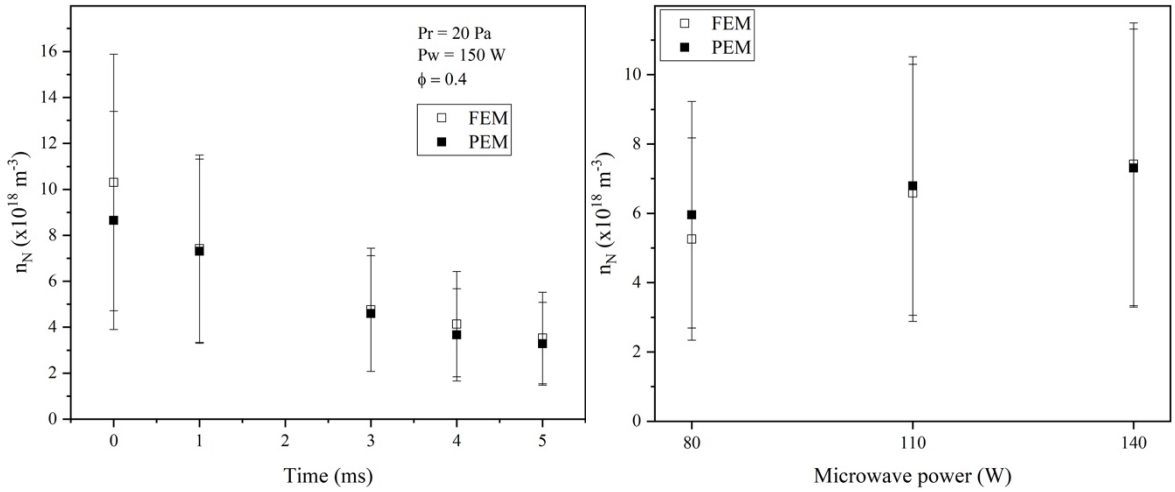

Figure 3.10: Comparison of the atomic nitrogen density obtained using the full excitation method (FEM) and the peak excitation method (PEM) for the time evolution at high power of 150 W (left) and three MW power values of the high power phase with measurements performed 1 ms after plasma was switched off (right). The pressure is equal to 20 Pa and the duty cycle is equal to 0.4 and pulsation frequency 10 Hz.

PEM is valid as long as the spectral profiles of the absorption lines chosen for TALIF measurements do not change over the investigated plasma conditions. The approach seems to be particularly suitable for low temperature moderate pressure plasmas where the change in line broadening width due to Doppler and Stark effects remain fairly limited, as seen in our conditions for nitrogen plasmas. Therefore, PEM approach has been used to determine the atom densities wherever it is possible.

Similar to nitrogen plasmas, the FWHM of hydrogen plasmas generated by the Aura-Wave is seen to be insensitive to pressure as seen in Figure 3.11.

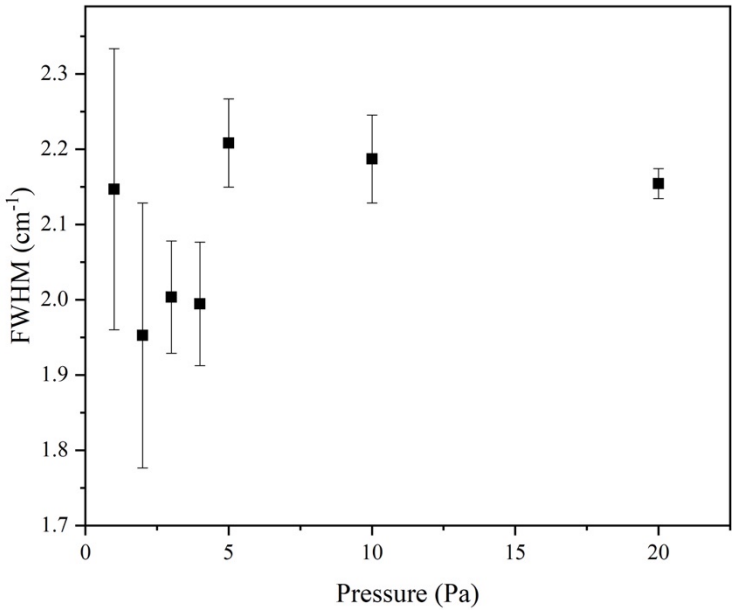

Figure 3.11: Calculated FWHM in H_2 plasmas generated by Aura-Wave source. The applied power was the highest-possible to be coupled, ranging between 165 W and 200 W according to the considered pressure condition.

This is owing to the low range of variation of gas temperature, between 400 K and 500 K raising the coupled MW power from 50 W to 180 W, as shown in Figure 3.12, and the dominance of the laser broadening similar to that of nitrogen. Thus, this permits us to adopt PEM approach even for hydrogen for Aura-Wave conditions.

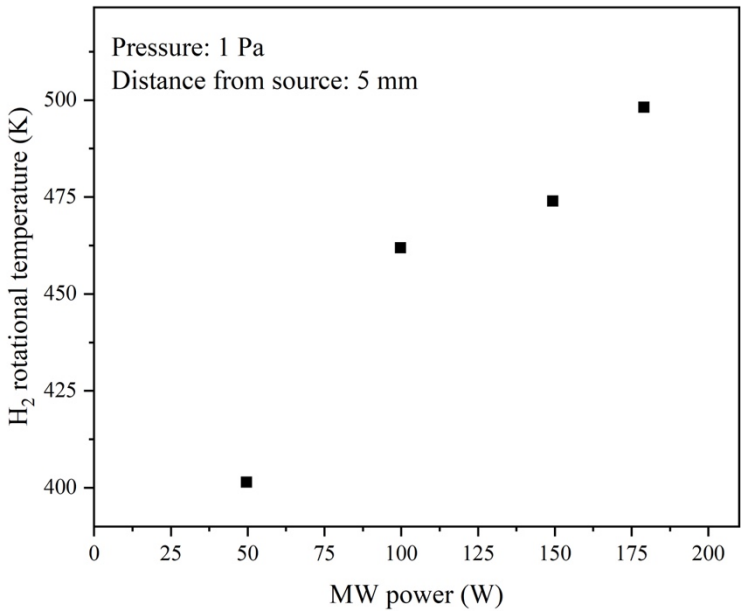

Figure 3.12: Rotational temperatures of H_2 plasmas generated in Aura-Wave source. The experiments were performed by [152]

3.8 Uncertainty analysis

The uncertainty on the measured atom densities was calculated using the propagation of uncertainties of the independent variables [153]. Accordingly, the uncertainty for species A=H or N can be written as

$$\frac{\delta n_A}{n_A} = \left\{ \left(\frac{\delta K_A}{K_A}\right)^2 + \left(\frac{\delta \tau_{f,Kr}}{\tau_{f,Kr}}\right)^2 + \left(\frac{\delta \int_{-\infty}^{\infty} \mathrm{d}\Psi_{\mathrm{Kr}}}{\int_{-\infty}^{\infty} \mathrm{d}\Psi_{\mathrm{Kr}}}\right)^2 + \left(\frac{\delta n_{Kr}}{n_{Kr}}\right)^2 + \left(\frac{\delta \tau_{f,A}}{\tau_{f,A}}\right)^2 + \left(\frac{\delta \int_{-\infty}^{\infty} \mathrm{d}\Psi_{\mathrm{A}}}{\int_{-\infty}^{\infty} \mathrm{d}\Psi_{\mathrm{A}}}\right)^2 \right\}^{0.5} \quad (3.15)$$

where K_A refers to all the independent variables in equation (3.8) other than the independent variables obtained after LIF signal analysis. The uncertainties of these variables were either obtained from the literature (two photon absorption cross-sections) or datasheets of the manufacturers (transmission of filters, photomultiplier sensitivity).

The uncertainties of $\Delta\nu_{G,A}^{eff}$ are generally obtained over several repetitions of the full excitation spectrum. However, when the full excitation spectrum is to be determined only once, the uncertainty is derived from the uncertainties of $\mathrm{d}\Psi$ at peak and $\int_{\delta\nu=-\infty}^{\infty} \mathrm{d}\Psi$. The uncertainties of τ_f for N and Kr are directly obtained from repeated measurements. While for H-atom, the uncertainty of τ_f are assumed to be 15%. In general, when τ_f vary with conditions (power and pressure) due to collisional processes, the mean and uncertainty of τ_f would be determined from the several temporal signals captured while the full excitation spectrum is recorded.

The uncertainty of the temporal TALIF integral $\mathrm{d}\Psi_A$ depends on the fit parameters which are in fact by-products of the fitting procedure. The uncertainties of the fit parameters are derived from the covariance matrices associated with these quantities. The uncertainty of the integral itself then is calculated as

$$\left(\frac{\delta \mathrm{d}\Psi_{\mathrm{A}}}{\mathrm{d}\Psi_{\mathrm{A}}}\right)^2 = \left(\frac{\delta A_1}{\mathrm{A}_1}\right)^2 + \left(\frac{A_1}{\mathrm{d}\Psi_{\mathrm{A}}}\right)^2 \times \left\{ (t_1 - t_0)^2 \delta {\tau_{f,A}}^2 + \left(\tau_{f,A} + t_1 - t_0\right)^2 (\delta {t_1}^2 + \delta {t_0}^2) \right\} \quad (3.16)$$

It should be noted that the background A_0 does not explicitly feature in the uncertainty of the LIF signal, but is implicitly included through the covariance matrix. The uncertainties of the spectral TALIF integrals and $\int_{\delta\nu=-\infty}^{\infty} \mathrm{d}\Psi$ are obtained directly from the fitting procedure [154] of the gaussian fit by evaluating the covariance matrices associated with the different quantities.

Figure 3.13 shows the contributions of the different independent variables to the uncertainty of the nitrogen atom density at 20 Pa and 140 W. The largest contribution to the relative error on nitrogen atom density comes by far from the uncertainty on the ratio of the two-photon absorption cross-sections for nitrogen and krypton, 50%, [127]. The second error source comes from the uncertainty on the krypton radiative lifetime, 20% [145]. The uncertainties on the time-integrated peak fluorescence intensity, dΨ, determined using the procedure described above contributes to 10-15% to the global relative error on the density. The contributions of the other error sources are below 5%.

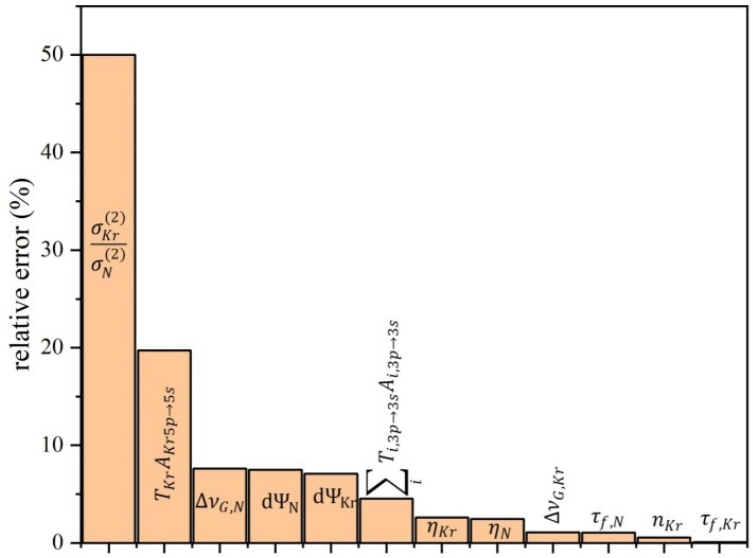

Figure 3.13: relative errors for the different terms of the equation (3.5)

3.9 Effects of plasma background on the quality of LIF signals

As Aura-Wave source works at low pressures (1 – 20 Pa), it produces very strongly emissive nitrogen plasmas. Figure 3.14 shows the emission intensities along the axis of the source at pressure of 2 Pa. For regions very close to the magnet (~5 mm) where ECR should be active, strong emissions are observed, which in fact saturated the photomultiplier. For distances greater than 6 mm the FPS emission is smoothly reducing where the photomultiplier did not get saturated. Despite this, the LIF signal was too weak to make any N-atom measurements mainly because of low N-atom density compounded by very strong background emissions.

The background emission decreases with pressure. This could be explained due to increasing quenching rates of $N_2(B^3\Pi_g)$ states with pressure. Aura source could be operated up to 20 Pa with both H_2 and N_2 gases. Note that these pressures are too high for the ECR to have any impact on the plasma processes. Nevertheless, the plasma emissions are quite high close to the magnet. It was

permissible to make measurements at a distance of 10 mm from the magnet at 10 Pa and 20 Pa. The FPS emission at 10 Pa is still quite high, 2 to 3 times stronger than at 20 Pa as seen in Figure 3.14.

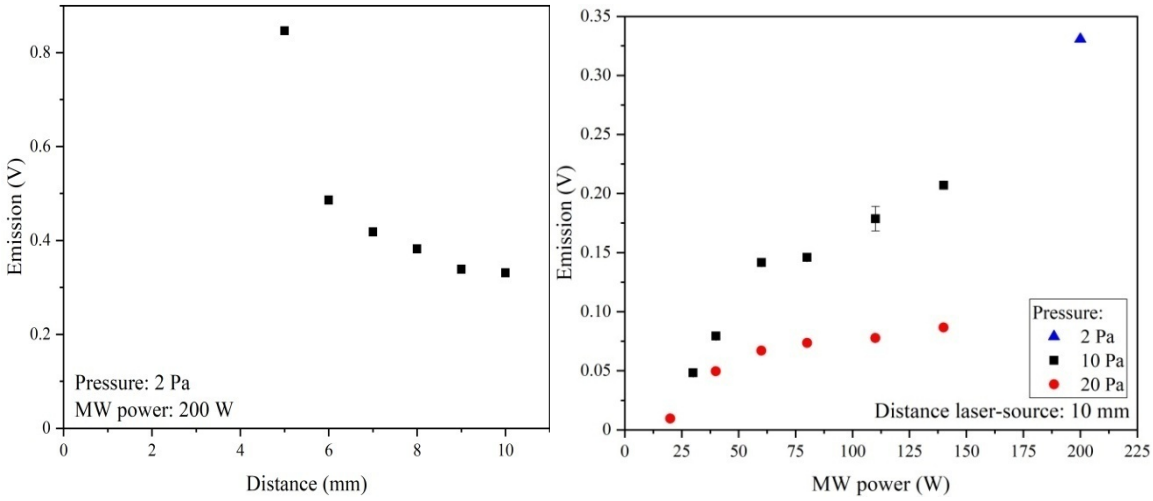

Figure 3.14: FPS emission values as a function of distance from Aura-Wave magnet in a 2 Pa plasma (left) and as a function of power and pressure (right)

It is worthwhile to study the effects of noise and background on the LIF signals. Here we introduce two definitions for this (I) Signal to Noise ratio (S/N) calculated as $A_1(t_1 - t_0)/\Delta A_0$ and (II) Signal to Background (S/B) ratio determined as $A_1(t_1 - t_0)/A_0$ (cf. Figure 3.2) . Even though the noise with respect to the background can be small (around < 5%), the magnitude of the noise with respect to the TALIF signal itself can be huge.

Figure 3.15 shows the signal to noise ratios (S/N) as a function of signal to plasma emission denoted as S/B for different conditions. As a matter of fact, S/B calculated on LIF spectra registered at 10 Pa are one order of magnitude smaller than those determined in plasmas sustained at 20 Pa, i.e. 0.02 and 0.4 respectively. Although the FPS emissions are comparable at power below 80 W, the S/B ratios at 10 Pa are much lower than what is observed at 20 Pa because of a relative decrease of N-atom densities with pressure. Accordingly, the S/N ratios at 10 Pa were poor.

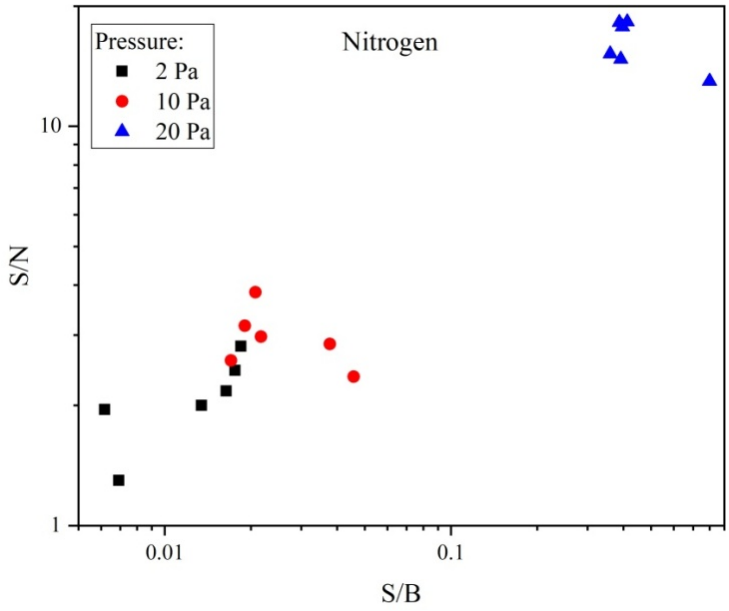

Figure 3.15: S/N dependence on S/B in Aura-Wave sustained nitrogen plasmas for different pressure conditions.

Figure 3.16 represents the effect of power on N-atom densities in plasmas sustained at 20 Pa and 10 Pa. It is observed that the N-atom density increases with MW power at 20 Pa which is not observed at 10 Pa. Also, the N-atom densities at 10 Pa and 20 Pa do not scale consistently with pressures. These results are not surprising as the S/N ratio at 10 Pa is around 2 to 3 due to the strong background emission and this is reflected in poor estimation of N-atom densities with huge uncertainties. This in fact demonstrates the limit to which TALIF acquisitions can be applied. Therefore, it was only possible to do experiments at 20 Pa for nitrogen plasmas with Aura-Wave source.

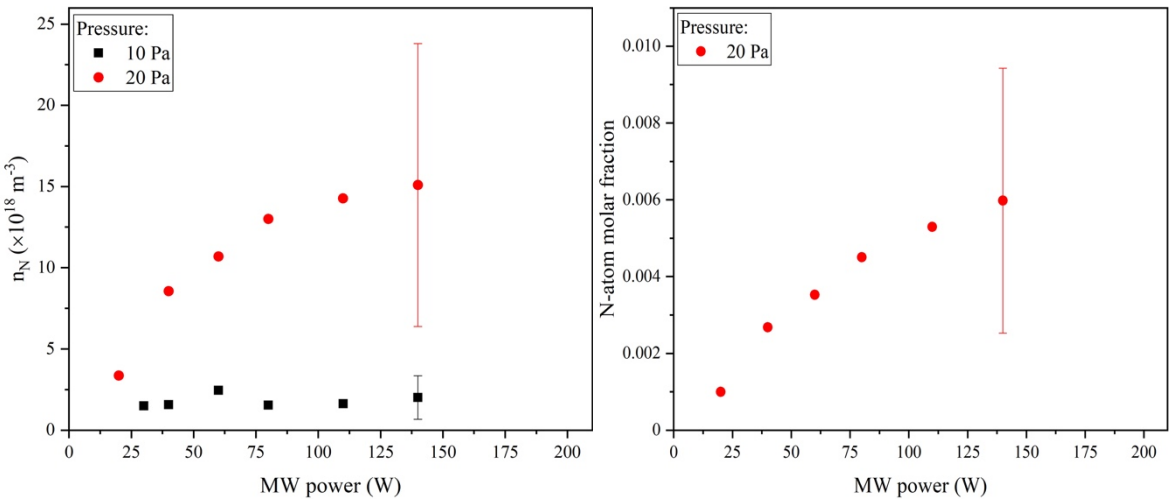

Figure 3.16: N-atom density (left) and molar fraction (right) dependences with MW power in plasmas generated in SAIREM® Aura-Wave.

Contrastingly, hydrogen plasmas which had very low background emission even at pressures as low as 1 Pa (with similar order of magnitudes of the atom densities for both hydrogen and nitrogen plasmas) could record very good quality signals at pressures of 1 Pa. Figure 3.17 shows the S/N recorded and the corresponding H-atom densities as a function of power and pressure. It is quite evident from the analysis that the strong plasma background can deteriorate the quality of the TALIF signals captured and thus imposes the limitation on the measurability of the atom-densities.

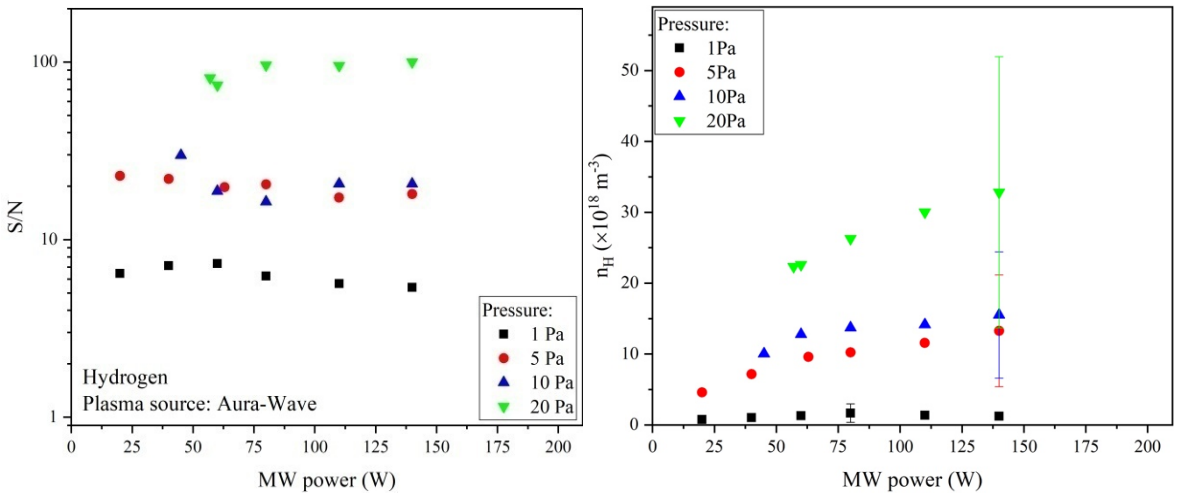

Figure 3.17: S/N ratios calculated in Aura-Wave hydrogen plasmas (left) and correspondent H-atom densities generated in different pressure (from 1 Pa to 20 Pa) and power (from 20 W to 140 W) conditions (right).

One of the alternative methodologies to measure atom-densities with strong background is to pulse the plasmas and make measurements few ms in to the plasma off phase when the background emission decays very quickly as compared to the atom densities [96]. Then, the atomic densities can be determined by extrapolating the atom-densities measured at different instants to time $t = 0$ when the plasma was switched off. Figure 3.18 shows the (a) S/N and S/B ratios, (b) the uncertainty of TALIF integral $\delta d\Psi_A$ and (c) N-atom densities and background emission for nitrogen pulsed plasmas at 20 Pa and 140 W.

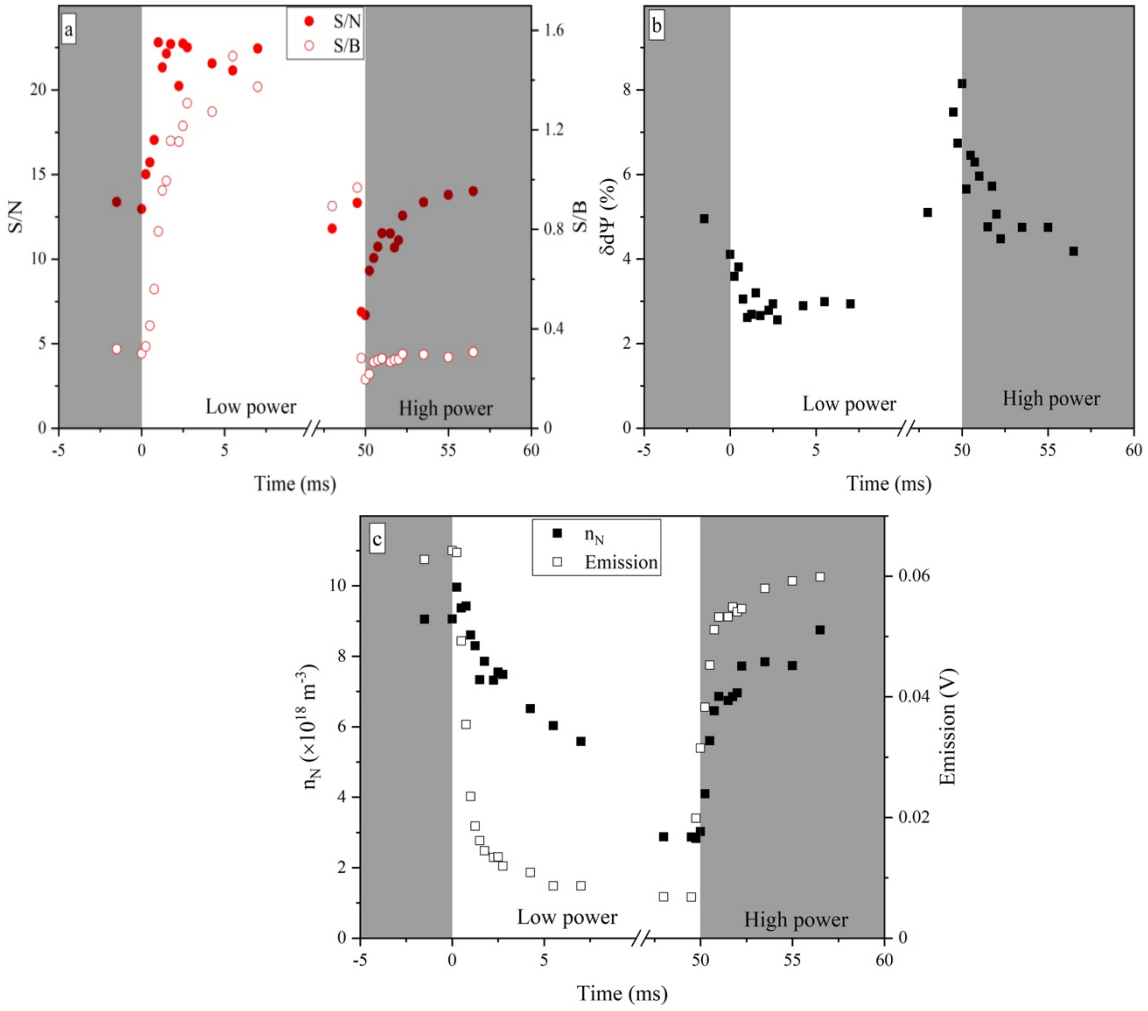

Figure 3.18: Time influence on (a) signal to noise S/N and signal to background emission S/B ratios, (b) uncertainty on TALIF integral $\delta d\Psi_A$ and (c) N-atom density and background emission.

During the plasma on-phase, the S/N and S/B ratios are both quite low owing to high background emissions. As soon as the plasma is switched off, the S/B ratios are seen to increase rapidly reflecting the rapid decay of background emission as compared to the N-atom density. This seems to have a positive effect as S/N ratios improve substantially for initial stages of the low power phase. This trend is also imitated by $\delta d\Psi_A$, which decrease substantially. However, over longer periods of time as the N-atom decays, the S/N ratio as well as $\delta d\Psi_A$ increase considerably. Although the contribution of $\delta d\Psi_A$ to the total uncertainty of N-atom, the analysis establishes the relationship between plasma background and the quality of signal captured and its effects on the uncertainty of TALIF integrals.

On the other hand, at the transition between low-power phase to high power phase, the S/N ratio as well as the uncertainty $\delta d\Psi_A$ suggest improvement. This is counter-intuitive as the signal seems to improve, in spite of high background emission. However, the improvement in the signals is due to the increase in the N-atom density and thus the fluorescence signal itself. Therefore, the quality

of the signal is affected by both the N-atom density as well as the background emission. This makes it rather difficult to predict the limit of detection, *i.e.* the least atom density that can be measured.

Likewise, when applying the pulsed plasma method at a pressure of 10 Pa did not deliver satisfactory results owing to the fast decay of N-atom densities to counter the positive effects of decay of the background emission. Also, attention needs to be paid to the surge of N-atom densities as soon as the plasma is switched off as seen in Figure 3.19. This reproducible surge is similar to the one observed in reference [53] where the authors showed an unexpected increase of N($^4S^o$) TALIF signal at the start of the plasma off phase in a pulsed microwave plasma. The methodology used in the present work provides TALIF measurements with a time resolution as low as 5 µs and a straightforward signal processing which enables investigating short time-scale kinetics effects for N($^4S^o$). This has been used to confirm and further study the existence of this fast increase in N-atom TALIF signal that is expected to occur within 500 µs during the early stage of the low power phase. Figure 3.19 shows time-resolved measurements with a much better resolution, i.e., 10 µs resolution, of the N($^4S^o$)-atom density and the background plasma emission near the transition between the high- and low-power phases. This figure confirms the existence of a significant increase in the N-atom density (more than 10^{18} m^{-3}, which represents more than 10% relative variation) just after the transition to the low power phase. Actually, a high N($^4S^o$) density level is maintained during almost 1 ms after the power transition. Note that such behavior is not observed for the plasma emission intensity that decreases sharply just after the transition.

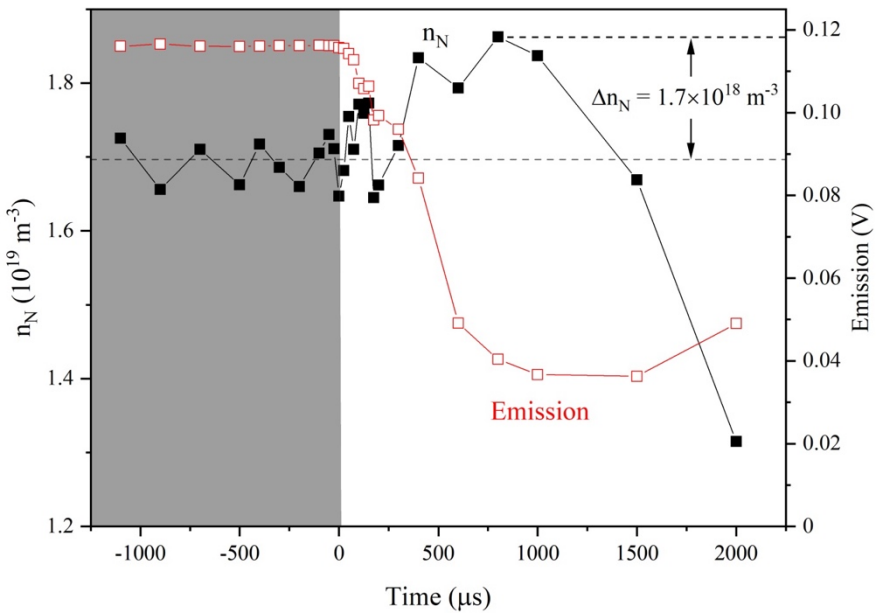

Figure 3.19: Time-resolved measurement of N-atom (black circles, left axis) and $N_2(B^3\Pi_g)$ emission (red squares, right axis) around the transition between the high and low power phases and during the early stage of the low power phase.

On the opposite, when the plasma is switched on, one can observe the sharp decrease in the N-atom densities. These observations may seem unphysical at first look, but it actually occurs due to the fast transients involving N-atom and its metastables N($^2P^o$) and N($^2D^o$) at the instant the plasma is switched off or on. This phenomenon will be discussed in detail in chapter 6. This means extrapolation of atomic densities from transient decay profile may not produce the actual atomic densities during the plasma on phase. Notwithstanding this, the method of using pulsed plasma measurements can be used as a substitute to make measurements for stationary strongly emissive plasma whenever permissible.

A similar analysis for pulsed hydrogen atom was also carried out. Figure 3.20 shows the (a) S/N and S/B rations, the (b) uncertainty of TALIF integral $\delta \mathrm{d}\Psi_{\mathrm{A}}$ and (c) H-atom densities and background emission for hydrogen pulsed plasmas at 1 Pa and 200 W. The effect of S/B ratio on S/N ratio is also visible to a certain extent for pulsed H plasmas at the instant when the plasma is switched off and similar observations can be made about $\delta \mathrm{d}\Psi_{\mathrm{A}}$ variation. It also seems that H-atom density shows a surge at the instant the plasma is switched off.

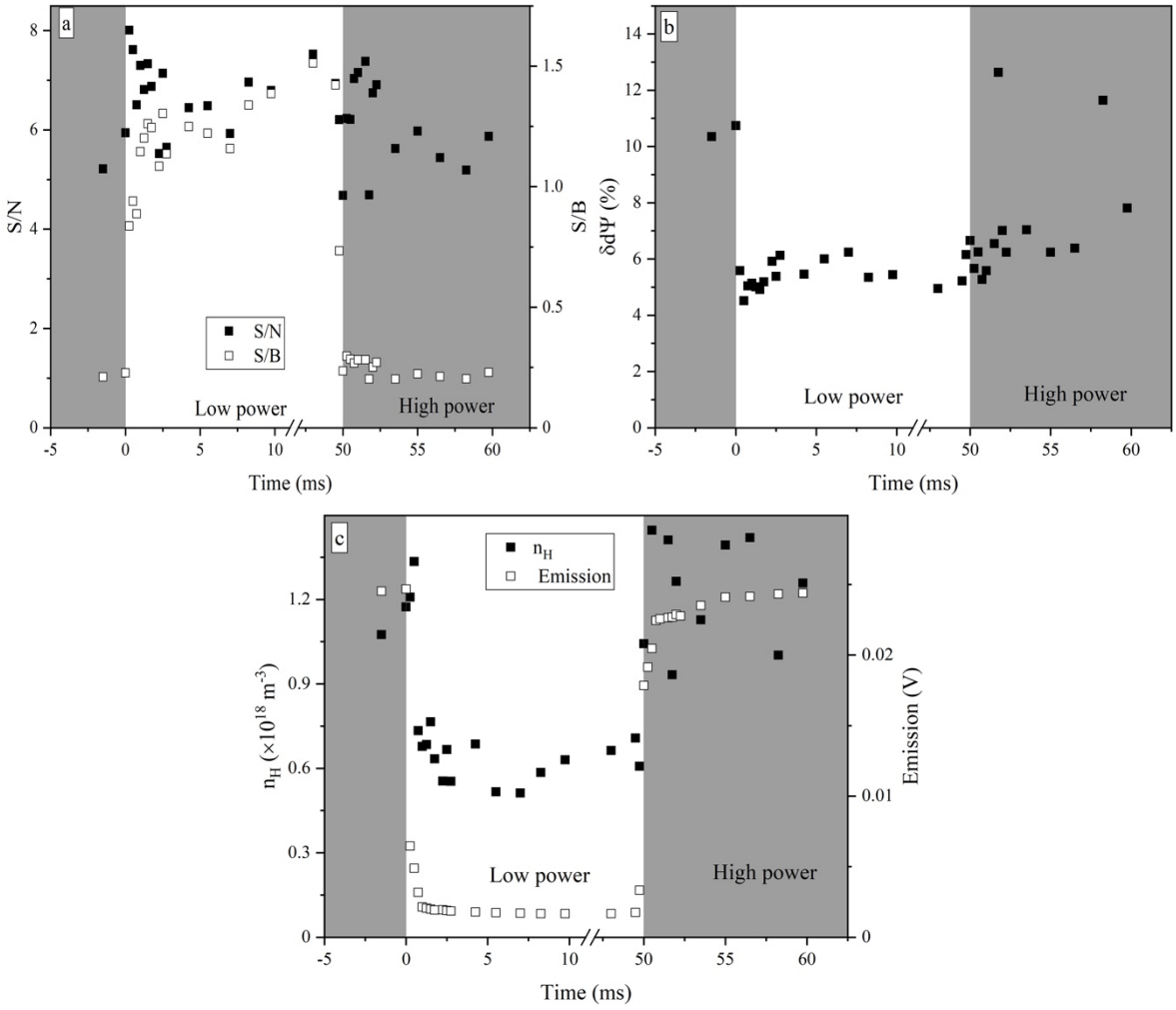

Figure 3.20: Time influence on (a) signal to noise S/N and signal to background emission S/B ratios, (b) uncertainty on TALIF integral $\delta d\Psi_A$ and (c) H-atom density and background emission.

3.10 Conclusion

The chapter has presented in detail the analysis carried out to estimate the atom-densities and their uncertainties. In this chapter, the validity of Peak Excitation Method (PEM) in the conditions of ECR microwave plasmas has been demonstrated. This method is valid as long as the spectral profiles of the absorption lines chosen for TALIF measurements do not change over the investigated plasma conditions. The approach seems to be particularly suitable for low temperature moderate pressure plasmas where the change in line broadening width due to Doppler and Stark effects remain fairly limited.

Further, the relationship between signal background and noise was demonstrated for stationary and pulsed plasma conditions. The ns-TALIF PEM was also applied to investigate the transients at the transition between the low- and high-power phases of pulsed plasmas where the existence of the unexpected increase in N($^4S^o$)-atom density at the early stage of the low-power phase is observed. We refer to as “surge” in this thesis. Later in chapter 6, it will be shown that the surge occurs due to

the conversion of metastables $N(^2D^o)$ and $N(^2P^o)$ into $N(^4S^o)$. The results obtained show that such increase should be taken into account when using extrapolated values from N-atom densities measured in the post discharge in order to determine the dissociation yield in an emissive discharge.

The methodology presented here will be the basis for all the TALIF acquisitions in the thesis.

Chapter 4 – Nitrogen collisional radiative model

4.1 Introduction

This chapter will introduce a transient quasi-homogeneous (0D) plasma model for simulating non-equilibrium nitrogen plasmas that has been developed during the course of the thesis. The chapter will briefly outline the mathematical basis of the kinetic solver and will give detailed description of different collisional and radiative processes involved. These reactions were carefully chosen over a wide range of literature production, including the well-known work from Capitelli [104], the detailed database presented by Annaloro [155] and the more recent review published by Guerra *et al.* [156]. The presented kinetics model will be used to study different conditions conforming to the experiments as well as serve as a guide to understand the mechanisms assisting dissociation of nitrogen.

4.2 Collisional radiative model for pure N_2 plasmas

The quasi-homogeneous plasma model, whose mathematical algorithm is similar to the one developed for H_2 plasmas in reference [96,157], has been developed with the aim of accurately predicting of the dissociation and ionization kinetics of nitrogen pulsed microwave discharges. The model takes into account relevant collisional and radiative processes such as collisional radiative and a vibrational kinetic models of electronically excited molecular nitrogen states, a collisional radiative model for atomic nitrogen, a dissociation model that considers electron-impact, vibrational 'ladder climbing' and electronically excited states quenching phenomena and an ionization model for both molecular and atomic nitrogen.

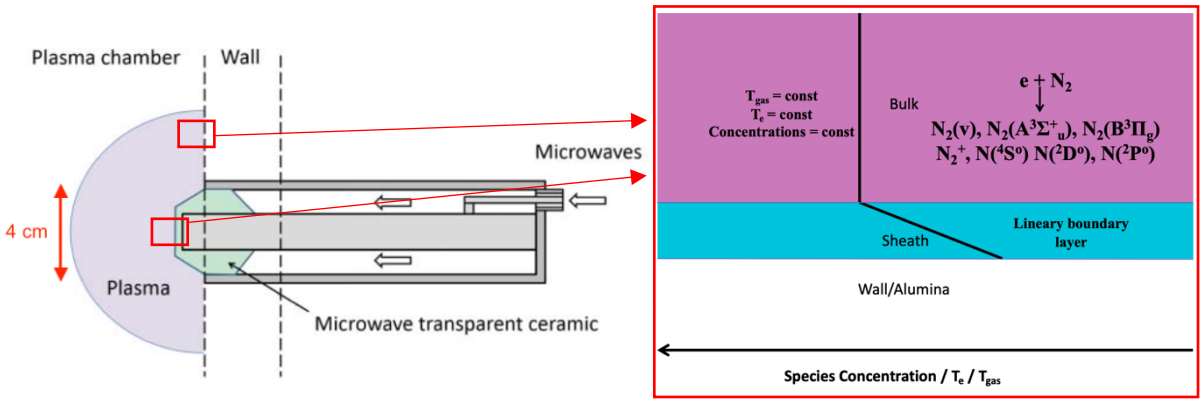

Figure 4.1: Structure of the studied MW plasma source (as seen in Figure 2.4) [117] (left) and schematic of the functioning of the adopted 0D model (right)

Figure 4.1 illustrates the structure of the non-magnetized source and a scheme of the model. In this model, the MW power is applied to plasma of volume V which is in contact with a reactor wall with surface area S. The plasma volume is assumed to be made of two regions: (I) a bulk homogeneous plasma and (II) a linear boundary layer through which ions, long-living excited states and atoms can diffuse and recombine at the wall. The MW heats up the electrons to high energies. Subsequently the electrons collide with the heavy species to produce excited species and ions. The heavy species are assumed to be well represented by Maxwellian distribution characterized by a gas temperature T_g. For non-equilibrium low-pressure plasmas, the electron energy distribution function (EEDF) is characterized by a strong deviation from Maxwellian behavior which is taken into account through the solution of Boltzmann equations for the electrons. Therefore, the key parameter for the MW model is the MW power density P_{MW} (in W cm^{-3}), which is nothing but coupled MW power (W) by plasma volume V (cm^{-3}).

The present chapter will describe the solution procedure for the self-consistent collisional radiative model for pulsed MW plasma over wide ranges of pressure and power density, typically between few Pa, where the P_{MW} is usually few W·cm^{-3}, and atmospheric pressure, with P_{MW} of few hundreds of W·cm^{-3}.

4.2.1 Species

The temporal variation for each species populations in the plasma bulk can be expressed as

$$\rho \frac{dY_s}{dt} = W_{s-g} + W_{s-w} \tag{4.1}$$

where the subscripts *g* and *w* indicate whether the species is in the gas and the wall phase, W_{s-g} and W_{s-w} are the two net production rates through homogeneous volumetric reactions and surface processes respectively, ρ is the plasma density and Y_s denotes the mass fraction of the species '*s*'. The density of the electrons is enforced using the plasma electrical neutrality condition.

The species considered in the model includes nitrogen molecule and its excited states, N-atom and its excited states, while ionization kinetics are described considering four ionic species: N^+, N_2^+, N_3^+ and N_4^+ and electrons.

The electronically excited states of N_2 molecule that have been considered in the present model are $X^1\Sigma^+_g$, $A^3\Sigma^+_u$, $B^3\Pi_g$, $C^3\Pi_u$ and $a'^1\Sigma^-_u$ and are tabulated in Table 4.1.

Table 4.1: Electronic excited states of N_2 molecule, with energy in eV and degeneracy g, considered in the CR model

State	Energy (eV)	g
$A^3\Sigma^+_u$	6.765	3
$B^3\Pi_g$	7.744	6
$a'^1\Sigma^-_u$	9.191	1
$C^3\Pi_u$	11.188	6

Because the microwave plasmas here studied were investigated over fairly long-time scales, it was explicitly chosen not to include the excited states which are short lived and are rapidly converted through radiative or collisional cascade. Rather, the collisional processes involving these short-lived states have been directly taken into account for the final species of their respective kinetic cascade. For example, the electronic state $W^3\Delta_u$ which is usually formed through electron impact excitation is assumed to be instantaneously converted to $B^3\Pi_g$, $a^1\Pi_g$ is assumed to be instantaneously converted to $a'^1\Sigma^-_u$, the pre-dissociative states such as $b^1\Pi_u$, $c'^1\Sigma^+_u$ and $b'^1\Sigma^+_u$ undergo direct dissociation. The model also takes into consideration 49 vibrational levels (from v = 0 to v = 48) of the electronic ground state $N_2(X^1\Sigma^+_g)$ which have been tabulated in Table 4.2. This is important to describe accurately the vibrational dissociation mechanism of N_2 molecules. In order to simplify the model, the vibrational distributions of the electronically excited states have not been considered in the present CR model.

Table 4.2: Vibrational levels of the electronic ground state $N_2(X^1\Sigma^+_g)$ considered

v	eV		v	eV		v	eV		v	eV
0	0		13	3.4767		25	6.1398		37	8.2546
1	0.2889		14	3.7189		26	6.3374		38	8.4051
2	0.5742		15	3.9574		27	6.5312		39	8.5515
3	0.8556		16	4.1924		28	6.7211		40	8.6937
4	1.1341		17	4.4236		29	6.9072		41	8.8319
5	1.4088		18	4.6512		30	7.0894		42	8.9659
6	1.6798		19	4.8750		31	7.2677		43	9.0957
7	1.9473		20	5.0952		32	7.4421		44	9.2213
8	2.2112		21	5.3116		33	7.6126		45	9.3427
9	2.4715		22	5.5243		34	7.7791		46	9.4598
10	2.7282		23	5.7333		35	7.9416		47	9.5726
11	2.9813		24	5.9384		36	8.1001		48	9.6811
12	3.2308									

The model also relies on 27 electronically excited states of atomic nitrogen which have been tabulated in Table 4.3. Note that N-atom in the ground state, that is $(2p^3)^4S^o_{3/2}$, will be denoted as either N or N($^4S^o$) in the rest of the thesis.

Table 4.3: Electronic excites states of N-atom with energy in eV and degeneracy g, considered in the CR model

State	eV	g	State	eV	g	State	eV	g
$2s^22p^3\ ^4S^o$	0	4	$2s^22p^2\ (^3P)3p\ ^4S^o$	12.003	4	$2s^22p^2\ (^3P)3d\ ^4P$	12.986	14
$2s^22p^3\ ^2D^o$	2.391	10	$2s^22p^2\ (^3P)3p\ ^2D^o$	12.027	10	$2s^22p^2\ (^3P)3d\ ^4D$	13.005	20
$2s^22p^3\ ^2P^o$	3.568	6	$2s^22p^2\ (^3P)3p\ ^2P^o$	12.145	6	$2s^22p^2\ (^3P)3d\ ^2D$	13.021	10
$2s^22p^3\ (^3P)3s\ ^4P$	10.422	12	$2s^22p^2\ (^1D)3p\ ^2D$	12.373	10	$2s^22p^2\ (^3P)4p\ ^2S^o$	13.193	2
$2s^22p^3\ (^3P)3s\ ^2P$	10.774	6	$2s^22p^2\ (^3P)4s\ ^4P$	12.853	12	$2s^22p^2\ (^3P)4p\ ^4D^o$	13.242	20
$2s^22p^4\ ^4P$	10.948	12	$2s^22p^2\ (^3P)4s\ ^2P$	12.918	6	$2s^22p^2\ (^3P)4p\ ^4P^o$	13.268	12
$2s^22p^2\ (^3P)3p\ ^2S^o$	11.618	2	$2s^22p^2\ (^3P)3d\ ^2P$	12.963	6	$2s^22p^2\ (^3P)4p\ ^2D^o$	13.292	10
$2s^22p^2\ (^3P)3p\ ^4D^o$	11.785	20	$2s^22p^2\ (^3P)3d\ ^4F$	12.971	28	$2s^22p^2\ (^3P)4p\ ^4S^o$	13.32	4
$2s^22p^2\ (^3P)3p\ ^4P^o$	11.871	12	$2s^22p^2\ (^3P)3d\ ^2F$	12.983	12	$2s^22p^2\ (^3P)4p\ ^2P^o$	13.348	6

4.2.2 Collisional processes

In this section, we will discuss the different collisional processes with regard to nitrogen plasmas that have been taken into account. Estimation of the source term W_{s-g} in the species balance equation for each species will require the determination of rate constants of all the processes involved.

Reaction rates for electron impact processes where cross-section data is available is directly evaluated from the electron energy distribution function (EEDF) obtained from the solution of the Boltzmann equation for electrons. All other reaction rates unless specified, are represented in the

form of modified Arrhenius equation $aT^b e^{-\left(\frac{c}{T}\right)}$, with a is then expressed in $mol \cdot m^{-3}$, b is non-dimensional exponent and c has units of K and T is the temperature at which the rates are evaluated (in kelvins). For reactions having the heavy body species as reactants, the rates are evaluated at T_g while reactions with electrons are evaluated at T_e (in kelvins).

The following section will list the different collisional processes considered in the model.

Electron impact processes

The electron-impact processes involve: (I) the vibrational excitation of the electronic ground state, (II) the electronic excitation of nitrogen molecule and atoms, (III) the direct dissociation through dissociative or pre-dissociative excited states and (IV) the direct ionization of nitrogen molecule and atom. The cross-sections of all super-elastic processes were determined from the corresponding inelastic processes using the principle of detailed balance, which can be written as:

$$\sigma^{j\to i}(\epsilon_i - \epsilon_{TH}) = \frac{g_i}{g_j}\sigma^{i\to j}(\epsilon_i) \tag{4.2}$$

where $\sigma^{j\to i}$ and $\sigma^{i\to j}$ are the forward and reverse processes, g_i and g_j are the degeneracies of the two states and ϵ_{TH} is the threshold energy of the forward process.

Vibrational excitation (e-v processes)

We considered 49 vibrational levels, *i.e.* v=0-48, and took into account the e-v processes of the form:

$$N_2(X^1\Sigma^+_g,v) + e^- \rightarrow N_2(X^1\Sigma^+_g,w) + e^- \text{ with } |w\text{-}v|\leq 15 \text{ and } v=0\text{-}48 \tag{R 4.1}$$

These involve both inelastic and super-elastic processes and the cross-sections have been taken from Phsy4entry database [158], even though when |w-v|>15 the cross section values were negligible and they were therefore not considered in our model.

Electronic excitation of molecular nitrogen (e-E-N_2)

All the processes coupling two excited states of N_2 were taken into account:

$$e^- + N_2(Y) \rightarrow e^- + N_2(Z) \tag{R 4.2}$$

where Y, Z = $X^1\Sigma^+_g$, $A^3\Sigma^+_u$, $B^3\Pi_g$, $C^3\Pi_u$ and $a'^1\Sigma^-_u$. The cross section data for the electronic excitation/de-excitation of molecular nitrogen from/to ground state have been considered from the database of Biagi [159]. The excitation/de-excitation process involving other excited states of N_2 was taken from Bacri and Medani [160].

Electronic excitation of nitrogen atom (e-E-N)

All the processes coupling two excited states of N were taken into account:

$$e^- + N(Y) \rightarrow e^- + N(Z) \qquad \text{(R 4.3)}$$

where Y and Z belongs to the 27 electronically excited states of N-atom. The cross-section data for these processes have been taken from the B-spline R-matrix (BSR) calculations performed for electron-impact excitation and ionization of nitrogen [161].

Electron-impact dissociation (e-D)

Electron impact dissociation was taken into account form both the ground and metastable states. The dissociation from the vibrational levels of the ground states is mainly through the pre-dissociation processes following the excitations to electronic states, the cross-section data for which is taken from Phsy4entry database [158]

$$e^- + N_2(X^1\Sigma^+_g,v) \rightarrow e^- + N(^4S^o) + N(^2D^o) \text{ with } v = 0\text{-}48 \qquad \text{(R 4.4)}$$

While the dissociation from the electronic excites states are not very important, they have been taken into account through the data proposed by Teulet et al. [162] as tabulated in Table 4.4.

Table 4.4: Electron impact dissociation reactions

Process	a	b	c	
$N_2(A^3\Sigma^+_u) + e \rightarrow 2N + e$ [162,163]	0.039812	2.98	41669.6	(R 4.5)
$N_2(B^3\Pi_g) + e \rightarrow 2N + e$ [162,163]	$2.71035 \cdot 10^{-5}$	3.73	55586.8	(R 4.6)
$N_2(a'^1\Sigma^-_u) + e \rightarrow 2N(^2D^o) + e$ [162,163]	$1.3575842 \cdot 10^{13}$	-0.5	71166	(R 4.7)
$N_2(C^3\Pi_u) + e \rightarrow 2N + e$ [162,163]	$3.095822 \cdot 10^{-3}$	3.27	12892.7	(R 4.8)

Electron-impact ionization (e-I)

This was treated in a similar way as the dissociation with a set of N_2 ionization processes form the different vibrational levels of the electronic ground state, N_2 ionization from electronically excited states and N-atom ionization from the electronically excited states. The considered processes are therefore:

$$e^- + N_2(X^1\Sigma^+_g,v) \rightarrow 2e^- + N_2^+ \text{ with } v=0\text{-}48 \quad \text{(R 4.9)}$$

$$e^- + N_2(Y \neq X^1\Sigma^+_g) \rightarrow 2e^- + N_2^+, \; Y= A^3\Sigma^+_u, B^3\Pi_g, C^3\Pi_u \text{ and } a'^1\Sigma^-_u \quad \text{(R 4.10)}$$

$$e^- + N(Y) \rightarrow 2e^- + N^+ \quad \text{(R 4.11)}$$

with Y = $^2D^o$ or $^2P^o$. The cross section data were taken from Phys4entry database [158] for processes (R 4.9), Bacri and Medani [160] for process (R 4.10) and BSR [161] database for process (R 4.11).

Vibrational relaxation processes

Vibrational relaxation kinetics may be of prime importance for moderate pressure (<10 mbar) microwave plasmas [104]. This kinetics may represent the major electron energy dissipation channel, a significant gas heating channel and a major dissociation route through heavy species collisions with the upper vibrational levels. Further, the vibrational distribution function may significantly deviate from a Boltzmann distribution under moderate pressure discharge conditions. A detailed modelling of the vibrational kinetics is therefore necessary for predicting the population of the upper vibrational levels and their subsequent contribution to the dissociation and ionization kinetics. The vibration kinetics considered in the model developed in this work distinguishes three sets of processes.

Vibration-vibration relaxation processes (v-v processes)

We only consider to be possible a single quantum jump process of the form

$$N_2(X^1\Sigma^+_g,v) + N_2(X^1\Sigma^+_g,w\text{-}1) \rightarrow N_2(X^1\Sigma^+_g,v\text{-}1) + N_2(X^1\Sigma^+_g,w) \quad \text{(R 4.12)}$$

The rate constant for these processes were investigated by several authors and we used the rate expressions suggested by Capitelli *et al*. [104], which are the most commonly accepted by the community.

Vibration-translation relaxation processes (v-t processes)

These involve energy transfer between the vibrational mode of N_2 molecule and the translational mode of N_2-molecule (v-t-N_2) and N-atom (v-t-N). The v-t processes can be described as:

$$N_2(X^1\Sigma^+_g,v) + N_2 \leftrightarrow N_2(X^1\Sigma^+_g,w) + N_2 \quad \text{(R 4.13)}$$

$$N_2(X^1\Sigma^+_g,v) + N \leftrightarrow N_2(X^1\Sigma^+_g,w) + N \quad \text{(R 4.14)}$$

As a matter of fact, reactive N- N_2 collisions, may lead to multi-quantum jump de-excitation, *i.e.* $|v-w|>1$, and enhanced energy transfer probabilities as compared to the non-reactive transfer channel. Of these, the collisions of upper vibrational levels with N-atom v-T-N are found to be very strong. In spite of this, there exists less clarity with regard to the reaction rates for this process [115,164]. As a matter of fact, the v-T-N rate constants published in the literature show a fairly large discrepancy [115]. This was analyzed by Guerra et al. [115] and based on the comparison between experiments and simulation of the pink afterglow of nitrogen DC discharges, suggest that the rate constants values calculated for v-T-N processes using Quasi-Classical Theory (QCT) approach are subject to large uncertainty and are overestimated for the moderate to low gas temperature values encountered in most of non-equilibrium conditions, i.e., typically $T_g < 1000$ K. The choice of v-T rate constants will impact the vibrational distribution and as a consequence affects the rate of dissociation. In our present model, we have incorporated the reaction rate model suggested by [115].

Vibration-dissociation processes (v-D processes)

This set of reactions consists of all the process involving collisions between heavy species involving the upper vibrational levels of $N_2(X^1\Sigma^+_g)$ and ending up with the dissociation of N_2. It is worthy to mention here that the upper vibrational level of $N_2(X^1\Sigma^+_g)$, *i.e.* v=48, is the last level with a vibrational energy, as estimated from a second order anharmonic oscillator model, just below the dissociation limit, *i.e.* higher levels are above the dissociation limit and can be considered as dissociated. Of course, using higher order anharmonic oscillator model would results in larger value for the upper vibrational level of $N_2(X^1\Sigma^+_g,v)$. This may slightly affect the vibrational kinetics and more specifically the dissociation kinetics of the upper vibrational. The v-D processes considered in this model are shown in the next page:

$$N_2(X^1\Sigma^+_g,v) + N_2 \rightarrow 2N + N_2 \quad \text{(R 4.15)}$$

$$N_2(X^1\Sigma^+_g,v) + N \rightarrow 2N + N \quad \text{(R 4.16)}$$

$$N_2(X^1\Sigma^+_g,v) + N_2(X^1\Sigma^+_g,w_{max}) \rightarrow N_2\ (X^1\Sigma^+_g,v\text{-}1) + 2N \quad \text{(R 4.17)}$$

Note that although processes (R 4.15) and (R 4.16) are considered for all the vibrational levels, only the upper levels will effectively contribute to the dissociation kinetics.

The rates of these processes are determined using similar expressions as those for v-t and v-v processes [104,164].

Collisional, radiative processes involving electronically excited states and ions

Radiative processes are taken into account when required for the N and N_2 electronically excited states involved in the model. The plasmas investigated are considered to be optically thin and the emission coefficients, *i.e.* Einstein coefficients, are taken from Kossyi et al [165] for N_2 and lines from NIST database for N [163]. Quenching processes [165], pooling reactions [165] and associative ionization [165] involving excited states were also taken into account. Ion conversion between N_4^+, N_2^+ and N^+ and dissociative recombination are also considered [113]. The reactions involved in the model are listed below, with radiative processes (Table 4.5), ion conversion and dissociative recombination (Table 4.6) and pooling reactions, associative ionization and collisional de-excitation (Table 4.7).

Table 4.5: Radiative processes included in the model

Process	Reaction rate	Reaction number
$N_2(B^3\Pi_g) \rightarrow N_2(A^3\Sigma^+_u) + h\nu$	$A_{ij} = 1.5\times10^5$	(R 4.18)
$N_2(C^3\Pi_u) \rightarrow N_2(B^3\Pi_g) + h\nu$	$A_{ij} = 3\times10^7$	(R 4.19)
$N(i) \rightarrow N(j<i) + h\nu$	NIST [166]	(R 4.20)

Table 4.6: Ion conversion and dissociative recombination reactions taken into account.

Process	**a**	**b**	**c**	
$N_2^+ + e \rightarrow 2N$ [165]	5.0075×10^{12}	-0.5	7.1166×10^{4}	(R 4.21)
$N_2 + N_4^+ \rightarrow 2N_2 + N_2^+$ [165]	$A_2 \cdot e^{(A_0 \cdot T - A_1)}$, with $A_0 = 0.0036$; $A_1 = 15.68$ K; $A_2 = 6.023\times10^{17}$ mol m^{-3}			(R 4.22)
$N + N_2^+ \rightarrow N^+ + N_2$ [165]	1.44552×10^{3}	1	0	(R 4.23)
$N_2 + N^+ \rightarrow N_2^+ + N$ [155]	1.005841×10^{5}	0.81	1.3×10^{4}	(R 4.24)
$N + N_3^+ \rightarrow N_2^+ + N_2$ [165]	397518×10^{7}	0	0	(R 4.25)
$e + N_3^+ \rightarrow N_2 + N$ [165]	2.0864×10^{12}	-0.5	0	(R 4.26)
$e + N_4^+ \rightarrow 2N_2$ [165]	2.0864×10^{13}	-0.5	0	(R 4.27)
$2e + N_2^+ \rightarrow e + N_2$ [165]	8.44994×10^{3}	-4.5	0	(R 4.28)
$2e + N^+ \rightarrow e + N$ [165]	8.44994×10^{3}	-4.5	0	(R 4.29)

Table 4.7: Pooling reactions, associative ionization and collisional de-excitation processes considered in this work

Process	a	b	c	
$2N_2(a'^1\Sigma^-_u) \rightarrow N_4^+ + h\nu$ [165]	1.2046×10^8	0	0	(R 4.30)
$N_2(A^3\Sigma^+_u) + N_2(a'^1\Sigma^-_u) \rightarrow N_2 + N_2^+ + e$ [107,165]	3.0115×10^7	0	0	(R 4.31)
$N_2^+ + N_2(A^3\Sigma^+_u) \rightarrow N_3^+ + N$ [165]	1.8069×10^8	0	0	(R 4.32)
$N(^2D^o) + N(^2P^o) \rightarrow N_2^+ + e$ [165]	6.023×10^5	0	0	(R 4.33)
$N + N_2(A^3\Sigma^+_u) \rightarrow N_2 + N(^2P^o)$ [104]	3.0115×10^7	0	0	(R 4.34)
$N + N_2(a'^1\Sigma^-_u) \rightarrow N_2(B^3\Pi_g) + N$ [107]	6.023×10^7	0	0	(R 4.35)
$N + N_2(A^3\Sigma^+_u) \rightarrow N_2(X^1\Sigma^+_g, v < 10) + N$ [165]	3.0115×10^7	0	0	(R 4.36)
$N(^2D^o) + N_2 \rightarrow N + N_2$ [165]	3.6138×10^3	0	0	(R 4.37)
$N + N(^2P^0) \rightarrow N(^2D^0) + N$ [165]	1.08414×10^6	0	0	(R 4.38)
$N(^2P^0) + N_2 \rightarrow N + N_2$ [104]	1.2046	0	0	(R 4.39)
$N(^2P^0) + N_2 \rightarrow N(^2D^0) + N_2$ [165]	1.2046	0	0	(R 4.40)
$N_2 + N_2(B^3\Pi_g) \rightarrow 2N_2$ [107]	1.8069×10^7	0	0	(R 4.41)
$N_2 + N_2(B^3\Pi_g) \rightarrow N_2(A^3\Sigma^+_u) + N_2$ [165]	3.0115×10^7	0	0	(R 4.42)
$N_2 + N_2(C^3\Pi_u) \rightarrow N_2(a'^1\Sigma^-_u) + N_2$ [165]	6.023×10^6	0	0	(R 4.43)
$N_2 + N_2(a'^1\Sigma^-_u) \rightarrow N_2(B^3\Pi_g) + N_2$ [165]	12046×10^5	0	0	(R 4.44)
$N_2 + N_2(A^3\Sigma^+_u) \rightarrow N_2 + N_2(B^3\Pi_g, v > 5)$ [107]	6.023×10^7	0	0	(R 4.45)
$N_2(X^1\Sigma^+_g, v \geq 6) + N_2(A^3\Sigma^+_u) \rightarrow N_2(B^3\Pi_g) + N_2(X^1\Sigma^+_g, v - 6)$ [107]	6.023×10^7	0	0	(R 4.46)
$N_2(X^1\Sigma^+_g, v \geq 24) + N_2(a'^1\Sigma^-_u) \rightarrow N_2 + N_2^+ + e$ [107]	3.6138×10^4	0	0	(R 4.47)
$2N_2(A^3\Sigma^+_u) \rightarrow N_2(B^3\Pi_g) + N_2(X^1\Sigma^+_g, v = 8)$ [107]	1.92736×10^8	0	0	(R 4.48)
$2N_2(A^3\Sigma^+_u) \rightarrow N_2(C^3\Pi_u) + N_2(X^1\Sigma^+_g, v = 2)$ [107]	156598×10^8	0	0	(R 4.49)
$N_2(A^3\Sigma^+_u) + N_2 \rightarrow N_2 + 2N$ [155]	7.016×10^{15}	-1.6	4.1057×10^4	(R 4.50)
$N_2(B^3\Pi_g) + N_2 \rightarrow N_2 + N(^2D^0) + N$ [155]	7.016×10^{15}	-1.6	5.5175×10^4	(R 4.51)

4.2.3 Surface processes

As far as surface processes are concerned, only recombination and de-excitation reactions were taken into account, i.e., the wall is assumed to be only catalytic and non-reactive. The

heterogeneous net production rate, R_{s-w}, is estimated from the balance between the diffusion flux and the net surface reaction [96]:

$$\frac{D_s}{\delta_s}\left(C_{s-g} - C_{s-w}\right) = \frac{R_{s-w}}{M_s} = -\gamma\frac{v_s^*}{4}n_{s-w} + \sum_{l\neq s}\alpha_{sl}r_l \qquad (4.3)$$

where D_s, δ_s, γ, v_s^* are the diffusion coefficient, the diffusion boundary layer thickness, the recombination coefficient and the thermal velocity at the reactor for species s. C_{s-g} and C_{s-w} are the concentrations [mol m^{-3}] of species *'s'* at the reactor wall. α_{sl} is the stoichiometric coefficient of species 's' in the catalytic recombination reaction of species 'l' and r_l is the rate of catalytic recombination of species 'l'. R_{s-w} is the rate *'s'* species reaction at the wall per unit wall surface [96]. The corresponding volumetric rate W_{s-w} actually required in the species balance equations of this quasi-homogeneous model is obtained from the product of R_{s-w} with the ratio of the wall surface to the plasma volume and the reverse of the molar mass of the species *'s'* M_s, *i.e.* W_{s-w}= $\frac{R_{s-w}}{M_s}\frac{S_{wall}}{V_{plas}}$.

The large efforts spent on the investigation of surface processes [167–170] emphasized the difficulty to setup simple kinetic data even for simple surface processes with a single element such as atoms recombination coefficients that depends not only on the wall material and temperature but also on the surface state and the discharge conditions since ion bombardment may assist recombination or desorption [167–170]. In this work we assumed that the recombination coefficients of ions are all equals to 1, and that the recombination of molecular ions is dissociative. The loss of all N_2 and N electronically excited states are mainly due to radiative de-excitation. The contribution of surface processes in these losses is not significant and the plasma composition is not sensitive to the value adopted for the surface de-excitation coefficients of these states which were set to one. The surface process of N atom excited states N(^{2}D^o) and N(^{2}P^o) are known to de-excite strongly at the wall to produce N-atom. The N-atom recombination coefficient, which is of prime importance for the present study, was adjusted such that the N-atom densities are closer to the experimentally determined values. The de-excitation coefficients of upper vibrational states are usually fairly low [156] and value of 10^{-3} was assumed for these processes. Following reference [156], we also assumed that the de-excitation process that requires strong interaction between the N_2-molecule and the surface thus leading to a full thermal equilibration with the surface results in the production of v = 0 level. The summary of all the surface reactions are tabulated in Table 4.8.

Table 4.8: Surface reactions included in the model

Surface reactions	γ	
$N(^4S^o) \rightarrow 0.5N_2(X^1\Sigma^+_g,0)$	10^{-1}-10^{-4}	(R 4.52)
$N^+ + e \rightarrow N$	1.0	(R 4.53)
$N_2^+ + e \rightarrow N_2$	1.0	(R 4.54)
$N_3^+ + e \rightarrow N + N_2$	1.0	(R 4.55)
$N_4^+ + e \rightarrow N_2 + N_2$	1.0	(R 4.56)
$N(^2D^o, ^2P^o) \rightarrow N$	0.5	(R 4.57)
$N(^2D^o, ^2P^o) \rightarrow 0.5N_2$	0.5	(R 4.58)
$N_2(X^1\Sigma^+_g,v) \rightarrow N_2(X^1\Sigma^+_g,0)$	10^{-3}	(R 4.59)

4.2.4 Energy equation

The estimation of the gas phase source terms requires the determination of the gas temperature and the electron energy distribution function (EEDF) that govern the heavy-species/heavy-species and electron-impact reaction rate constants, respectively. Therefore, the species balance equation (4.1) is coupled to a total energy balance equation that yields the gas temperature [171] and the two-term expansion of the homogeneous electron Boltzmann equation as described in reference [96,157].

In the present model, the EEDF, is determined from the time dependent electron Boltzmann equation for electron. The electron energy is discretized into uniform bins and the EEDF f(ε) for electron energy ε is given by

$$\frac{df(\varepsilon)}{dt} = -\frac{dJ_E}{d\varepsilon} - \frac{dJ_{e-h}}{d\varepsilon} + In_\varepsilon \tag{4.4}$$

where J_E and J_{e-h} are the electron fluxes in the energy space due to electric field heating and elastic collisions respectively while In_ε refers to the rate of production of electrons with energy ε due to inelastic collision. All the different inelastic collisions discussed in the previous section have been considered for obtaining the EEDF. The solution of the electron Boltzmann equation requires the knowledge of the reduced electric field, *i.e.* E/n where E is the electric field and *'n'* the neutral density. However, this is not directly realizable in microwave discharges where one has rather access to the microwave power input in the system and can estimate the microwave power that is actually coupled in the plasma. However the key-parameter that appears in the energy balance

equation and the electron energy equation, as far as quasi-homogeneous plasma model is concerned, is the absorbed power density P_{MW} [157]. Knowing the microwave power density P_{MW}, one may access to the reduced electric field through an overall energy balance on the electron kinetic mode:

$$P_{MW} = \frac{\omega_p^2 \vartheta_m}{\vartheta_m^2 + \omega_{MW}^2} E^2 \tag{4.5}$$

where ω_p and ω_{MW} is plasma and MW frequency respectively and ϑ_m is the momentum transfer frequency of electron collisions with gas particles.

The above equation is therefore coupled to the species, energy and Boltzmann equations.

The total energy equations used in this work is very similar to the one used for hydrogen plasmas in references [96] which can be written as

$$\sum_{s \neq e} \rho \left\{ Y_s Cp_s \frac{dT_g}{dt} + h_s \frac{dY_s}{dt} \right\} + \rho Cp_e \frac{dY_e T_e}{dt} = P_{MW} - \lambda \frac{T_g - T_w}{\delta_t} - \sum_s h_s W_{s-w} \tag{4.6}$$

where Cp_s and h_s is the specific heat and enthalpy of formation of heavy species *'s'*. Cp_e refers to the electron specific heat, while λ and δ_t are the thermal conductivity of the heavy species and the thermal boundary layer while P_{MW} is the absorbed MW power density defined as the ratio of the absorbed power to plasma volume. Under stationary conditions, the MW power is balanced by the heat loss due to conduction and catalytic reactions at the wall. The thermal conductivity of the plasma is estimated using the Lennard-Jones potential [96].

It is noteworthy that one of the peculiarities of the present model consists in solving for the full ionization kinetics, i.e., the electron density n_e is not specified. This is slightly different from similar works on the non-equilibrium kinetics in microwave plasma where the electron density is usually prescribed and the reduced electric field is related to the so-called parameters that represents the power dissipated per electron in the plasma is inferred for a prescribed value of the reduced electric field give the power density, *i.e.* n_e represents the power density.

4.2.5 Solution procedure

The transient quasi-homogeneous plasma model used in this study has been solved using DVODE solver [172]. These equations are solved for specified plasma pressure, microwave power density, and wall temperature. The electron Boltzmann equation is discretized in the energy space

and the non-linear algebraic system resulting from the obtained equations along with species and total energy equations are solved for each time step. There are two modes of operation of the model i.e. stationary and pulsed mode. In the stationary mode, the transient simulations are carried out until the plasma properties do not change by more than the specified tolerance. For the pulsed mode operation, the simulations are carried out, for a specified cycle time t_c and duty cycle Φ the fraction of time of MW power on to MW power off, until the time-averaged plasma properties over one pulse cycle converge. In order to enable the transient calculation at MW power off or low phase, the MW power of low phase is fixed at a very small power density which was generally up to three orders of magnitude lower than the plasma on phase.

4.3 Conclusions

The present chapter has introduced the collisional 0D radiative model for N_2 MW plasmas along with the list of different processes that have been considered. The chosen kinetic model is based on a critical review of the literature, in order to select the most relevant and reliable data available so far. The present model will be extensively used in later chapters to understand the chemical kinetics accompanying the stationary and pulsed MW plasmas investigated in the present thesis. It is proper to recall that this homogeneous model does not aim to describe the transport of active species, as a 1D or a 2D model would do, but compared to the latter it has the advantage to give a solid insight on the chemistry with a very reasonable calculation time within few hours. This model is then designed to be a support for the interpretation of experimental results and has no ambition to predict the optimal conditions in which the experiments should be performed.

Chapter 5 –Stationary MW plasmas

5.1 Introduction

This chapter will present the characteristics of nitrogen and hydrogen plasmas under stationary conditions for SAIREM® Hi-Wave (non-magnetized) MW source for pressures between 20 Pa to 150 Pa and MW power ranging from 20 W to 180 W. This will be followed by a discussion on the chemical kinetics of the nitrogen plasma, in order to identify the important processes leading to the dissociation of nitrogen molecules under these conditions.

5.2 First Positive System emission of molecular nitrogen

In our measurements, in addition to the fluorescence from excited N atoms during TALIF, the First Positive System (FPS) is also recorded. The excited states of N_2, $A^3\Sigma^+_u$, $B^3\Pi_g$ and $C^3\Pi_u$, are known to exist in a collisional and radiative kinetic loop through the following processes [107,165]:

$$N_2(B^3\Pi_g) \rightarrow N_2(A^3\Sigma^+_u) + h\nu \quad \text{(R 5.1)}$$

$$N_2(C^3\Pi_u) \rightarrow N_2(B^3\Pi_g) + h\nu \quad \text{(R 5.2)}$$

$$N_2 + N_2(B^3\Pi_g) \rightarrow N_2(A^3\Sigma^+_u) + N_2 \quad \text{(R 5.3)}$$

$$N_2 + N_2(A^3\Sigma^+_u) \rightarrow N_2 + N_2(B^3\Pi_g, v > 5) \quad \text{(R 5.4)}$$

$$N_2(X^1\Sigma^+_g, v \geq 6) + N_2(A^3\Sigma^+_u) \rightarrow N_2(B^3\Pi_g) + N_2(X^1\Sigma^+_g, v - 6) \quad \text{(R 5.5)}$$

$$2N_2(A^3\Sigma^+_u) \rightarrow N_2(B^3\Pi_g) + N_2(X^1\Sigma^+_g, v = 8) \quad \text{(R 5.6)}$$

$$2N_2(A^3\Sigma^+_u) \rightarrow N_2(C^3\Pi_u) + N_2(X^1\Sigma^+_g, v = 2) \quad \text{(R 5.7)}$$

In fact, these processes are known to be responsible for the appearance of the afterglow in N_2 plasma [54,173,174]. Thus, the recorded FPS emission is indicative of the line of sight averaged densities of N_2 excited states. As electron impact processes are dominant in the conditions of our study, these excited states of N_2 are produced in the core of the plasma predominantly by:

$$e^- + N_2(X^1\Sigma^+_g) \rightarrow e^- + N_2(Z) \quad \text{(R 5.8)}$$

where Z = $A^3\Sigma^+_u$, $B^3\Pi_g$, and $C^3\Pi_u$ and hence, the FPS emission can be used as an indicator of the electron densities.

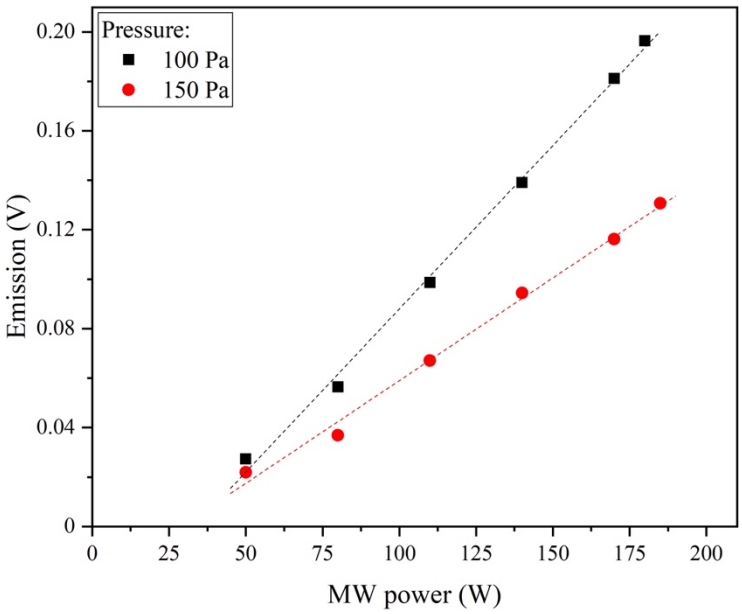

Figure 5.1: FPS emission as a function of MW power and pressure. Experiments were performed analyzing a volume 10 mm far from plasma source at pressures of 100 Pa and 150 Pa and plasmas sustained in powers between 50 W and 185 W.

Figure 5.1 shows the variation of FPS intensities at a spatial location of 10 mm from the source as a function of power at pressures of 100 Pa and 150 Pa. At both pressures, the FPS intensities show a linear variation as a function of power. As the electron temperature is mainly influenced by the inelastic collisions, its values are not expected to vary significantly with MW power at a given pressure. Therefore, the increase in the MW power at a fixed pressure should result in an increase in electron density, strengthening our hypothesis that there is a direct correlation between FPS emission and electron densities. The FPS emission are seen to decrease with pressure owing to faster collisional quenching of the excited states $N_2(B^3\Pi_g)$.

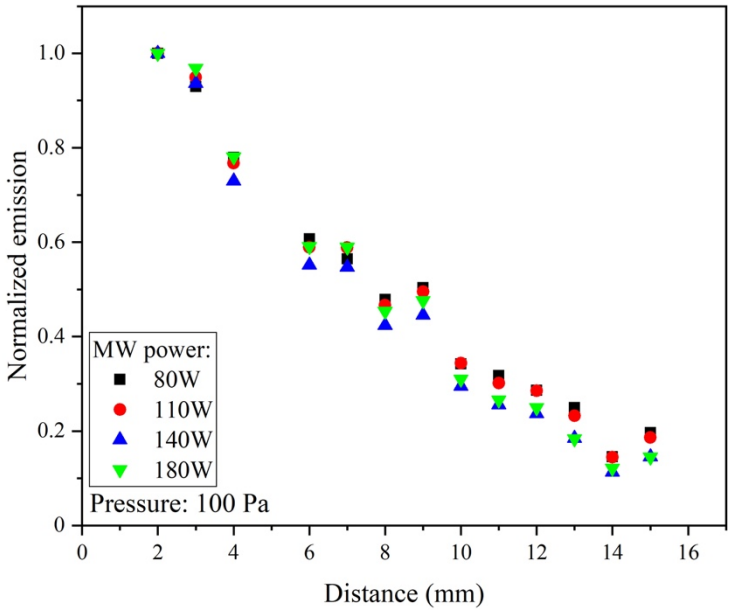

Figure 5.2: Normalized FPS emissions averaged on the laser-source distance shown for different power conditions, namely 80 W, 110 W, 140 W and 180 W, in 100 Pa plasmas.

Figure 5.2 shows the spatial variation of normalized FPS intensities as a function of power at a fixed pressure of 100 Pa. Firstly, the normalized intensities are seen to have self-similar profiles for all powers. This is indicative of MW coupling to be independent of injected MW power at this pressure. Further, the FPS emissions are seen to decrease steeply with distance from the source, indicating localization of electrons close to the ceramic surface. In fact, the MW power density is expected to achieve maximum close to the ceramic surface, resulting in production of electrons and sustaining the plasma in this region [117]. Further, the normalized FPS emissions at 100 Pa and 150 Pa are similar, as shown in Figure 5.3. The similarity of the emission profiles is indicative that the MW plasma coupling is similar for the examined pressures.

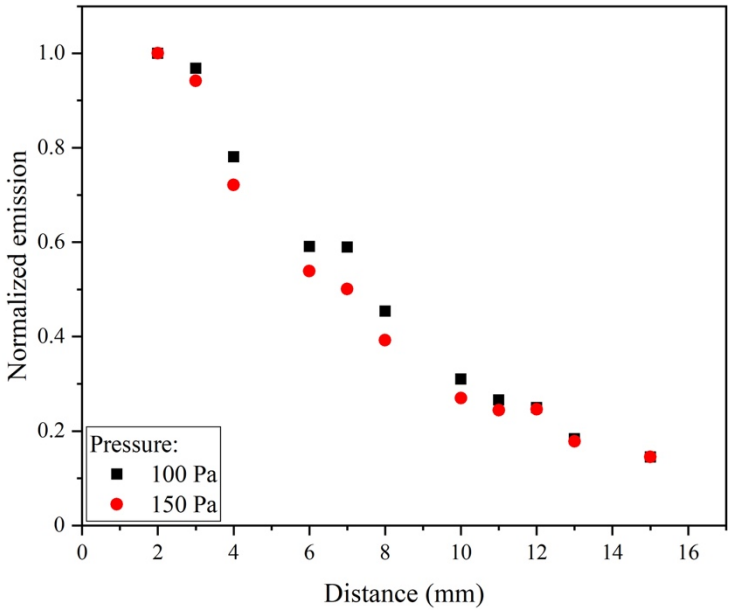

Figure 5.3: Normalized FPS emissions averaged on the laser-source distance shown for 100 Pa and 150 Pa at 180 W of MW power

5.3 Gas temperature

Gas temperature values measured for nitrogen and hydrogen plasmas generated using Hi-Wave are shown in Figure 5.4. These measurements have been performed at a distance of 14 mm from the ceramic surface of the plasma source. As it is better explained in section 5.5, the plasma volume has been assumed as a hemisphere of radius 3 cm. Therefore, a location sampled at 14 mm from the source's surface can be considered a good estimator of the average plasma temperature in the whole volume.

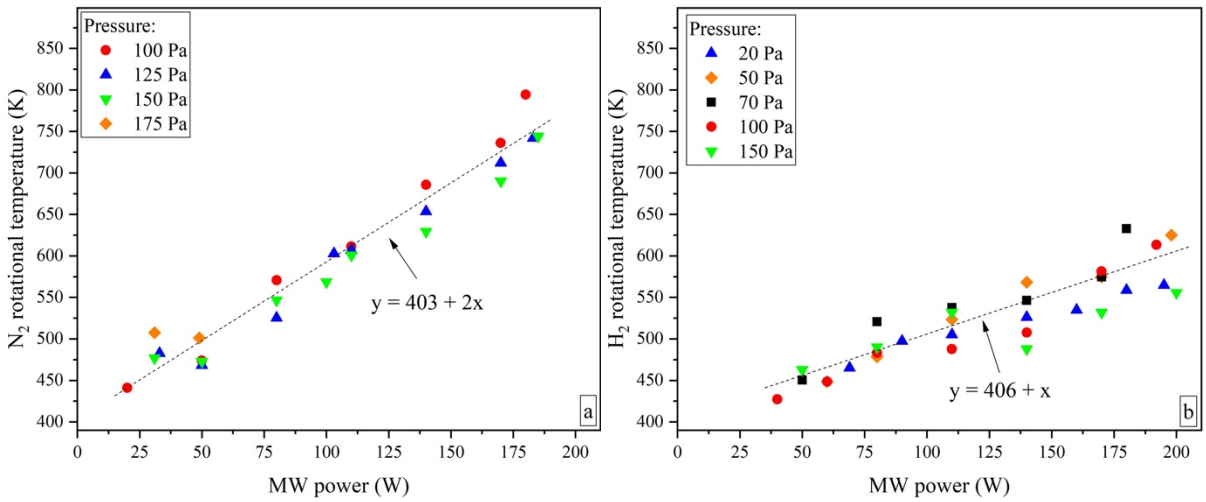

Figure 5.4: Rotational temperatures of (a) N_2 plasmas and (b) H_2 plasmas generated with SAIREM® Hi-Wave source.

The rotational temperatures display a linear relationship with MW power, with nitrogen having slopes greater (factor of 2) than those of hydrogen plasmas. The different values of temperature observed clearly depend on the nature of the targeted gases. The systematically lower temperature values recorded in hydrogen plasmas than those of nitrogen at a given MW power condition have to be attributed to the higher thermal conductivity *k* of hydrogen as compared to that of nitrogen. To give an idea, in standard conditions (*i.e.* atmospheric pressure and temperature of 298 K) the value of hydrogen thermal conductivity k_{H_2} is one order of magnitude greater than k_{N_2}, since k_{H_2} = 0.1897 W m^{-1} K^{-1} and k_{N_2} = 0.02598 W m^{-1} K^{-1}. Plasmas with higher thermal conductivity will attain lower gas temperatures to dissipate the same absorbed MW power to the surrounding colder walls.

The gas temperature is directly proportional to the pressure at constant injected power in the reactor as the collision processes increase with pressure and tend to reduce the degree of non-equilibrium. However, for the relatively narrow range of pressures explored for the plasma source studied, a weak correlation between gas temperature and pressure for both hydrogen and nitrogen has been observed.

5.4 N-atom and H-atom densities

N-atom densities were found to be spatially homogeneous for the conditions of the study. Figure 5.5 shows the spatial variation of N-atom density and the corresponding FPS emission at 150 Pa and 180 W of MW power. This indicates that N-atom is very diffusive. This should also hold true for H-atom as hydrogen being lighter and much more diffusive than nitrogen. Therefore, it would be sufficient to make atom density measurements of both hydrogen and nitrogen at a single spatial point to characterize the plasma. This has been enforced for all density measurements that follow. Moreover, the S/N ratio for the Hi-Wave source was found to be > 10 for all operating conditions and we did not encounter the problems that were observed for Aura-Wave source.

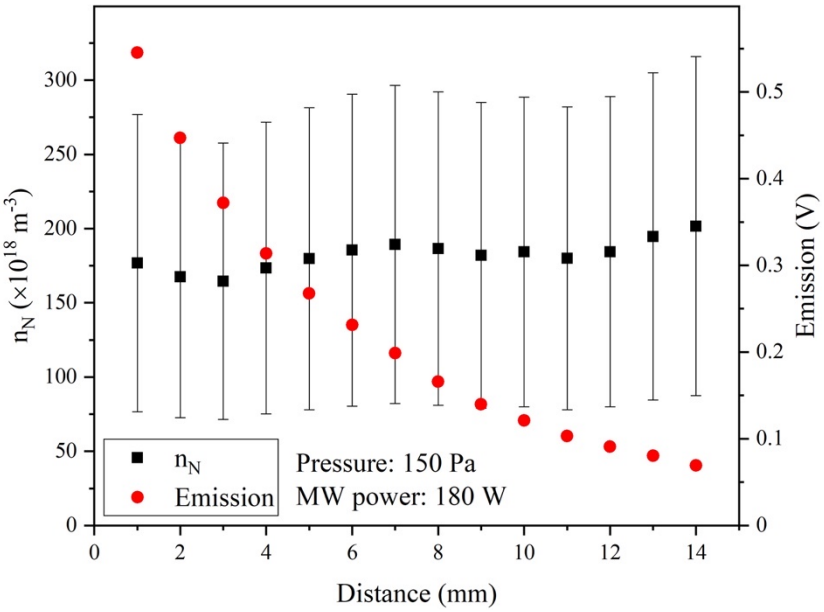

Figure 5.5: Atomic nitrogen density and plasma emission variations with distance from the plasma source.

Figure 5.6 shows the variation of (a) densities and (b) molar fractions of N-atom with MW power and pressure. The N-atom density seems to increase with pressure, while the molar fraction of N-atom displays a linear relationship with MW power, as seen in Figure 5.6a and Figure 5.6b respectively.

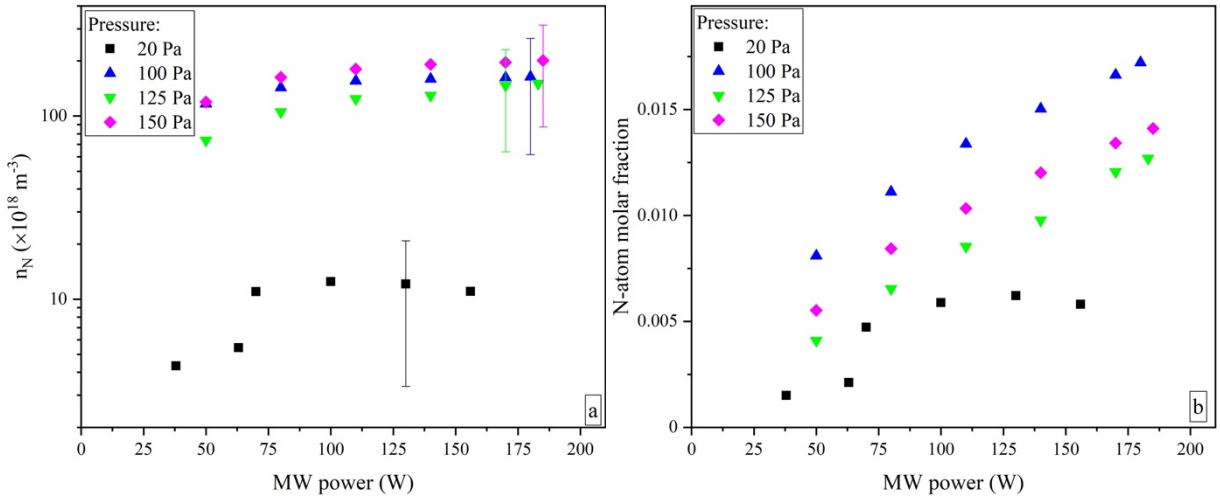

Figure 5.6: (a) Distance averaged N-atom densities and (b) N-atom molar fractions as a function of MW power and pressure.

Figure 5.7 shows the H-atom densities as a function of MW power for different pressures measured at 14 mm from the source surface, highlighting how the densities are directly proportional to the MW power. The behavior of hydrogen was observed to be very similar to that of N-atom. Like that observed in Aura-Wave, H-atom densities were slightly higher than N-atom densities.

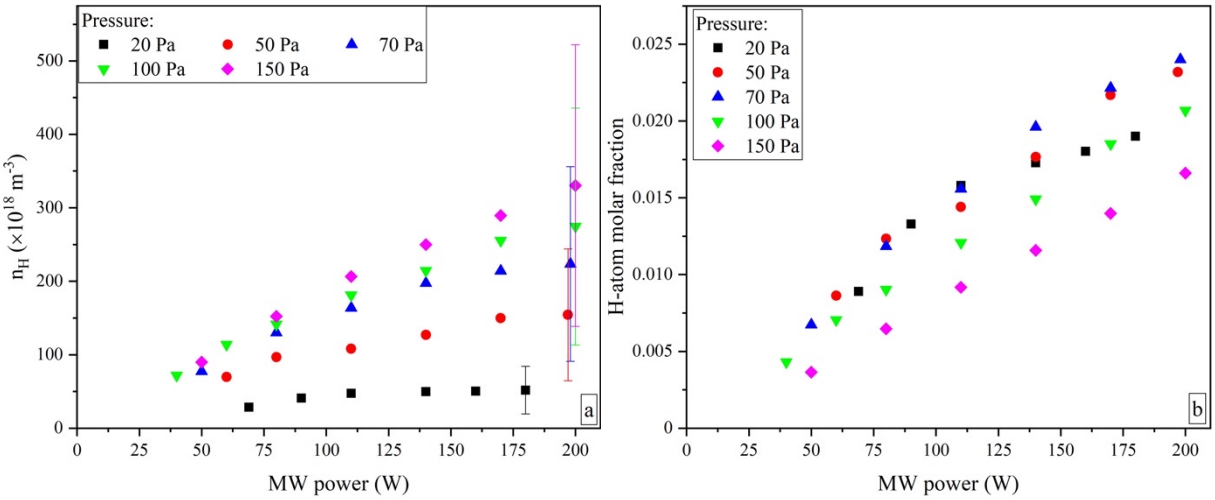

Figure 5.7: (a) H-atom densities and (b) H-atom molar fractions obtained in Hi-Wave plasmas

The efficiency of the sources for dissociating the molecules can be assessed by using the degree of dissociation which for nitrogen is defined as 0.5[N]/[N_2] [175–178]. In order to have the assessment of the performance of Hi-Wave source, comparisons have been made with the degree of dissociations of N_2 and H_2 in plasmas generated by Aura-Wave source. These measurements have been performed at 10 mm far from the magnet. Figure 5.8 compares the degree of dissociation measured for nitrogen and hydrogen plasmas for the two sources, Hi-Wave and Aura-Wave. Hydrogen consistently displays better degree of dissociation when compared to nitrogen irrespective of the sources used. This is consistent owing to the higher bond strength of nitrogen when compared to hydrogen.

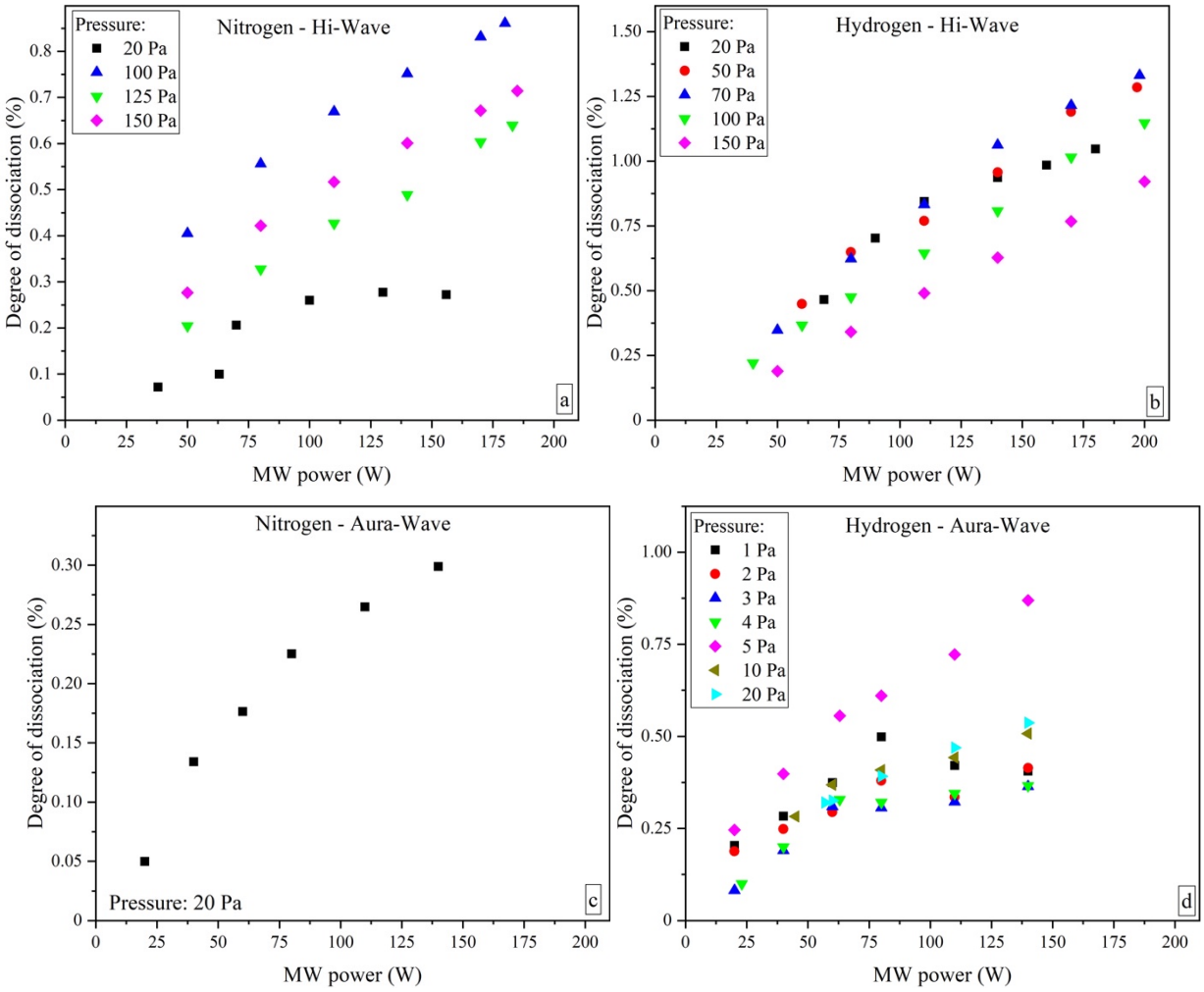

Figure 5.8: Degree of dissociations calculated for both sources studied in this thesis. Results related to Hi-Wave – generated plasmas are represented in (a) and (b), referred respectively to nitrogen hydrogen plasmas, while Aura-Wave plasmas' analysis is illustrated in (c) and (d), indicating nitrogen and hydrogen plasmas respectively.

5.5 Kinetic studies of low pressure N_2 plasmas

In order to gain more insights into the chemical kinetics of the dissociation mechanism in the plasma, the CR model has been used to perform simulations. It has to be noted that the CR model does not take into account of the ECR regime found in Aura-Wave and can be applied for the Hi-Wave source only. In order to tune the CR model to closely mimic the conditions of the plasma source, the parameters such as boundary layer, ratio of volume to surface area and the surface recombination coefficient γ of N-atoms $N(^4S^o)$, *i.e.* reaction (R 5.9), need to be fixed appropriately.

$$N(^4S^o) \rightarrow 0.5N_2(X^1\Sigma^+_g,0) \qquad \text{(R 5.9)}$$

The volume of the plasma in the model is used to quantify the MW power density which directly affects the electron dynamics of the plasma. The surface area signifies all the loss mechanisms of

the plasma source to the cold walls surroundings. The plasma volume signifies the region where most of the MW power is dissipated. Generally, only a fraction of total MW power injected into the plasma is absorbed by the plasma [97,98]. However, this cannot be estimated easily from the experiments, even if some attempts have been recently made on a MW capillary system [179] and on ECR system [152], showing that the MW power really coupled to the plasma is only one third of the injected power. Only fully self-consistent simulations, where the Maxwell's equations for the MW radiation and the fluid model for plasma are solved simultaneously, can give a good estimation of the MW plasma coupling. As the aim of the work is to identify the important processes prevalent in the operating conditions of the plasma source, the CR model with a good estimate of plasma volume should be sufficient. The dimension of the ceramic surface in contact with the plasma is approximately of diameter 40 mm and 10 mm height. On the other hand, the MW power coupling with the plasma can be considered to be significant for distances within 20 mm from the ceramic surface as seen in Figure 5.2. Taking this into account, the plasma has been assumed to be a hemisphere of radius 30 mm which is in contact with a circular surface of 25 mm radius. This assumption is conservative and should be able to capture the essence of the plasma satisfactorily. All the simulations have been performed at a fixed pressure of 100 Pa. As the surface recombination of N-atoms depend on the boundary layer thickness, *i.e.* the diffusion of N-atoms from the plasma bulk to the surface and γ (see equation 4.3), it is necessary to assess these information from the experiments. Unfortunately, the present experiments did not allow determining the gamma value due to uncertainty in the volume and surface, as well as the boundary layer thickness due to highly diffusive N-atoms. Therefore, γ of N-atoms N($^4S^o$) was fixed to 10^{-3} while the boundary layer thickness was tuned such that both the gas temperature and N-atom densities from simulations are in close agreement with the measurements at 100 Pa as shown in Figure 5.9. These simulations should give a qualitative picture of the physico-chemical processes occurring in the plasma.

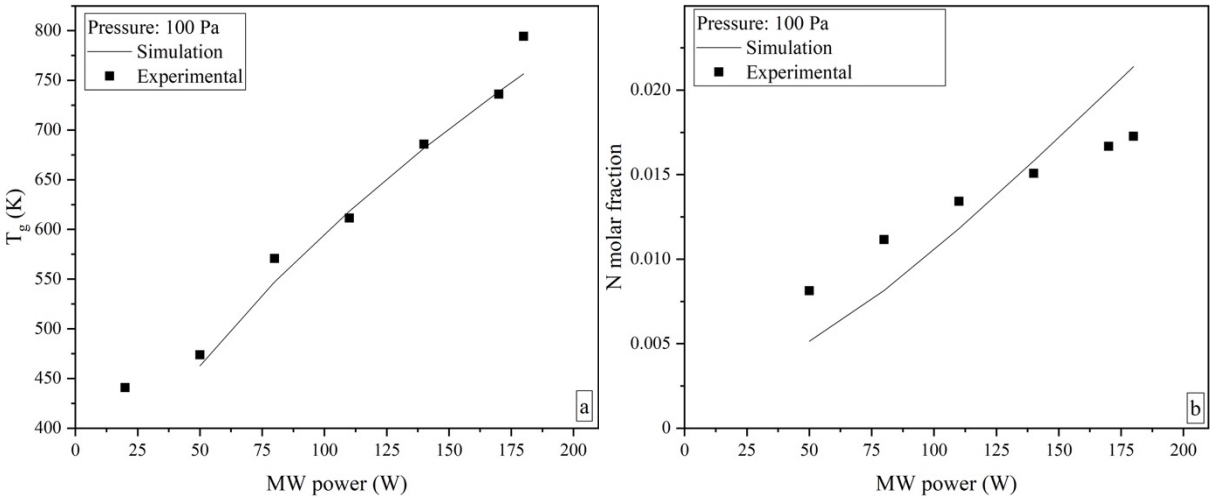

Figure 5.9: Comparison between experimental and simulated values of (a) gas temperature and (b) N-atom molar fractions

The major ions that were found in the plasma is N_2^+. These were mainly formed due to the electron impact ionization of N_2 molecules:

$$e^- + N_2(Y \neq X^1\Sigma^+_g) \rightarrow 2e^- + N_2^+ \qquad \text{(R 5.10)}$$

with Y= $A^3\Sigma^+_u$, $B^3\Pi_g$, $C^3\Pi_u$ and $a'^1\Sigma^-_u$. The next significant ion is N^+ which is about one tenth of the concentration of N_2^+. Figure 5.10 shows the variation of N_e and T_e as a function of MW power. Note that the electron temperature represented here is the average electron energy obtained from the EEDF. Thus, the electron temperature is a result of the frequency of inelastic collisions between electron and heavy particles.

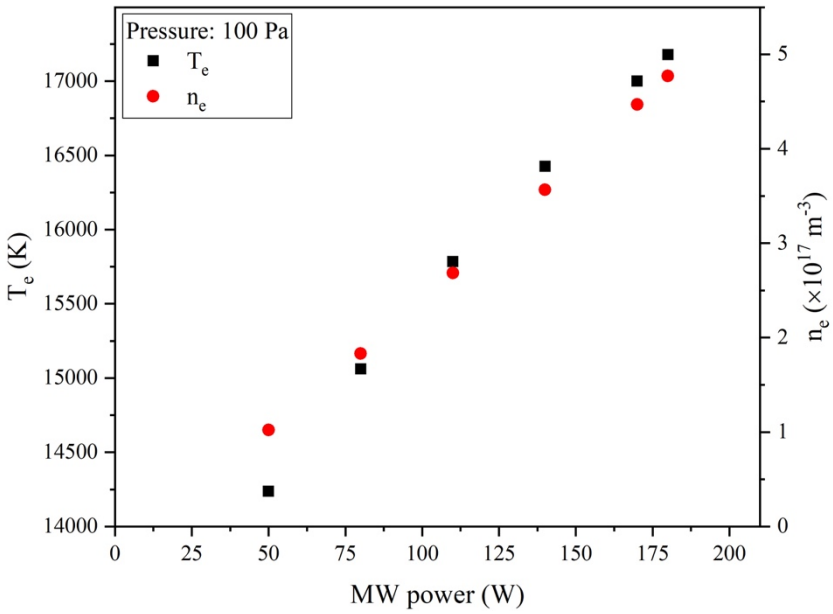

Figure 5.10: electron temperatures and densities estimated by the CR model

Almost all the electronic excited states of N_2 molecule are produced through the electron impact processes and these excited states are consumed mainly through reactions:

$$N_2 + N_2(B^3\Pi_g) \rightarrow 2N_2 \quad \text{(R 5.11)}$$

$$N + N_2(A^3\Sigma^+_u) \rightarrow N_2(X^1\Sigma^+_g, v \leq 10) + N \quad \text{(R 5.12)}$$

Analysis on the reaction rates gives us a branching ratio of approximatively 75% for (R 5.11).

Figure 5.11 shows the densities of Nitrogen molecule excited states $N_2(A^3\Sigma^+_u)$ and $N_2(B^3\Pi_g)$ as a function of pressure and power. The molar fractions of $N_2(A^3\Sigma^+_u)$ and $N_2(B^3\Pi_g)$ are comparable. The molar fraction of these excited states increases linearly with MW power similar to the emissions of FPS observed in the experiments. The excited states are mainly consumed by pooling reactions to the ground state and are not found to be responsible in the dissociation of N_2 molecule at these pressure conditions.

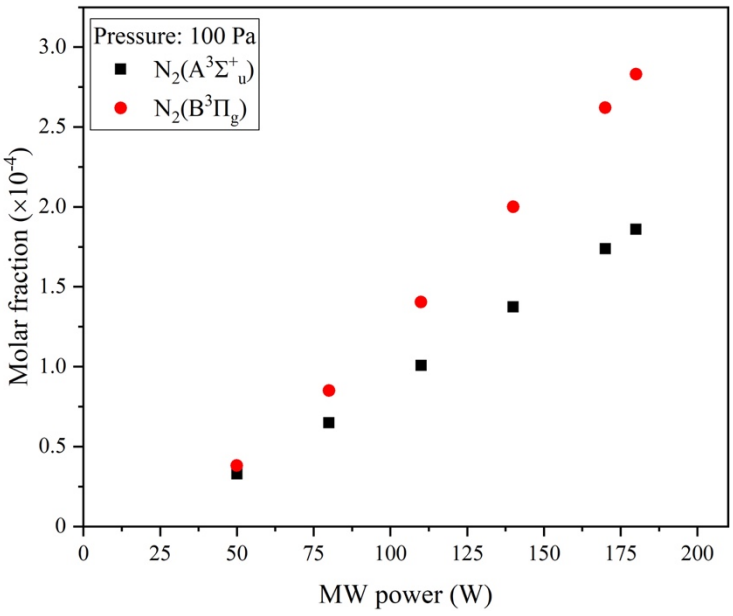

Figure 5.11: $N_2(A^3\Sigma^+_u)$ and $N_2(B^3\Pi_g)$ molar fractions as a function of MW power.

Figure 5.12 shows the different reactions involved in the production and destruction of atomic N at various absorbed MW power. The main consumption of N-atom takes place due to the surface recombination of atomic N at the walls of the reactor. In addition, N-atom undergoes electron impact excitation to N excited states, of which N metastables are the most significant. Although the electron-impact excitation processes are comparable or even greater than the surface recombination

of N-atom, as the meta-stables and the N-atom exist in a quasi-equilibrium, the electron impact excitation process cannot be considered as a major global consumption channel of N-atom.

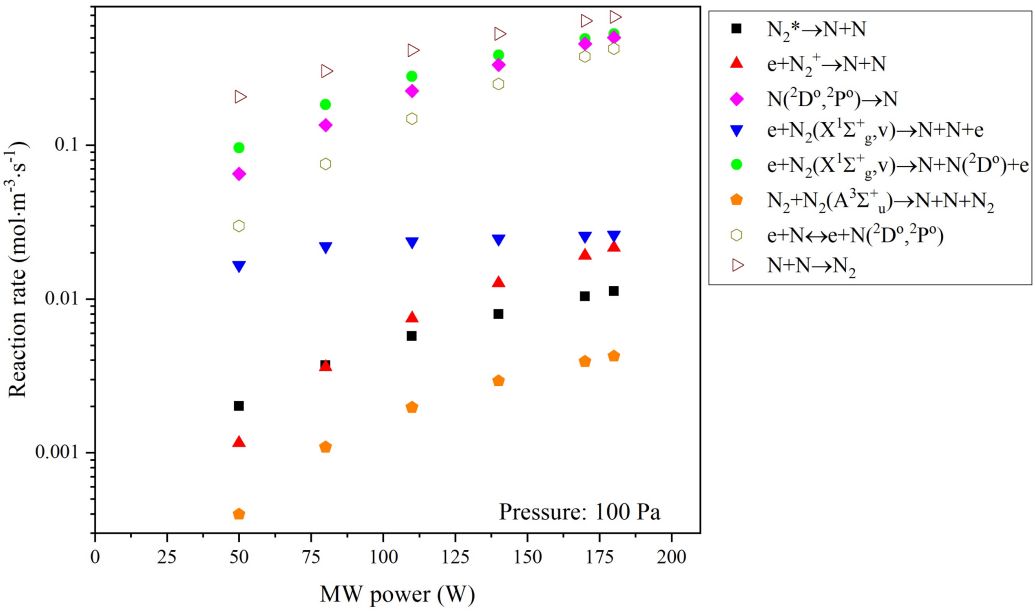

Figure 5.12: Production (filled symbols) and destruction (open symbols) processes of N-atom particles.

Evidently, most of the dissociation of N_2 proceeds through electron impact dissociation (R 5.13) resulting in equal production of N-atom ($N(^4S^o)$) and $N(^2D^o)$.

$$e^- + N_2(X^1\Sigma^+_g,v) \rightarrow e^- + N(^4S^o) + N(^2D^o) \qquad \text{(R 5.13)}$$

with v = 0-48. The dissociation through vibrational dissociation (VD) processes is negligible. Further, the de-excitation of the meta-stables $N(^2D^o)$ and $N(^2P^o)$ at the wall is seen to be equally important production channel of N-atom. The surface de-excitation of the metastables has higher reaction rate compared to the electron impact dissociation. As the major production channel of the meta-stables are through electron driven processes, the densities of these states are strongly impacted by the electron densities. Figure 5.13(left) shows the ratio of densities of N meta-stables to N-atom as a function of MW power. The ratio of these meta-stables increases with injected MW power. Of all the excited states, $N(^2D^o)$ remains the most significant for all conditions, as shown in Figure 5.13(right).

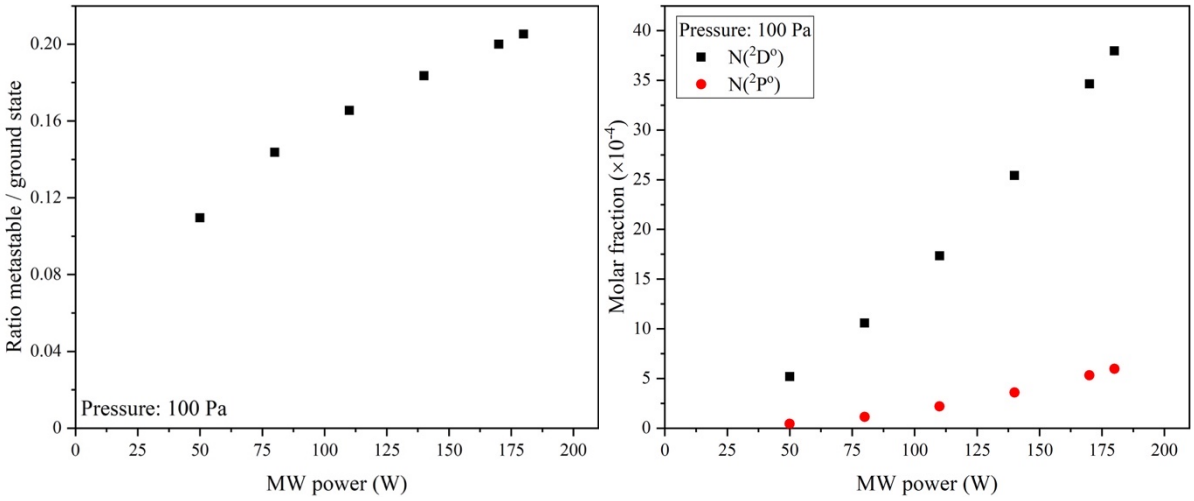

Figure 5.13: (left) N metastable to ground state densities ratios and (right) N metastable states molar fractions as a function of MW power.

Figure 5.14(a) shows the VDF as a function of injected MW power. VDFs show the presence of a Treanor plateau [180] at moderate vibrational levels. This plateau is created through the vibrational ladder mechanisms and results in elevated densities of upper vibrational levels. While the electron impact processes are responsible for populating the initial vibrational levels, the vibrational relaxation, *i.e.* vibrational-vibrational (VV, see reaction (R 4.12)) and vibrational-translational (VT, see reaction (R 4.14)) relaxation, processes are responsible for populating the higher vibrational states and the efficiency of these processes impact the VDF. This implies that the dissociation of N_2 molecule from the upper vibrational levels through electron impact is significant. The reaction rates of electron impact dissociation as a function of MW power and the ground state vibrational level is shown in Figure 5.14(b), indicating the contribution of higher vibrational levels to dissociation is important. The fraction of dissociation coming from higher vibrational levels can be as high as 0.35 as seen in Table 5.1.

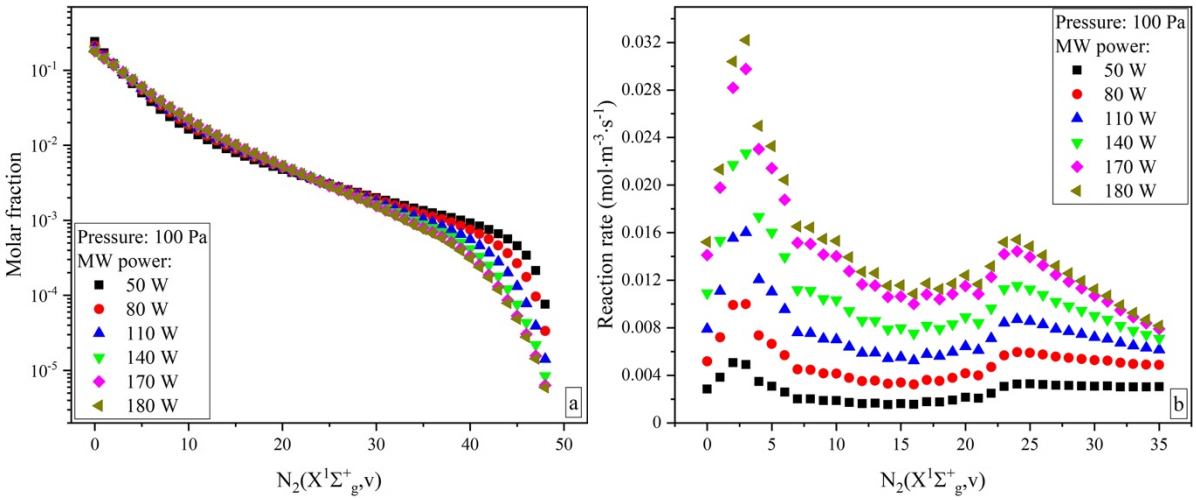

Figure 5.14: (a) VDF as a function of MW power and (b) reaction rates of electron impact dissociation reactions.

Table 5.1: Electron impact dissociation rates ratios of higher vibrational states (v>25) as a function of MW power

MW power (W)	Ratio at 100 Pa
50	0.35646
80	0.31754
110	0.28443
140	0.25891
170	0.23961
180	0.23425

As the power increases, the contribution of upper vibrational levels towards dissociation decreases. This can be explained by the changes in the VDF where the plateau becomes smaller with increasing power. As the gas temperature increases with MW power, the efficiency of VT-N processes also increases [156] which results in the decrease of the plateau regions at higher powers. This means that the effectiveness of the ladder mechanism to sustain the plateau reduces at higher power and, therefore, the efficiency of the dissociation may not scale with the increase in the MW power. The fact that the plateau region is destroyed by VT-N processes means that the dissociation is limited by the concentration of N-atoms. Therefore, the process of dissociation through vibrational pumping mechanisms are self-limited by the atomic densities. Nevertheless, due to the increase in the electron density, the dissociation from the initial vibrational levels, and hence the overall dissociation increases with MW power, as seen in Figure 5.14(b).

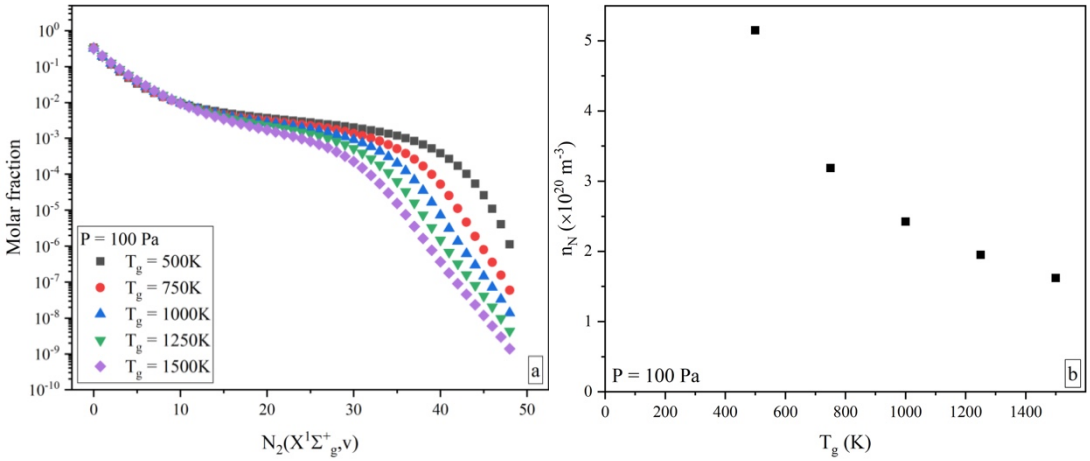

Figure 5.15: (a) VDF and (b) N-atom densities as a function of gas temperature

In order to understand the effects of gas temperature on the vibrational ladder mechanism, simulations have been performed by fixing gas temperature for the same MW power density. Figure

5.15(a) shows the VDF as a function of gas temperature. It is clearly seen that the plateau decreases with increasing gas temperatures, owing to the effectiveness of VT-N processes at high temperatures. Actually, the role of the VT-N processes is to decrease the non-equilibrium nature of VDF. This explains a decrease in the dissociation at higher temperatures, as seen in Figure 5.15(b).

As the vibrational ladder mechanism is dominant at such pressures, simply increasing the MW power does not translate to enhanced degree of dissociation. Therefore, for stationary plasma operations at such pressures, the gain in degree of dissociation with MW power is limited. Hypothetically, in order to have very high degree of dissociations at such operating conditions, a plasma process should be such that the gas temperatures are maintained low in order to ensure that the VT-N relaxation processes are inefficient and results in non-equilibrium VDF.

5.6 Conclusions

Measurements and simulations were used to characterize the plasmas operating under stationary conditions. The dissociation yields of nitrogen are seen to be less than that of hydrogen by a factor of two for both the sources. Simulations of the conditions indicate that the electron impact processes are dominant in these conditions, *i.e.* $e + N_2(X^1\Sigma^+_g,v) \rightarrow e + N\ (^4S^o) + N(^2D^o)$. It is also observed that the vibration ladder mechanism is important in these conditions. The vibrational relaxation processes effectively populate the upper vibrational levels and dissociation from these levels contributes to around 25% of the total dissociation. It is also seen that the dissociation of nitrogen molecules by vibrational ladder mechanism is self-limited by the N-atom density, where the Treanor plateau is suppressed by the effective VT-N relaxation processes. Therefore, for these pressure conditions, the strategy of increasing the degree of dissociation by increasing the MW power is not very effective. Therefore, in chapter 6 the effectiveness of plasma pulsation on degree of dissociation is studied.

Chapter 6 – Pulsed MW plasmas

6.1 Introduction

The chapter will consider the characterization of the plasma sources working under pulsed operation. The chapter will first discuss the fast-transient processes that are observed at the instant following the switching on or off of the plasma. Aspects of this have already been discussed in Chapter 3 while discussing the S/N and uncertainties of N-atom densities measurement for pulsed plasmas. It was observed that the N-atom densities showed surge when the plasma was switched off while the densities crashed when the plasma was switched on. These observations will be studied, both experimentally and through simulations to understand the phenomena underlying the processes.

These will be followed by estimating the efficiency of pulsed plasma for dissociation of nitrogen. The enhancement of N-atom densities for pulsed plasma when compared to continuous plasmas under same time averaged MW absorbed power has been estimated from the experiments. These results are further supported by the simulations to better understand the parameters influencing the enhancement factor.

6.2 Experimental conditions

Operating the MW plasma in pulsed plasma conditions was found to be more complicated than that in stationary conditions as the plasmas were often unstable owing to high reflected power. As a consequence, the MW frequency was chosen between 2.44 GHz and 2.46 GHz such that the reflected power attained is at minimum and the absorbed MW power is at maximum. This situation usually brought to the coupling of 90% of the incident power displayed on the MW power supply. The MW power profiles for most conditions were nearly square wave with the rise and decay time of the absorbed MW of the order of μs. As explained in chapter 2, two different methods were used to pulse the plasma, namely I) duty cycle varying between 0.1 to 0.9 at a fixed frequency of 10 Hz and II) duty cycle of 0.5 at frequencies between 10 Hz to 100 Hz. The input power during the high power phases for these experiments was fixed at 200 W which is also the maximum of the MW generator used in this work. Further, it was impossible to pulse the plasma when the MW power during the low-power phase is fixed at zero, possibly due to very large cycle time (for 10 Hz cycle time was equal to 100 ms) for the discharge to be sustainable during the plasma-off phase.

Therefore, the absorbed MW power during the low-power phase for all experiments was fixed at value of 20 W.

It was quite difficult to perform pulsed plasma experiments for hydrogen plasmas with Hi-wave source as the pressure fluctuations (as it was not possible to control the hydrogen gas flow rate efficiently) in the reactor often rendered the plasma unstable and could not sustain long operation times. Thus, the pulsed plasmas experiments with Hi-wave source were restricted to nitrogen plasmas. The experimental conditions studied were 20-175 Pa and 20-180 W of coupled MW power.

6.3 Decay and rise of N-density and FPS emission

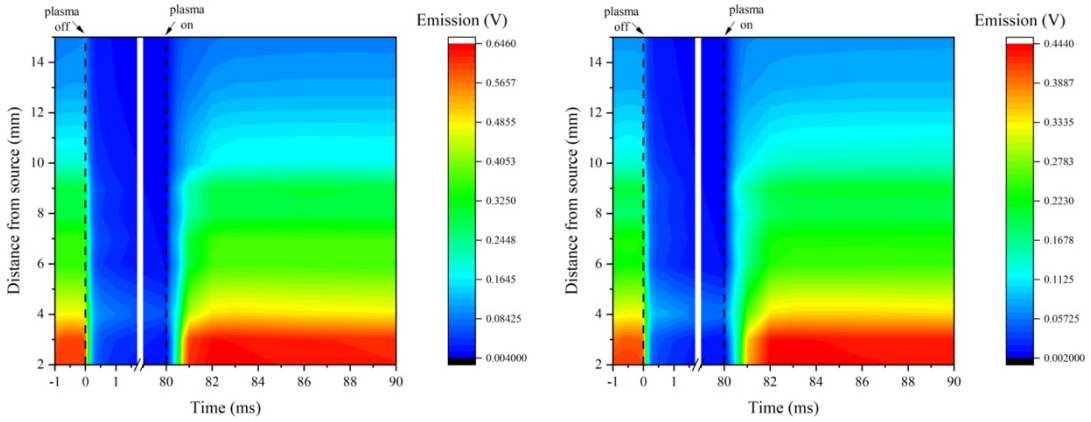

Figure 6.1: Spatio-temporal variation of FPS emission from Nitrogen plasma produced by Hi-wave source at (left) 100 Pa and (right) 150 Pa for 20% duty cycle and 10 Hz plasma pulsation frequency. Time t=0 refers to the instant plasma is switched off, while t=80 ms refers to the instant the plasma is switched on. The source is positioned at y = 0.

Figure 6.1 shows the spatio-temporal variation of FPS emission from nitrogen plasmas produced by Hi-wave plasma source at (left) 100 Pa and (right) 150 Pa pressure with time = 0 refers to the instant plasma is switched off. During the decay phase of the plasma, the FPS emission depletes uniformly along the length of the plasma within the first 1 ms of the transition. On the other hand, when the plasma is switched on, the FPS emissions seem to increase much faster closer to the surface of the source and a stationary condition is achieved for all the spatial positions within 2 ms of the transition. Thus, for all practical reasons, the analysis of the pulsed plasma can be composed into two regimes, the fast-transient regime and the stationary regime. As seen earlier for stationary plasma, the FPS emission is reflective of the electron densities. Therefore, the plasma can be considered to be constant volume for most periods except for the small period of about 2 ms corresponding to the transition between the low power to high power phase.

On the other hand, no clear conclusion about the spatial variation of the N-atom density could be deciphered due to the scatter of data along the spatial direction. Figure 6.2 shows the variation of time-averaged N-atom density at 100 and 150 Pa where unlike the stationary plasmas N-atom density is no more spatially homogeneous for the pulsed plasma. The time averaged N-atom density seems to attain maximum around x= 10 mm from the plasma surface. Studying spatio-temporal variation of the plasmas would be challenging with the current optical-detector system as it would require numerous acquisitions to obtain satisfactory trends. For this reason, further studies were focussed on studying the temporal variation of N-atom and FPS emission for a fixed spatial location i.e. 10 mm and 14 mm for from the surface of the Hi-wave and Aura-wave respectively. A planar LIF could be tried to give more insight about spatial variations of N-atom densities.

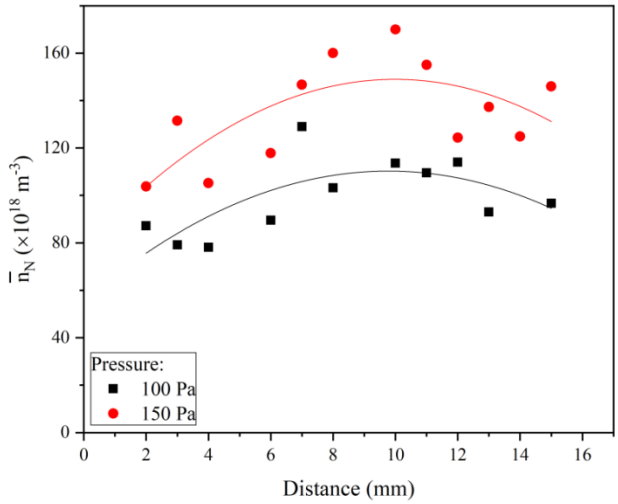

Figure 6.2: Time-average N-atom density for Nitrogen plasma produced by Hi-wave plasma source for 0.2 duty cycle at 100 Pa and 150 Pa.

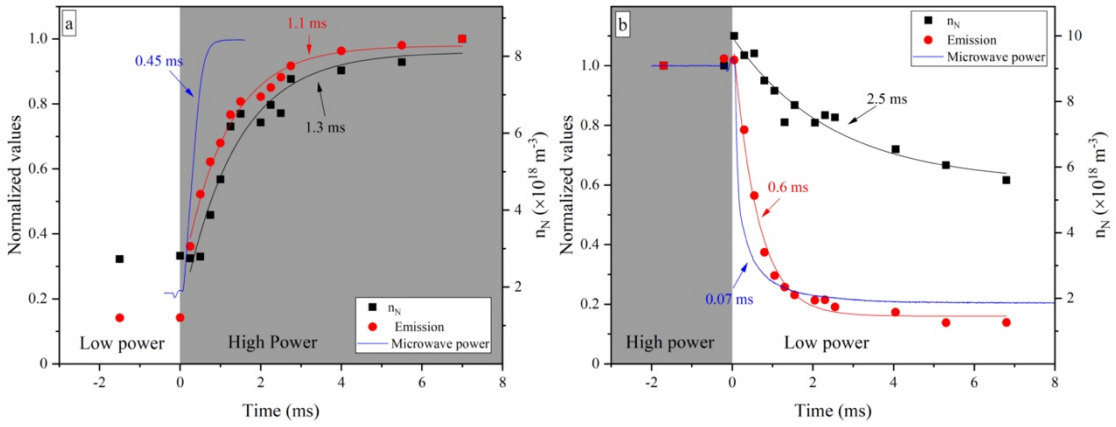

Figure 6.3: Temporal evolution of the N($^4S^o$)-atom density, the $N_2(B^3\Pi_g)$ emission intensity and the MW power for (a) the high-power phase and (b) the low-power phase at pressure of 20 Pa and 0.5 duty cycle for the Aura-Wave source. The time origin, t = 0, i.e. when transitioning between the high- and low-power phases, is chosen at the start of the power increase (a) or decrease (b). Time-resolution of these measurements is 250 µs.

The time-evolution of the N-atom density, the 728-750 nm FPS emission intensity, and the MW power with Aura-wave source are shown in Figure 6.3. In this figure, the time origin, t = 0 s, is chosen at the start of the power increase (a) or decrease (b) at the transition between the high- and low-power phases. Also shown in the figure are the time-variation fits using first order exponential growth and decay functions that are used to estimate the rise and decay characteristic times. The rise and decay times of the absorbed MW power are approximately 0.45 ms and 0.07 ms, respectively. These are much smaller than the rise and decay times of the $N_2(B^3\Pi_g)$ emission intensity and the $N(^4S^o)$-atom density. Also, the measured plasma characteristics reach steady-state values during both high- and low-power phases. This indicates that the characteristic times for the governing processes of $N(^4S^o)$-atom and $N_2(B^3\Pi_g)$ kinetics are much smaller than the 100 ms pulse period. The characteristic time of N-atom density decay is seen to be between 10 and 20 times greater than that of the plasma emission.

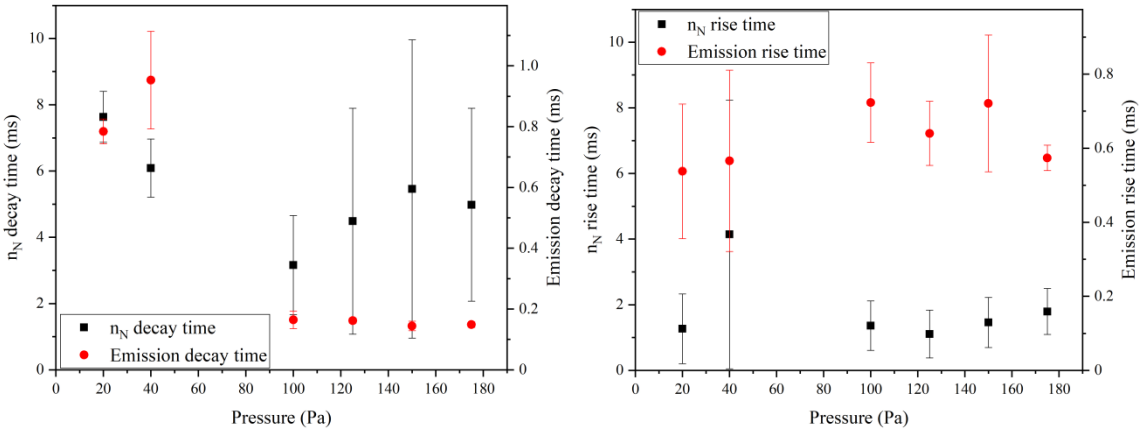

Figure 6.4: Decay (left) and rise (right) times of N-atom densities and FPS emissions

The transient characteristics of N-atom density and FPS emissions with Hi-wave sources have similar trends. The decay (left) and rise (right) times for N-atom density and FPS emissions are shown in Figure 6.4. The values of rise times for N-atom density and FPS emissions are seen to be independent of pressure and are around 2 ms and 0.7 ms respectively. The dynamics of the electron heating in pulsed plasmas is very fast and the electron temperature usually closely follows the time-scale of the absorbed MW power [96]. Further discussion on this is provided in section 6.4.

The sudden increase in the MW power should result in a large electron heating that leads to enhanced excitation, ionization and dissociation kinetics. The rise times of N atom density and FPS emission would therefore represent the ionisation, dissociation and excitation characteristic times. Since the gas temperatures is fairly low, *i.e.* T_g=500-600 K, the excitation is governed by electron impact processes (R6.1) while the dissociation involves both an electron impact process on the ground state (R6.2) which also requires vibrational excitation by electron impact. Thus, the time

variation of the $N(^4S^o)$-atom density and the $N_2(B^3\Pi_g)$ emission intensity are also indicative of electron density build-up and ionization time-scale.

$$e + N_2(X^1\Sigma_g^+) \rightarrow e + N_2(B^3\Pi_g, v) \quad \text{(R6.1)}$$

$$e + N_2(X^1\Sigma_g^+, v) \rightarrow e + N_2(X^1\Sigma_g^+, w>v) \rightarrow e + N(^4S^o) + N(^4S^o \text{ or } ^2D^o) \quad \text{(R6.2)}$$

As for the decay phase, since the dynamics of the electron heating is very fast, one would expect the electron temperature drop to closely follow the MW power variation. Therefore, the high energy threshold electron impact excitation, ionization and dissociation processes are very likely to be rapidly quenched during the power decay phase. These will be discussed in detail later in the chapter, where results from simulations are also analysed. If the loss process of $N_2(B^3\Pi_g)$ was mainly through radiative de-excitation, which has a characteristic lifetime of 10 μs [181], the decay of the $N_2(B^3\Pi_g)$ emission would have closely followed the MW power decay. This is obviously not the case in this experiment which showed a much longer characteristic decay time of ~600 μs for the FPS emission. Actually, $N_2(B^3\Pi_g)$ kinetics probably follows a complex mechanism similar to that observed in a short-lived afterglow [54,173,174]. In that case, the kinetics of $N_2(A^3\Sigma^+_u)$, $N_2(B^3\Pi_g)$ and $N_2(C^3\Pi_u)$ are strongly coupled in a collisional-radiative loop involving several processes that are reported in [182]. Generally, the surface processes of the nitrogen meta-stables are negligible. Even if we assume a significant de-excitation probability of $N_2(A^3\Sigma^+_u)$ at the wall, the diffusion/wall-de-excitation of this metastable should be diffusion limited. In this case, the $N_2(A^3\Sigma^+_u)$ de-excitation characteristic time, would correspond to the diffusion characteristic time of $N_2(A^3\Sigma^+_u)$ that is given by Λ^2/D where Λ is the plasma characteristic length and D the diffusion coefficient. Assuming the same value for the diffusion coefficients of all N_2 electronic states and a Lenard-Jones N_2-N_2 interaction potential, a value of 0.03 m^2/s was estimated for D [96] at a pressure of 20 Pa and a temperature of 600 K. This yields a 5 ms diffusion characteristic time for the 2 cm length scale estimated from the volume-to-surface ratio in our system. This diffusion time-scale is much longer than the observed decay time and we can conclude that the surface process cannot dictate the loss mechanism of electronic excited states of N_2. The major exit channels from this loop are through pooling reactions as below [104,107,165]:

$$N_2(A^3\Sigma^+_u) + N_2(a'^1\Sigma^-_u) \rightarrow N_4^+ + e \quad k=10^{-11}\ cm^3\cdot s^{-1} \quad \text{(R6.3)}$$

$$2N_2(A^3\Sigma^+_u) \rightarrow N_2(X^1\Sigma_g^+, v=0) + N_2(B^3\Pi_g \text{ or } C^3\Pi_u) \quad k=7.7\times10^{-11}\ cm^3\cdot s^{-1} \quad \text{(R6.4)}$$

$$N_2(A^3\Sigma^+_u) + N(^4S^o) \rightarrow N_2(X^1\Sigma_g^+, v=6\text{-}9) + N(^2P^o) \quad k_4=4\times10^{-11}\ cm^3\cdot s^{-1} \quad \text{(R6.5)}$$

$$N_2(B^3\Pi_g) + N_2(X^1\Sigma_g^+) \rightarrow N_2(X^1\Sigma_g^+, v=0) + N_2(X^1\Sigma_g^+) \quad k_3=1.5\times10^{-12}\ cm^3\cdot s^{-1} \quad \text{(R6.6)}$$

The estimation of the characteristic times of reactions (R6.3) and (R6.4) is more difficult since it requires the knowledge of the $N_2(A^3\Sigma^+_u)$ and $N_2(a'^1\Sigma^-_u)$ densities. A lower limit for these time scales may be however calculated by noticing that the relative densities of these excited states with respect to N_2 ground states are always below 10^{-3} [165,182]. Using this value of relative density and the respective rate constants, we can estimate lower limits of 42 ms and 5 ms for the characteristic times of reaction (R6.3) and (R6.4), respectively. These values are also much larger than the observed sub-millisecond decrease of the FPS emission intensity. These processes do not result in a depletion of the excited triplet state that is consistent with the one observed for the FPS emission during the early stage of the low power phase. Using the N-atom density measured in the present study, i.e., $n_N \approx 10^{19}$ m^{-3}, a characteristic time of 2.5 ms was estimated for reaction (R6.5) that is also not fast enough to explain the time decrease of the FPS just after the transition to the low power phase. Eventually, a value of 275 μs was estimated for reaction (R6.6). It appears therefore that in our condition, reaction (R6.6) is the major loss mechanism of excited electronic states in our discharge conditions. The characteristic time inferred from this reaction rate constant is not very far from the one seen experimentally, i.e., ~600 μs. Taking into account the qualitative nature of our reaction timescale analysis as well as the uncertainty of the rate constants value of (R6.6) [182] one can even consider that the agreement is satisfactory. This will be later verified from kinetic calculations.

The characteristic time of N-atom density decay is longer than that of the plasma emission. It varies between 8 ms at 20 Pa to about 4 ms for pressures > 100 Pa. Over such a long-time scale, it can be usually assumed that the consumption of N-atom takes place through surface recombination processes at the reactor walls.

Assuming a Lennard-Jones N-N_2 interaction potential, a value of 0.15 $m^2 \cdot s^{-1}$ [96] was estimated for the diffusion coefficient of N-atom at 20 Pa and 600 K. This yields a value of 3.4 ms for the diffusion characteristic time, which is very close to the decay time seen in our experiments. This shows that the measured depletion kinetics of $N(^4S^o)$ atoms agrees with diffusion limited recombination process. Therefore, we cannot determine the γ_s value of the surface recombination reaction. The only thing we can conclude is that the surface recombination time scales are either of the same order of magnitude or shorter than the diffusion time scales. In both cases, the measured characteristic time would be consistent with the diffusion limited recombination. Of course the surface recombination time scales may show similar time scales as diffusion.

6.4 Surge and crash of N($^4S^o$)-atom during phase transition

Actually, the N($^4S^o$) loss kinetics involves much more complex kinetics than a simple diffusion/recombination process. As a matter of fact, looking at Figure 6.3(b), one can notice a surge in the N-atom density just at the transition between the high and low power phases despite the poor time resolution in this figure. This reproducible surge observed in many performed measurements is similar to the one observed in [53] where the authors showed an unexpected increase in N($^4S^o$) TALIF signal at the start of the plasma off phase in a pulsed microwave plasmas. The methodology developed in the present work provides TALIF measurements with a time resolution as low as 5 µs and a straightforward signal processing which enables investigating short time-scale kinetics effects for N($^4S^o$). This has been used to confirm and further study the existence of this fast increase in N-atom TALIF signal that is expected to occur within 500 µs during the early stage of the low power phase.

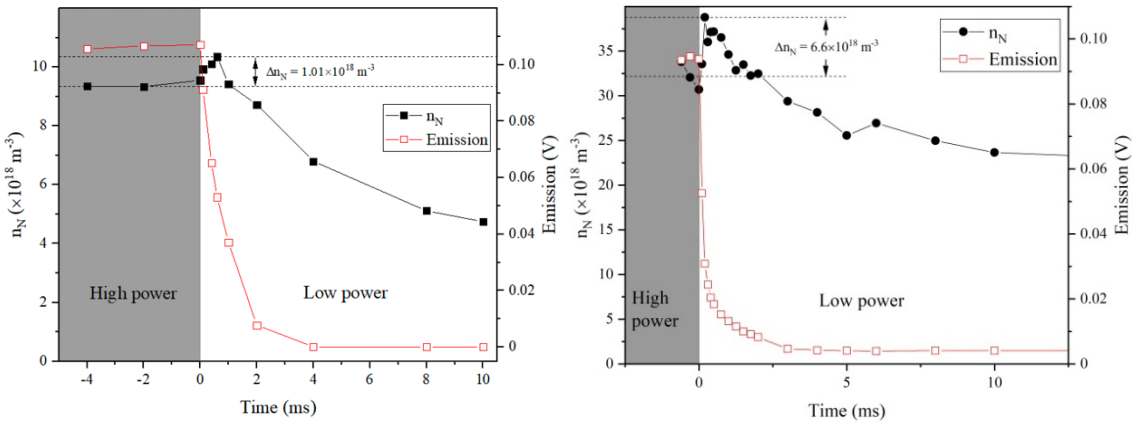

Figure 6.5: Time-resolved measurement of N-atom density (black circles, left axis) and $N_2(B^3\Pi_g)$ emission (red squares, right axis) around the transition between the high and low power phases and during the early stage of the low power phase for Hi-Wave source at (left) 40 Pa, 0.5 duty cycle, pulsation frequency 50 Hz and (right) at 100 Pa, 0.2 duty cycle, pulsation frequency 10 Hz

Figure 6.5 shows time-resolved measurements with a much better resolution, *i.e.* 10 µs resolution, of the N($^4S^o$)-atom density and the background plasma emission near the transition between the high- and low-power phases for (left) Aura-wave source at 20 Pa and (right) Hi-wave source at 100 Pa. This figure confirms the existence of a significant increase in the N-atom density (more than 10^{18} m^{-3}, which represents more than 10% relative variation) just after the transition to the low power phase. Actually, a high N($^4S^o$) density level is maintained during almost 1 ms after the power transition. Note that such behaviour is not observed for the plasma emission intensity that decreases sharply just after the transition.

On the contrary, the opposite trend is observed for N-atom density during the transition between low-power phase and high-power phase. Figure 6.6 shows the time-resolved measurements of the N($^4S^o$)-atom density and the background plasma emission near the transition between the high- and low-power phases for Hi-wave source at 100 Pa. While the FPS emission shows a monotonic increase with time after the transition to high power phase, the N-atom density shows a small dip lasting for about 1 ms before rising monotonically after the transition to high power phase.

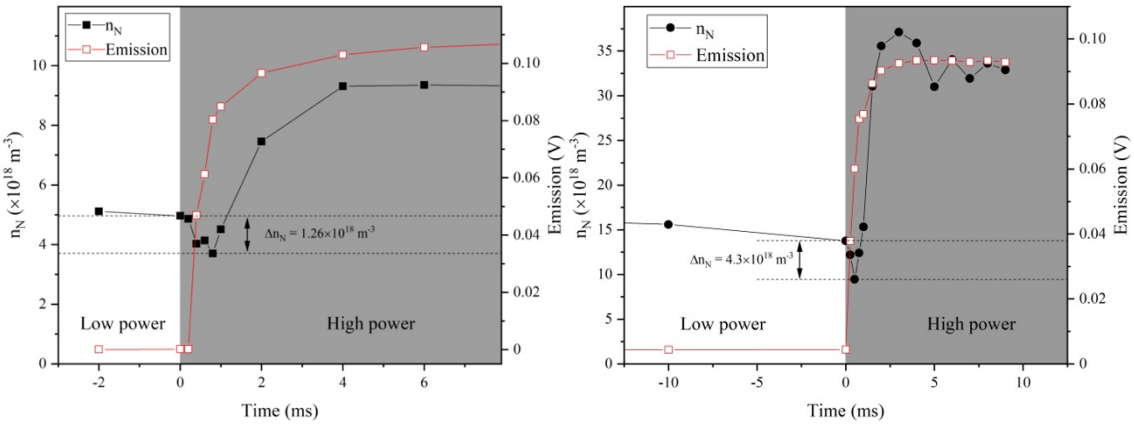

Figure 6.6: Time-resolved measurement of N-atom (black circles, left axis) and $N_2(B^3\Pi_g)$ emission (red squares, right axis) around the transition between the low and high power phases and during the early stage of the high power phase for Hi-wave source at (left) 40 Pa, 0.5 duty cycle, pulsation frequency 50 Hz and (right) at 100 Pa, 0.2 duty cycle, pulsation frequency 10 Hz.

The phenomena of the increase and the decrease in the N-atom density during the transition is referred to as "*surge*" and "*crash*" respectively in this thesis. Figure 6.7 shows (left) the absolute densities of surge and crash and (right) ratio of surge and crash to the N-atom density just before the phase transition observed for Hi-wave plasma source as a function of pressure. The surge and crash densities are substantially high and are seen to increase with pressure. However, the ratio of surge and crash are seen to decrease with pressure, attaining about 0.8 at 20 Pa and reducing to 0.1 at higher pressures. All the experiments were repeatable and the magnitudes of the surge and crash are greater than the uncertainty of the N-atom densities.

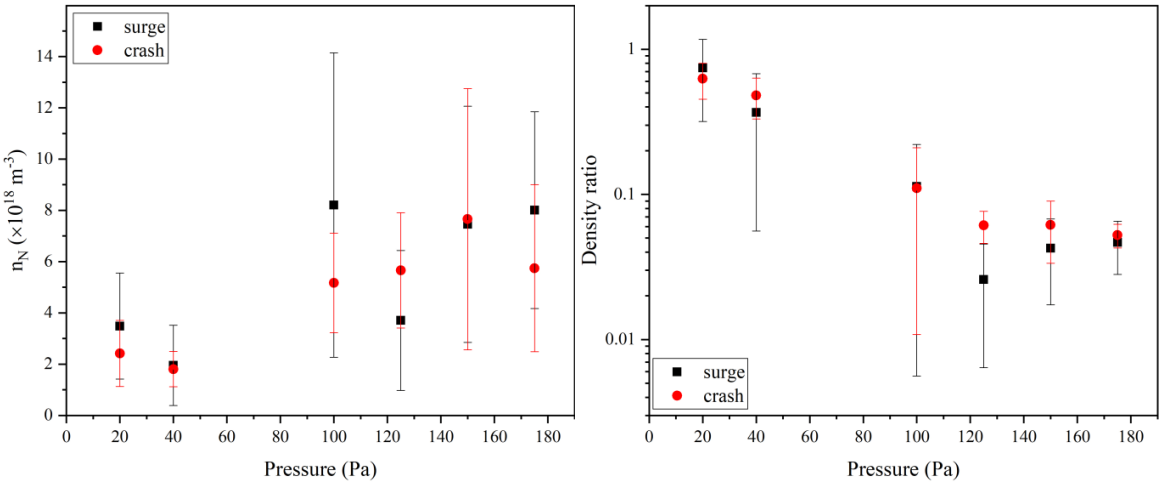

Figure 6.7: (left) Absolute surge and crash densities and (right) ratio of surge and crash densities to the N-atom density just before the phase transition observed for Hi-wave plasma source as a function of pressure.

To understand the evolution of the N($^4S^o$)-atom density during pulsed plasma operation, the self-consistent collisional radiative model for N_2 plasma has been used. Despite the variations in the plasma volume during the transient phase of the pulsed plasma, our analysis of FPS emissions indicate that this variations are restricted mainly to the fast transient phase (2 ms after the power phase transition). Therefore, we make a convenient assumption, just like that of chapter 5, that the plasma volume remains constant during the pulsation. The simulations have been performed at 40 Pa. Unfortunately, simulations with the experimentally injected MW power injected (180 W at high phase) resulted in peak temperatures greater than 2000 K. Therefore, to have reasonable values of gas temperature and atomic densities as observed in the experiments, the time-averaged input MW power was fixed at 5 W. Moreover, these simulations should qualitatively highlight the different important processes causing the phenomenon of surge and crash. Firstly the effect of the surface recombination coefficient of N($^4S^o$) γ on the wall on the surge and crash process are studied.

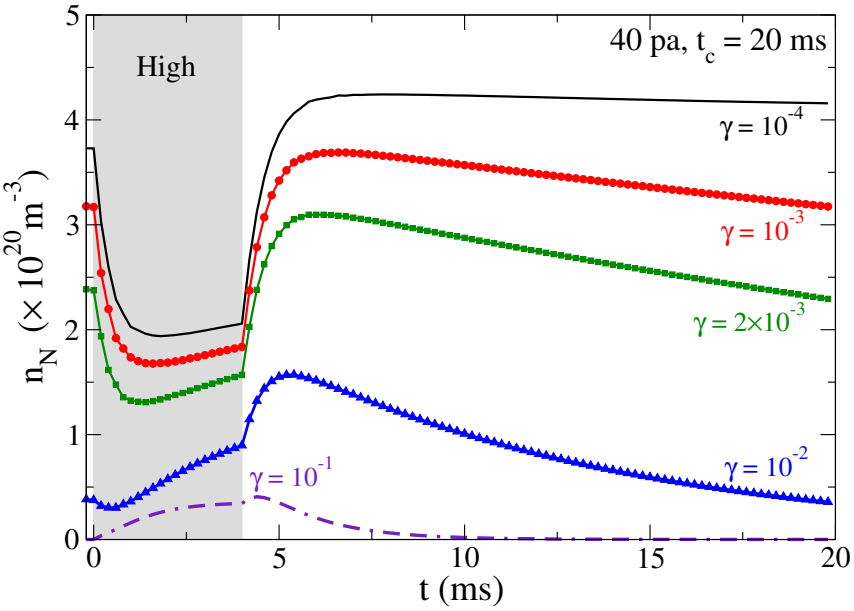

Figure 6.8: temporal variation of N-atom density at different γ in a pulsed plasma with duty cycle of 0.2

Figure 6.8 shows the temporal variation of nitrogen atom density as a function of the surface recombination γ, for pulsed plasma with duty cycle of 0.2. The degree of surge and crash seems to decrease with increase in surface recombination coefficient γ. While the N-atom decay is dominated by processes over a long time scale such as surface recombination of $N(^4S^o)$ at the walls of the reactor, the phenomenon of surge and crash in the $N(^4S^o)$ density can be only due to the change in the kinetics of very short characteristic-time processes. This may involve either a decrease/increase in the rates of N-atom consumption processes or an increase/decrease in the rates of N-atom production processes at the transition between the power phases. The rapid transition from the high (low) - to the low (high) power phases will first result in a decrease (increase) in the electron temperature, which immediately affects the rates of the electron-impact processes, and more particularly the ionization and dissociation processes directly causing the surge and crash in a pulsed N-plasma. From chapter 5, the different processes that are expected to dictate the kinetics of $N(^4S^o)$ in addition to electron impact dissociation (R6.2) and surface recombination are listed below.

$$N(^2D^o) + N_2 \rightarrow N(^4S^o) + N_2 \quad \text{(R6.7)}$$

$$N(^2D^o \text{ or } ^2P^o) + \text{wall} \rightarrow N(^4S^o) \quad \text{(R6.8)}$$

$$e + N_2^+ \rightarrow N + N \quad \text{(R6.9)}$$

$$e + N(^2D^o \text{ or } ^2P^o) \rightarrow e + N(^4S^o) \quad \text{(R6.10)}$$

$$e + N(^4S^o) \rightarrow e + N(^2D^o \text{ or } ^2P^o) \quad \text{(R6.11)}$$

Then, the time-evolution of N($^4S^o$) is governed by the interplay of all the process mentioned above. All the results that are discussed below in this section are performed at a pressure of 40 Pa with duty cycle of 0.2 and pulse cycle time of 20 ms, which corresponds to 4 ms of time in which the plasma in on. The surface recombination coefficient γ for N($^4S^o$) has been fixed at 10^{-3}. This value was chosen to have very pronounced surges and crashes.

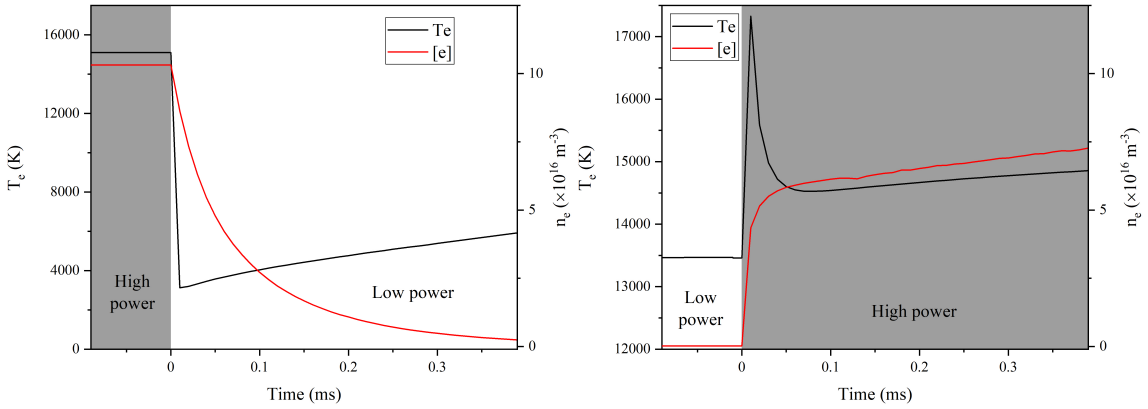

Figure 6.9: Time-variation of the electron temperature and electron density at the transition between (left) the high- and low-power phases and (right) low power to high power phase for pulsed plasma operating at 0.2 duty cycle, a pulse period of 20 ms at a pressure of 40 Pa. The time t=0 refers to the phase transition of power in both the figures

Figure 6.9 shows the time-variation of the calculated electron-temperature (T_e) and electron density (n_e) at the transition between (left) the high- and low-power phases and (right) low power to high power phase. We can see and confirm the previously mentioned and expected very fast and strong electron cooling/heating phase during the power transitions. It appears that the calculated n_e and T_e are coupled during the phase transition of the power. They are governed by the electron kinetics and more precisely by the balance between the ionization and electron loss processes. Over larger time scales, they are dominated by wall recombination. During the high to low power transition, the electron temperature decreases from 15000 K to 4000 K. This first decrease in T_e is due to the fact that the very large inelastic collision frequency results in electron-heavy species energy transfer kinetics that is much faster than electron recombination kinetics. As a result, when the power is decreased, a similar electron population has to share a much smaller amount of energy. This results in the observed decrease in the electron temperature. Due to the very low T_e-value at the end of the very short cooling phase, the electrons start recombining and their population decreases gradually as may be seen in Figure 6.9(left). This results in the observed subsequent increase in the electron temperature that reaches a steady state low power phase value of 12500 K, which is just 2000 K below the high power phase value. Similarly, during the low power to high power transition, the T_e increases instantaneously to a value of 17000 K. Subsequently, as the ionization kinetics results in the increase in electron density, the T_e decreases gradually to reach the

steady state high power phase value of 15000 K as seen in Figure 6.9(right). Thus all the electron impact processes is expected to experience rapid changes during the transition.

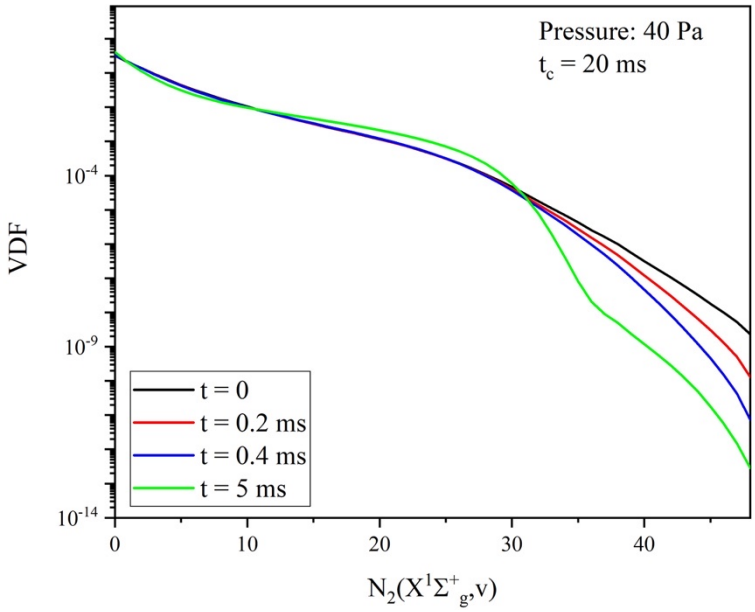

Figure 6.10: Time-variation of the vibrational distribution functions (VDF) during the transition to the low power phase. The simulation was performed for a pressure of 40 Pa, time averaged MW power 5 W, a pulse period of 20 ms and a duty cycle of 0.2. The emphasis is put on the high/low power transition

Figure 6.10 shows the calculated time-variation of the vibrational distribution functions (VDF) at different stages of the transient between high- and low-power phases. The relative density of high-lying vibrational states (v>34) strongly decreases within 200 µs after the transition to the low-power phase. A detailed rate analysis shows that this decrease benefits to the low-lying vibrational states through vibrational-de-excitation process, the contribution towards vibrational dissociation during the initial stages is negligible. Moreover, the total variation of relative density of the high vibrational levels is below 10^{-5} which is much below the observed $N(^4S^o)$ relative density increase.

The time-variation of the rates of the processes involved in the kinetics of $N(^4S^o)$ during the transition from high to low power phase are shown in Figure 6.11. Actually, during the high power phase, the kinetics of $N(^4S^o)$ is essentially governed by the balance between (I) the production through electron-impact dissociation of N_2 (reaction (R6.2)) and the de-excitation of $N(^2D^o/^2P^o)$ at the wall (reaction (R6.8)) and, to a lesser extent, by super-elastic collisions (reaction (R6.10)), and (II) the loss through electron-impact excitation of $N(^4S^o)$ to $N(^2D^o)$ and $N(^2P^o)$ states (reaction (R6.11)) and surface wall-recombination.

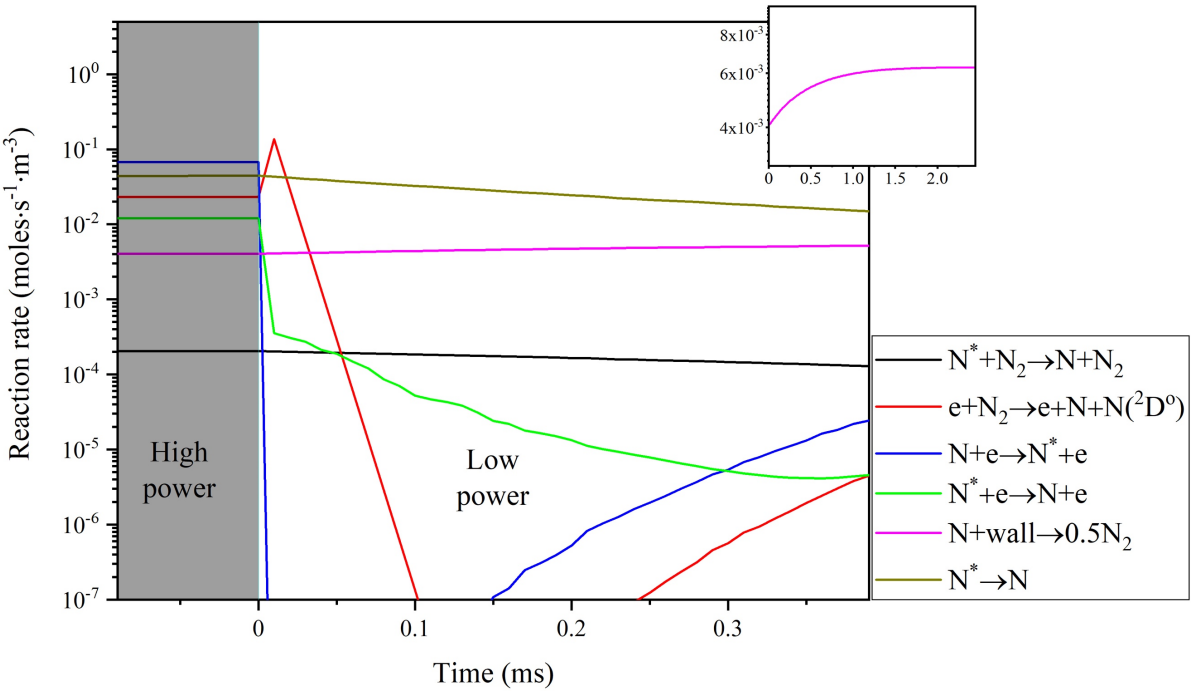

Figure 6.11: Time-variation of the main electron impact processes involved in the kinetics of N($^4S^o$)-atom at the transition between the high- and low-power phases. The rates of surface recombination processes are also shown for comparison. Also shown in the insert is the increase of surface recombination of N($^4S^o$) in the low power phase. N indicates both considered N-atom metastable states, i.e. N($^2D^o$) and ($^2P^o$). The axis labels of the insert are the same as those of the main plot.*

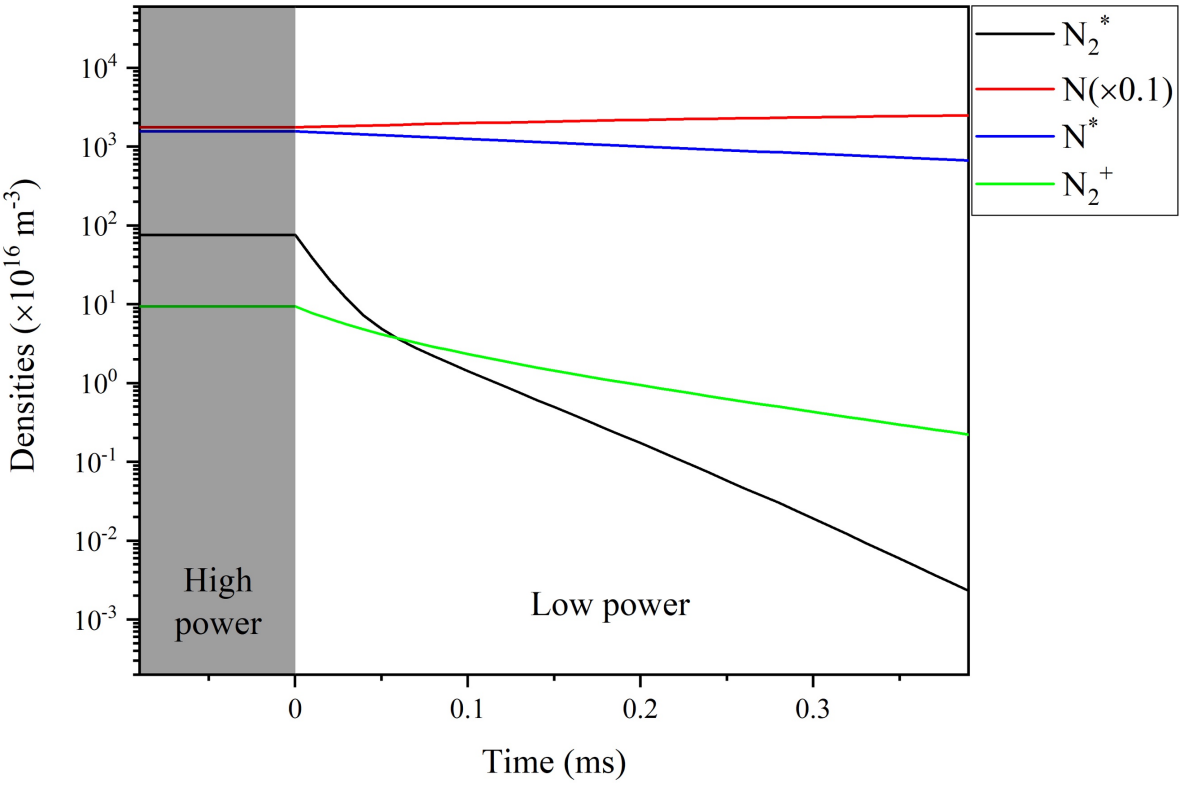

Figure 6.12: The time evolution of different species during the transition between high and low power phase. N_2 and N* indicate $N_2(A^3\Sigma^+_u)$ and $N_2(B^3\Pi_g)$ levels of molecular nitrogen and both considered N-atom metastable states, i.e. N($^2D^o$) and ($^2P^o$).*

When the power is decreased, the electron cooling affects this balance through a strong decrease in the electron-impact dissociation of N_2, the $N(^4S^o)$-atom excitation and, to a lesser extent, the $N(^2D^o/^2P^o)$ de-excitation. As a result, the kinetics of $N(^4S^o)$-atom becomes dominated by the wall de-excitation of $N(^2D^o/^2P^o)$, as a source, and wall recombination, as a loss term, during the transient. This results in a net production of $N(^4S^o)$ during the initial states of the transition, which explains the observed short time scale increase in $N(^4S^o)$ density in both the experiment and simulation. Actually, the surface recombination rate of $N(^4S^o)$ is seen to increase slightly (about 10%) during the early low power phase (which can be easily seen in the insert in Figure 6.11). This indicates a slight increase in the $N(^4S^o)$ density over the short time-scale considered in Figure 6.12, which is in agreement with the experimental observation of surge. The major species that is produced during the transition process is the $N(^2D^o/^2P^o)$ metastables as seen in Figure 6.12.

Similar observations can be made for the transition between low to high power phase. The time-variation of the rates of the processes involved in the kinetics of $N(^4S^o)$ along with the time evolution of different species densities during the transition from low to high power phase are shown in Figure 6.13. Like the surge process, the crash process also occurs due to the imbalance in the production, *i.e.* electron impact dissociation and surface de-excitation of $N(^2D^o/^2P^o)$, and loss terms of $N(^4S^o)$ *i.e.* electron impact excitation during very short scales. The loss processes are electron driven which quickly depletes the $N(^4S^o)$ atom densities causing crash. This can be confirmed by the decrease in surface recombination rates of $N(^4S^o)$ atom as shown in the inset of Figure 6.13(up) during the initial stages of the high-power phase. Eventually, the surface de-excitation of $N(^2D^o/^2P^o)$ becomes important at larger time scales and one sees an increase in the $N(^4S^o)$ atom densities. In fact, the time evolution of the $N(^4S^o)$ and the metastables $N(^2D^o/^2P^o)$ have exactly complementary trends during the crash and surge processes.

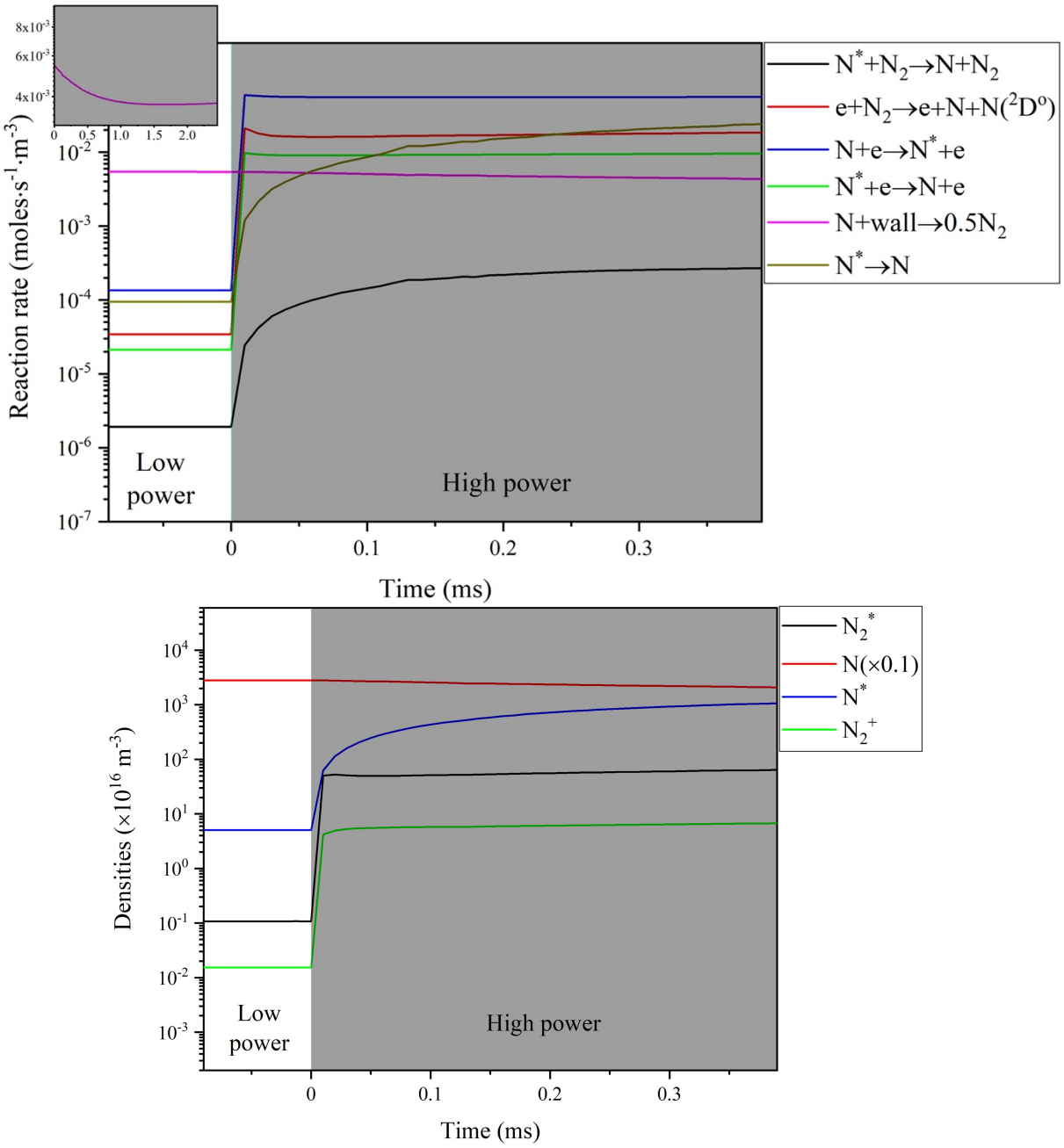

Figure 6.13: (up) Time-variation of the different processes involved in the kinetics of N(^{4}S^o)-atom and (down) the time evolution of different species densities at the transition between the low- and high-power phases. Also shown in the insert is the increase of surface recombination of N(^{4}S^o) in the low power phase. N_2 and N* indicate $N_2(A^3\Sigma^+_u)$ and $N_2(B^3\Pi_g)$ levels of molecular nitrogen and both considered N-atom metastable states, i.e. N(^{2}D^o) and (^{2}P^o).*

This finding leads to a slightly different interpretation from the one given in reference [53] where the observed increase in N(^{4}S^o)-atom density during the early post-discharge phase of a pulsed plasma was attributed to super-elastic collisions on N(^{2}D^o/^{2}P^o). Here, in addition to the various electron impact processes, we see that the wall-de-excitation of the metastable state N(^{2}D^o/^{2}P^o) atoms is very important. The relative importance of different processes can vary depending on the discharge conditions as clearly seen in experimental conditions of this study. In

any case, the contribution of N($^2D^o$) ad N($^2P^o$) metastable states to N($^4S^o$) kinetics is important for N-atom density.

6.5 Effect of duty-cycle and cycle time

The effect of pulsation has been evaluated using enhancement factor which is defined as

$$\eta_N = \frac{\int_0^{t_c} n_N(t)dt}{n_{N,Stat}}$$

where $n_{N,Stat}$ refers to the N-atom density under continuous plasma operation at a MW power equal to the time integrated average values of the MW power injected for the pulsed plasma operation. The MW profile was assumed to be a perfect square profile; while the trapezoidal integration was applied to integrate the N-atom density in order to obtain time averaged N-atom density. η_N is also reflective of the energy efficiency of the plasma process, i.e. if $\eta_N > 1$ indicates the pulsed plasma improves the yield of N-atom while the time averaged power is constant.

It has to be realized that the average power of the different duty cycles are different as the maximum and minimum power are fixed for the studies. Ideally, it would be interesting to make experiments with the same injected power for all the duty cycles. In that case the MW injected power during the high power phase will be the highest for duty cycle of 0.1. Unfortunately, these experiments could not be carried out with the present experimental setup.

Figure 6.14 shows the transient variation of normalized N-atom density *i.e.* the ratio of instantaneous N-atom density $n_N(t)$ to $n_{N,Stat}$ as a function of duty cycle at fixed pulsation frequency of 10 Hz. The line y=1 corresponds to the breakeven point and in order to have enhancement in N-atom density, one should have most of the curves above this line. The effects of surge and crash also have a role to play on the enhancement factor. Due to reflections of MW power, the injected power was found to vary strongly with the experimental conditions *i.e.* pressure and duty cycle. As seen in the previous sections, the decay times of N-atom is of the order of 10 ms (<< 100ms) which would mean most of the N-atom would decay very quickly. Similarly the rise times observed were typically around 2 ms resulting in a very quick transition to a stationary phase where N-atom densities reach saturation. This means that most parts of the decay phase for duty cycle = 0.1 lies below the breakeven curve. This is obvious as the decay phase lasts for about 90 ms which is too long to gain from the higher yield of N-atom, *i.e.* density ratios > 2 during the high power phase. On the other hand, for a duty cycle of 0.2, the gain during the high power phase is around 1.5 and substantial amount of the period, the N-atom densities are above the breakeven line. Thus the gain of N-atom yield over the entire period for duty cycle of 0.2 can be larger than 0.1. On the extreme, the duty cycle of 0.5 produce a modest gain during the high power phase and also

decays to values close to the breakeven line. Thus, such a duty cycle would produce modest enhancement to N-atom densities over the entire time period.

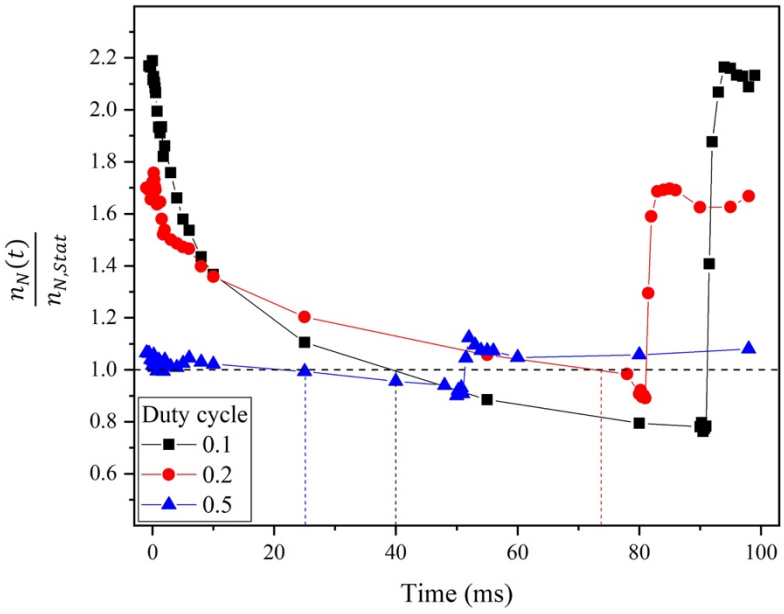

Figure 6.14: Normalized N-atom density $\frac{n_N(t)}{n_{N,Stat}}$ at 150 Pa and duty cycle of 0.1, 0.2 and 0.5.

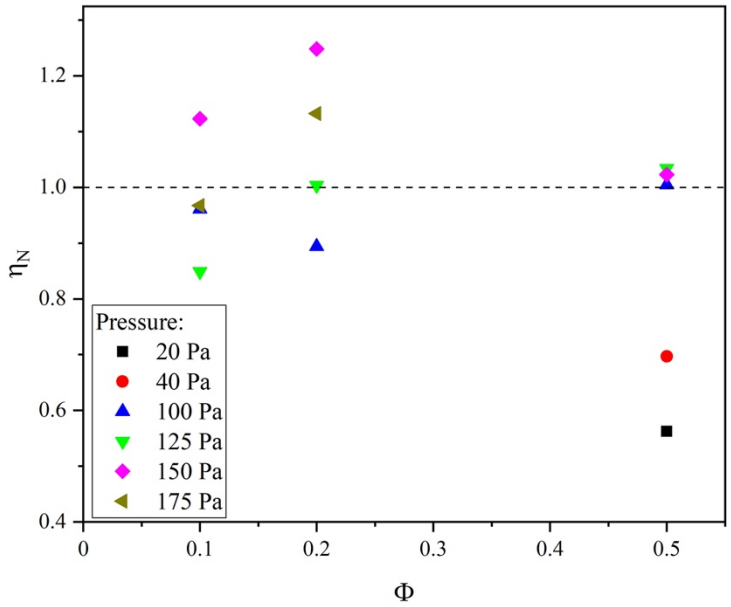

Figure 6.15: Enhancement factors as a function of duty cycle and pressure for Hi-wave plasma source pulsed at frequency of 10 Hz

Enhancement factors η_N as a function of pressure and duty cycle at fixed pulsation frequency = 10 Hz are shown in Figure 6.15. A duty-cycle of 0.2 had the maximum enhancement while the duty cycle of 0.5 were close to 1 for pressures greater than 100 Pa. Unsurprisingly, the duty cycle of 0.1 had poorer enhancement ratios for most conditions. The advantage of having smaller duty cycles is

a large amount of energy is injected in a very short duration resulting in high dissociation. However if the decay phase is too long, such high dissociation yields cannot be converted into an efficient process. Thus it would be necessary to make a judicious choice of the cycle time according the N-atom decay rates.

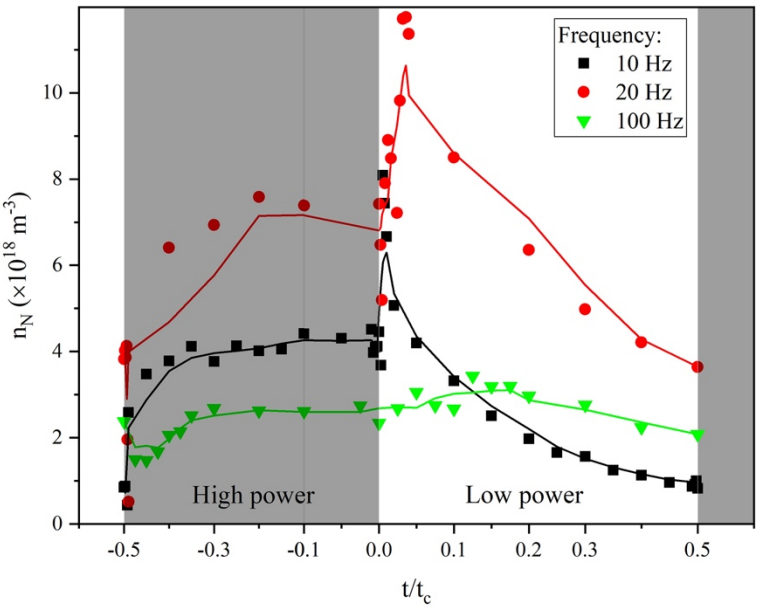

Figure 6.16: N-atom densities variation with normalized time and pulsation frequency and fixed duty cycle of 0.5 at 20 Pa.

Figure 6.16 shows the N-atom densities as a function of normalized time *i.e.* t/t_c for several plasma pulsing frequencies and fixed duty cycle of 0.5 at 20 Pa. The N-atom density yield is much greater for 20 Hz when compared to 10 Hz and 100 Hz. It is clear that 10 Hz suffers from a decay phase which is much longer than the decay times of N-atom resulting in reduced N-atom yields. On the other hand, 100 Hz with a cycle time of about 10 ms (5 ms each for high and low power phases) suffers from providing too little time for N-atom to reach saturation during the high power phase. Further, it is interesting to observe that the surge is very small for 10 Hz when compared to the large surges observed for 20 Hz. This can be further confirmed from the enhancement as a function of frequency as shown in Figure 6.17. The best frequency to operate the plasma was found to be between 25 Hz to 50 Hz. Also, the plasma pulsation seems to be very effective at the pressure of 40 Pa.

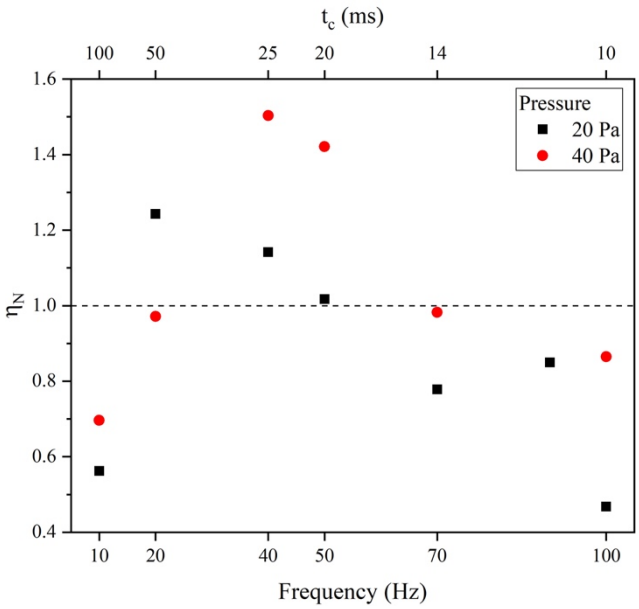

Figure 6.17: Enhancement factors η_N as a factor of frequency.

It is clear from these experimental studies that the cycle time and duty cycle have an important role to play on the enhancement ratios. If the time-averaged MW power could be maintained constant, the enhancement factor is nothing but improvement of the energy efficiency of the process. Unfortunately, our experiments did not permit us to make experiments for fixed time integrated MW power. For this reason, the CR model has been used once again to evaluate the pulsed plasma on dissociation for fixed time integrated MW power. All the simulations have been performed at 40 Pa and injected MW power of 5 W and surface recombination coefficient $\gamma = 10^{-3}$. Also, the MW power during the low power phase is 0.001 W which is just sufficient to simulate the pulsed plasma.

Figure 6.18 shows the time evolution of the plasma parameters of (a) T_g, (b) T_e, (c) n_e and (d) n_N as a function of duty cycle for a fixed cycle time. It appears that smaller duty cycle have better dissociation yields for the same MW power. This is expected as the MW energy during the high power phase increases substantially with lowering of duty cycle. This results in substantial augmentation of gas temperature, electron temperature and electron densities. In fact the electron densities show increase of one order of magnitude when compared to stationary operation. Therefore, the electron impact processes are very high resulting in enhanced dissociation.

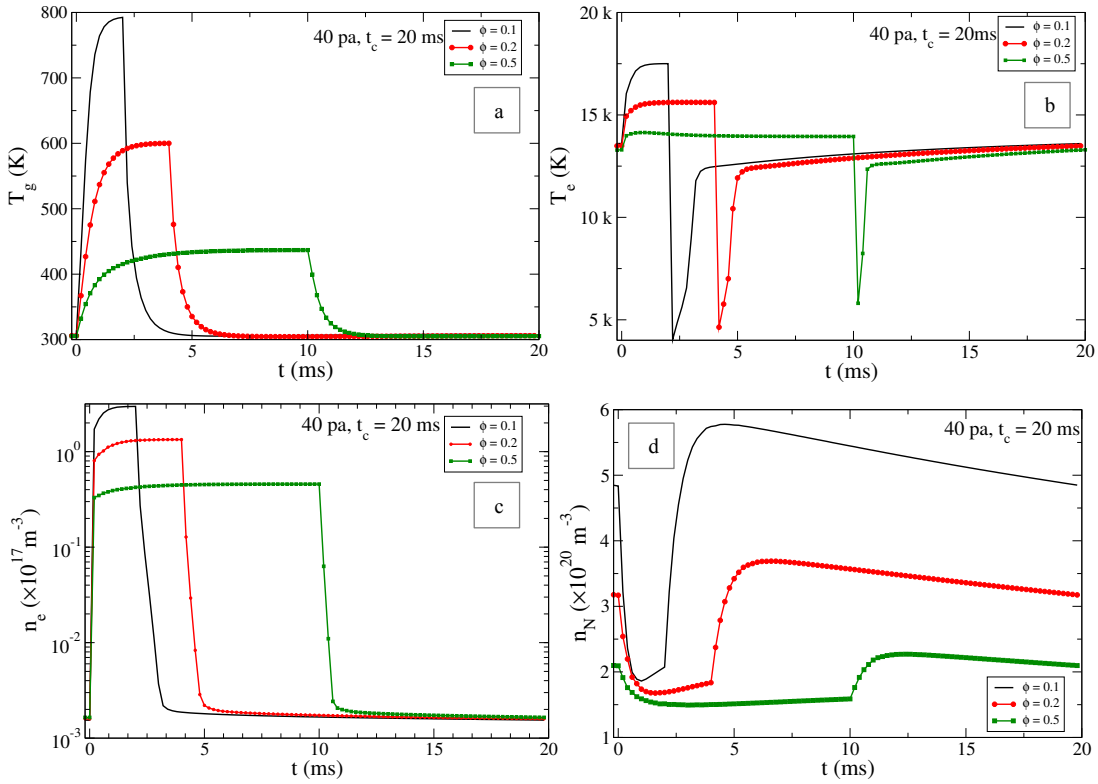

Figure 6.18: Time evolution of (a) T_g (b) T_e, (c) n_e and (d) n_N for pulsed plasma at different duty cycles and at a pressure of 40 Pa and time-averaged injected power of 5 W.

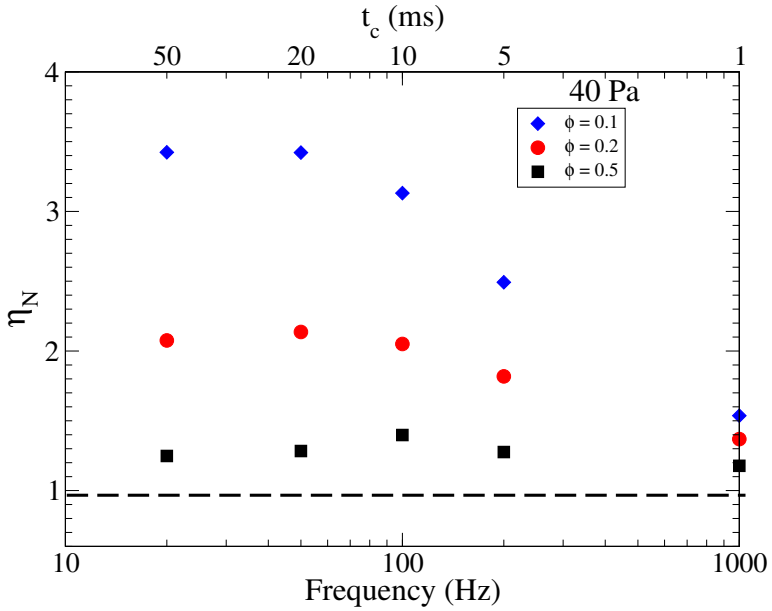

Figure 6.19: Enhancement ratios as a function of duty cycle and cycle time at 40 Pa and $\gamma=10^{-3}$

Figure 6.19 shows the enhancement ratios as a function of cycle time and duty cycle. The enhancement ratios are quite high for low duty cycles. However, like seen in the experiments, the enhancement ratios are seen to increase with cycle time. For the pulsed process to be efficient, it is necessary to ensure that there is sufficient time available for achieving stationary conditions for

electron densities. The high electron densities at stationary conditions enhance the dissociation process. For pulsation with very low cycle time, the stationary conditions for dissociation process are never achieved and therefore the advantage of pulsation is never realized.

It has to be noted that the present simulations have been performed for very low surface recombination processes, *i.e.* low γ values. In practice, the surface recombination process can be very high. Figure 6.20 shows the enhancement ratios as a function of surface recombination process and duty cycle for a fixed cycle time of 20 ms. Unsurprisingly, the increase in the surface recombination process reduces the yield of nitrogen. However, it is clear that the enhancement ratios can be substantially high for low duty cycles even for a process with large surface recombination.

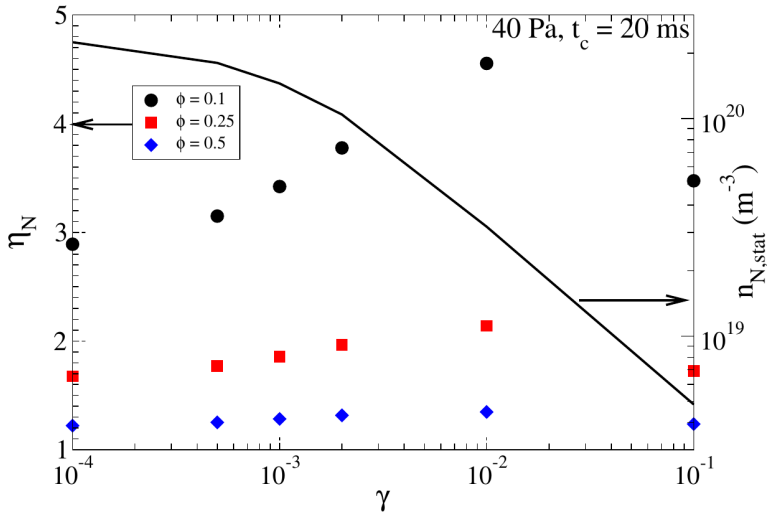

Figure 6.20: Enhancement ratios for pulsed plasmas as a function of γ and duty cycle at 40 Pa and cycle time of 20 ms

6.6 Conclusion

In this chapter, through experiments and simulation, we have studied and characterized pulsed plasmas. Especially, it has been demonstrated that the existence of an unexpected sudden increase in N($^4S^o$) atom density at the early stage of the transition from high- to low-power phase called as "surge". Similarly, during the transition from low to high power phase, there is an unexpected sudden decrease in the densities of N($^4S^o$) called as "crash". The use of a CR model taking into account a detailed state-to-state kinetics, enables to attribute this phenomenon to conversion of N($^2D^o$) and N($^2P^o$) meta-stable atoms. The surge and crash are more predominant at low pressures.

Further, the studies focused on the enhancement of N-atom densities in pulsed MW plasmas. The enhancement of N-atom densities under plasma pulsation depends on combination of several parameters such as cycle time t_c, duty cycle and pressure. It is ideal to have conditions where the

duty cycle is quite small to have very high energy dissipated resulting in effective dissociation of molecules, yet the cycle time should not be long enough to deplete substantial amount of atoms during the decay phase. Thus, an optimal combination of cycle time and duty cycle needs to be chosen such that pulsation can effectively enhance the yields of N-atom densities. Experiments and simulations indicate that the pulsation is effective for frequency between 20 Hz and 50 Hz for the studied conditions.

Chapter 7 – General conclusions and perspectives

The dissociation process of nitrogen in low pressure (10-150 Pa) MW assisted pulsed plasmas has been the main focus of the thesis, sometimes supported in terms of methodology by H-density measurements. Both experiments and detailed collisional-radiative 0D kinetic simulations have been used to study the dissociation processes. Two different Sairem® MW plasma sources, namely the magnetized Aura-Wave and the non-magnetized Hi-Wave, have been used for the studies. The N-atom density measurements have been performed using ns-TALIF. It has been shown that pulsing of plasmas can greatly increase the yield of N-atom densities.

7.1 Major contributions of the thesis

1. **ns-TALIF methodology for nitrogen plasmas:** One of the major challenges of the work was to perform TALIF under such low-pressure conditions where nitrogen plasmas have very strong emission background making it difficult to capture the fluorescence signal of N-atom. A simplified and straightforward methodology that may be used to measure $N(^4S^o)$ atom density by means of ns-TALIF technique in strongly emissive plasmas has been presented. The method makes use of the TALIF intensities measured with the laser central frequency tuned to the peak of absorption (so called PEM for Peak Excitation Method), instead of the fully integrated laser excitation spectrum (So called FEM for Full Excitation Method). The use of this method, along with a physics-based fitting/filtering procedure enables a substantial reduction of the experimental uncertainty and allows performing measurement even in strongly emissive discharges. The analysis of uncertainty and S/N were presented clearly demonstrating the limits of application of ns-TALIF for strongly emissive plasmas or weak fluorescence signals.

2. **Characterization of stationary plasmas:** Measurements and simulations were used to characterize the plasmas operating under stationary conditions. The dissociation yields of N-molecules are seen to be less than that of H-molecules for both the sources (in Hi-Wave: 0.8% vs 1.1% at 100 Pa; in Aura-Wave: 0.3% vs 0.5% at 20 Pa, as seen in Figure 5.8). Simulations of the conditions indicate that the electron impact processes are dominant in these conditions. Therefore, the dissociation of nitrogen proceeds through the electron impact dissociation *i.e.* $e + N_2(X^1\Sigma_g^+, v) \rightarrow e + N(^4S^o) + N(^2D^o)$. The VDF display a Treanor plateau owing to the vibrational ladder mechanism and it enhances the degree of dissociation for the examined conditions. However, the

dissociation of nitrogen molecules by vibrational ladder mechanism is self-limited by the N-atom density as the strong VT-N relaxation processes reduce the non-equilibrium nature of the VDF, *i.e.* the plateau. Therefore, for stationary plasmas under these pressure conditions, the efficiency of dissociation does not increase greatly with MW power.

3. **Surge and Crash in a pulsed N-plasmas:** After an adequate validation, the methodology of N-atom measurement using ns-TALIF was employed to investigate the transients of a strongly emissive pulsed microwave discharge. We especially demonstrated the existence of an unexpected sudden increase in N($^4S^o$) atom density at the early stage of the transition from high- to low-power phase called as "surge". Similarly, during the transition from low to high power phase, there is an unexpected sudden decrease in the densities of N($^4S^o$) called as "crash". The use of a CR model taking into account a detailed state-to-state kinetics, enables to attribute this phenomenon to conversion of N($^2D^o$) and N($^2P^o$) meta-stable atoms. Thus, the measurement of surge is indicative of the population densities of N($^2D^o$) and N($^2P^o$). The surge and crash are more predominant at 40 Pa than at 100 Pa or 150 Pa.

4. **Enhancement of N-atom densities under low pressure conditions:** Finally, the studies focused on the enhancement of N-atom densities in pulsed MW plasmas. The enhancement of N-atom densities under plasma pulsation depends on combination of several parameters such as cycle time t_c, duty cycle and pressure. It is ideal to have conditions where the duty cycle is quite small to have very high energy dissipated resulting in effective dissociation of molecules, yet the cycle time should not be long enough to deplete substantial amount of atoms during the decay phase. Thus, an optimal combination of cycle time and duty cycle needs to be chosen such that pulsation can effectively enhance the yields of N-atom densities. Experiments and simulations indicate that the pulsation is effective for frequency between 20 Hz and 50 Hz for the studied conditions.

7.2 Future perspectives

1. **Improvements in the laser experimental setup:** It is also feasible to make temporal measurements of emissions emanating from other lines which can be useful to further characterize the pulsed plasma. For example, the electron temperature and electron densities can be determined from the line-ratio methods [183]. This would require I) modifying the present optical setup by placing a monochromator in front of the PMT and II) also using a calibration lamp to perform a relative calibration of the optical system in order to take into account its spectral response. The

monochromator can then be used for selecting the different atomic lines that are necessary for the use of the Boltzmann plot method and the estimation of the electron temperature. The temporal signal will be captured in the same way as before as the PMT, MW and the laser are synchronized.

2. **Self-consistent models especially for pulsed plasmas:** Although the present CR model helps us in detailed investigation of plasma kinetics, the inherent limitation of missing details of plasma MW coupling makes it difficult to model the conditions accurately. In fact, MW-plasma coupling is very sensitive to the operating conditions such as the pressure, discharge gases etc. Therefore, it will be interesting to develop a fully self-consistent model for pulsed plasmas where both the Maxwell's equations for the MW electromagnetic radiation and conservative laws governing the plasma are solved. The self-consistent model can accurately predict the MW-plasma coupling and give us details such as plasma volume, MW power density etc. which were missing in our studies. Further, the local conditions obtained from the self-consistent model can be used to make detailed predictions of kinetics using the CR model.

3. **Optimization of pulsed plasma process on the reactor itself for increased yield of N density:** The studies performed in the thesis can be expanded to make optimization of the process in order to produce high yield of atomic nitrogen (or other gases like hydrogen, oxygen, … depending on the application). This improvement can be basically put in action following two different strategies: I) increasing the incident MW power provided by the supplier and II) implement a reactor chamber hosting more than one MW plasma sources. A greater input power produced by the MW power supplier, which can be achieved by new generation devices, such as the SAIREM® GMS 450 W, would significantly increase the explorable experimental conditions. In fact, greater MW average power could be achieved in a pulsed discharge at a given duty cycle condition and molecular nitrogen dissociation degree improved. The second proposed upgrade to the experimental setup, namely the implementation of a multi-source reactor, is another appealing solution. In fact, the adopted cavity in the experiments of this thesis is featured by high power reflections and plasmas were not always effectively sustained by a single source. A multi-source configuration will be of great usefulness in the frame of a recently-started project carried on by the LSPM, the "Institut de Minéralogie, de Physique des Matériaux et de Cosmochimie" (IMPMC), and the "Institut de Physique du Globe" (IPGP) whose core is based on the study of the mass independent fractionation (MIF) on titanium, for cosmochemistry applications (to reproduce in laboratory the chemical composition on presolar meteorites). This research has already brought to a published communication [184] and new results can still be obtained in the frame of an ANR

project (MIFs) that has just begun in 2021. The idea is to perform experimental studies on the interactions between $Ar/O_2/H_2O$ plasmas generated by four magnetized MW SAIREM sources with Ti and TiO_2 substrates. The applications where the results presented in this thesis can find a practical application can be found in a plethora of operational pressures. The upcoming sections illustrate the most relevant of these uses, presented following an increasing-pressure regime order.

4. **Low pressure regimes (1 – 100 Pa), plasmas for fusion reactors:** As mentioned in section 1.4, reactors suited to reproduce hydrogen fusion phenomena as observed in stars are object of studies since mid 20th century. Nitrogen plasmas may find a use in this technology. Molecular nitrogen, alongside other species as neon, is usually taken under consideration to be injected in the tokamak (like the ITER reactor) as cooling species, because of their capability to well dissipate energy in radiative way [185]. This need exists because the high temperatures reached in the chamber can seriously affect the divertor (highlighted in Figure 7.1) after reaching even 3695 K, the fusion temperature of their main structural component, massive tungsten.

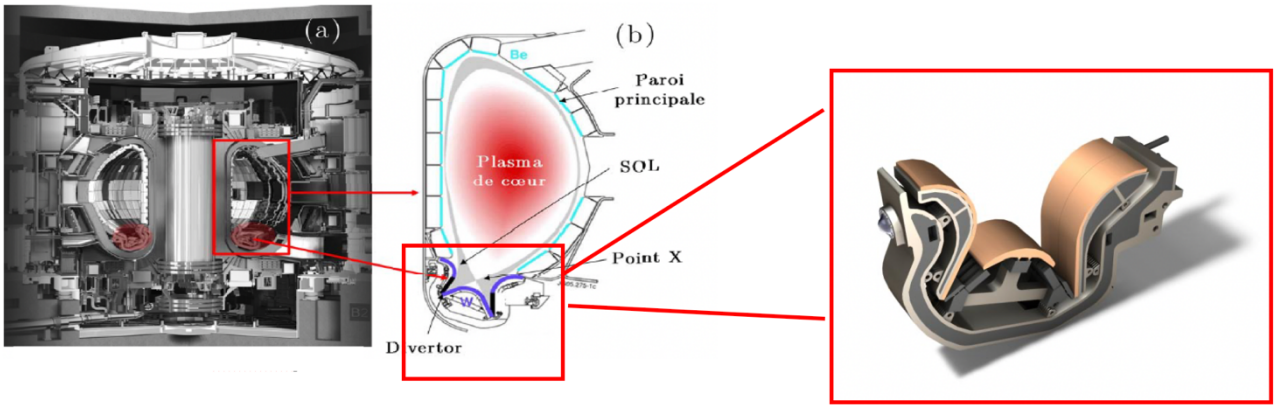

Figure 7.1: (a) internal view of a tokamak reactor. (b) scheme of a section, where the divertor is highlighted. Taken from [186]

A consequence to this would be the pollution of the plasma with W particles, an irreversible damaging of the whole structure, and an extinction of the fusion plasma. According to [185], N_2 should be introduced in the chamber from specific locations, placed under the dome of the divertor, as shown in Figure 7.2 (blue line).

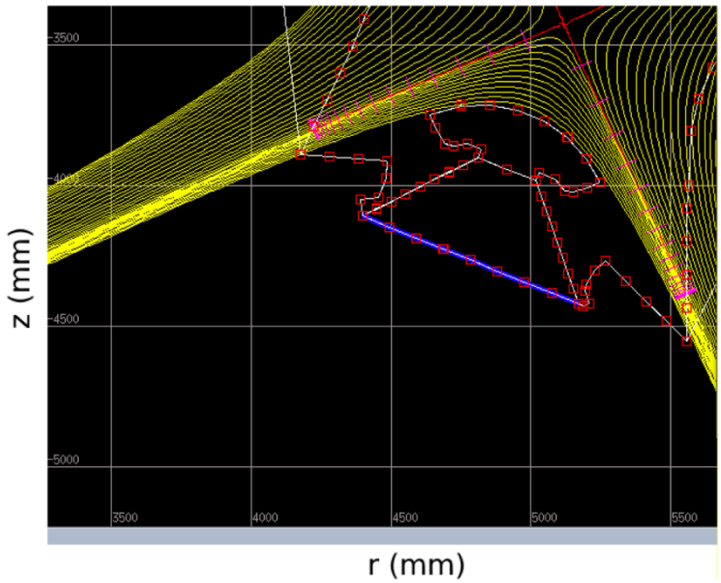

Figure 7.2: Scheme of the divertor and the best injection sites of N_2 (blue line). The yellow lines represent the magnetic field in the chamber. Taken from [185]

The image also highlights the theoretical lines that defines the X-point (red lines) while the yellow lines represent the magnetic field. The trajectory of the latter clearly changes whether a region above or below the X-point is considered. In the first scenario, magnetic field lines are closed, so that every ion of light species involved in the fusion process (namely, hydrogen and its isotopes deuterium and tritium) are confined within this area. On the other end, magnetic field lines located below the X-point are opened, so that all heavy charged particles can be addressed far from the chamber, including helium ions (the "ashes" of D+T fusion reaction). It has been estimated by theoretical studies that nitrogen atoms will be mostly located close to this region and, therefore, to the divertor (cf. Figure 7.3) [185].

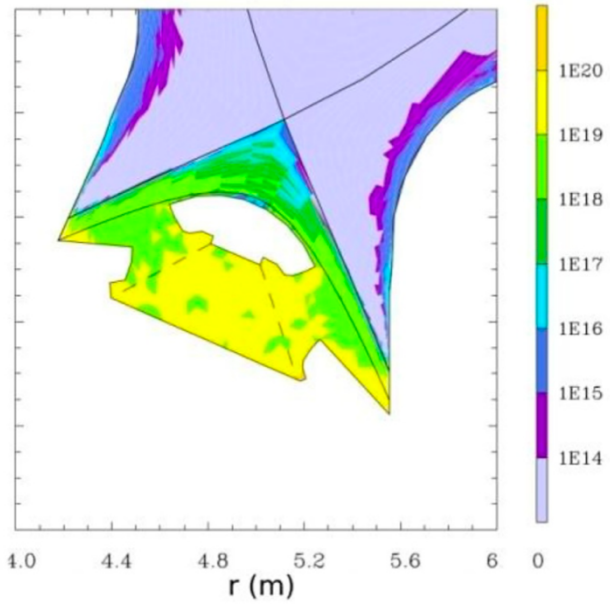

Figure 7.3: N-atom densities in the different regions defined by the X-point. Taken from [185]

Nevertheless, one of the main drawbacks related to the use of N_2 is that ammonia (NX_3, X = H, D, T) is generated in the reactor, after the interaction with hydrogen or its isotopes. This molecule will be therefore pumped out by the vacuum system, where these molecules, especially those highly tritiated, are a real threat to the pumps, causing permanent damages [187]. In addition to this, a number of studies performed in much colder plasmas proved that a tungsten surface in contact with a H_2/N_2 is much more deformed than one in a pure hydrogen plasma environment [187–189], as shown in Figure 7.4 (comparison of blisters occurrence in pure hydrogen plasma, and in hydrogen/nitrogen plasma), where the scanning electron microscopy (SEM) analysis of a test performed internally to the LSPM showed similar outcomes. The experiments were performed in the CASIMIR reactor, whose structure can be assumed as a system of 16 magnetized sources similar to the Aura-Wave (see [152,186,190] for more information), at 1 Pa, 2 kW and total flow of 60 sccm.

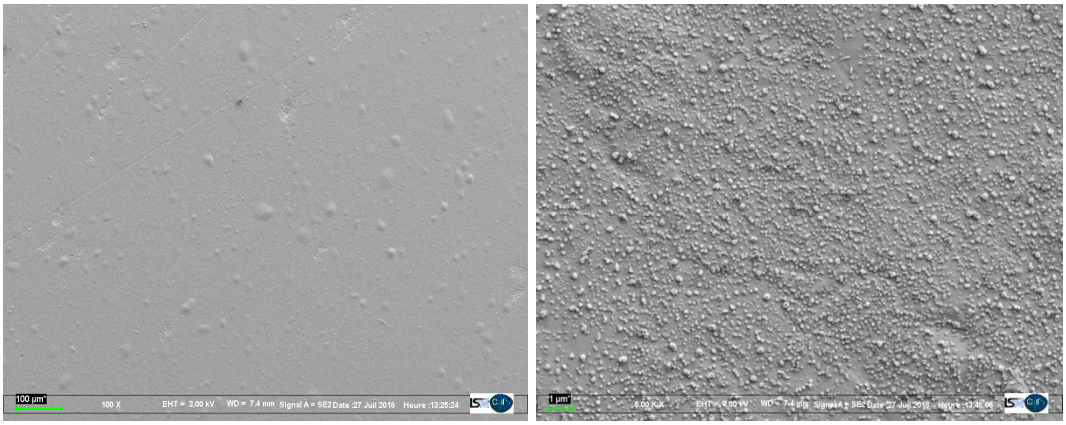

Figure 7.4: (left) SEM analysis on a tungsten surface in contact with a pure H_2 plasma, where a 10^{10} blisters m^{-2} density was measured. (right) SEM analysis on a tungsten surface in contact with a H_2/N_2 (10% of N_2) plasma, where a 10^{20} blisters m^{-2} density was measured.

The synthesis of ammonia in H_2/N_2 plasmas mediated by a tungsten substrate has been the object of another research (Project PHC Procope), where the LSPM cooperated with the "Leibniz-Institut für Plasmaforschung und Technologie e.V." (previously known as INP) to examine the effect of the substrate temperature, the distance from a Distributed Antenna Array (DAA) composed of 16 non-magnetized sources and the relative composition of the discharge. Two distances (0.1 m and 0.15 m), two substrate temperatures (573 K and 873 K) and a large number of different admixtures (ranging from 2% to 98% of N_2 content) conditions were studied at fixed pressure (50 Pa) and total mass flow (50 sccm). In the examined conditions, ammonia density seemed to be not affected by the substrate temperature nor its distance from plasma sources, as shown for NH_3 hot band in Figure 7.5. On the other hand, the discharge composition showed that the presence of N_2 included between 40% to 60% of the total flow assures the highest yield of ammonia production, being in agreement with previous similar studies performed on expanding Ar plasmas with H_2 and N_2 injected in the background at 20 Pa [25] (cf. condition 1 of Figure 7.6).

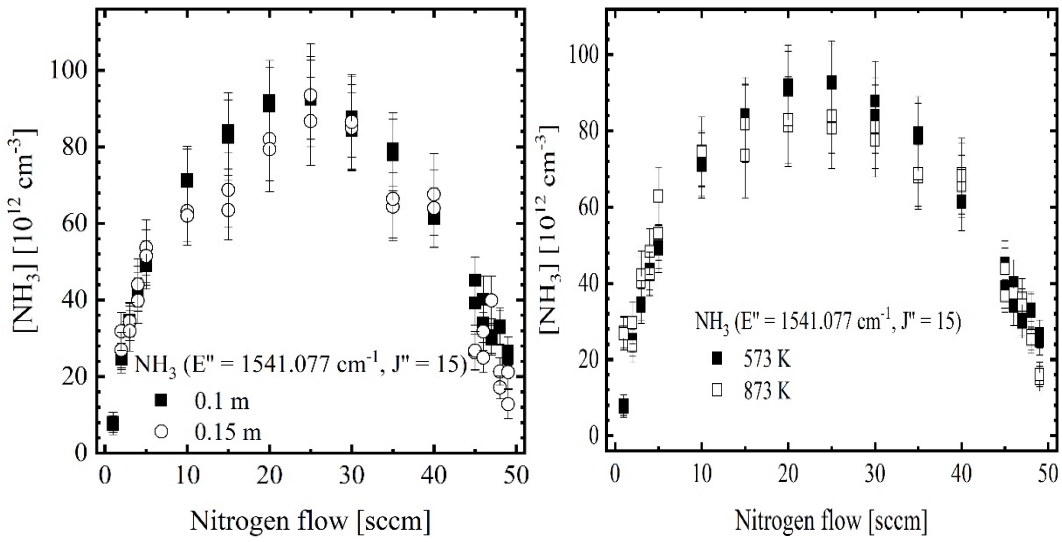

Figure 7.5: NH_3 hot band density calculated at (left) a substrate temperature of 573K and different distances from the DAA and (right) at 0.1 m from the DAA and different substrate temperatures.

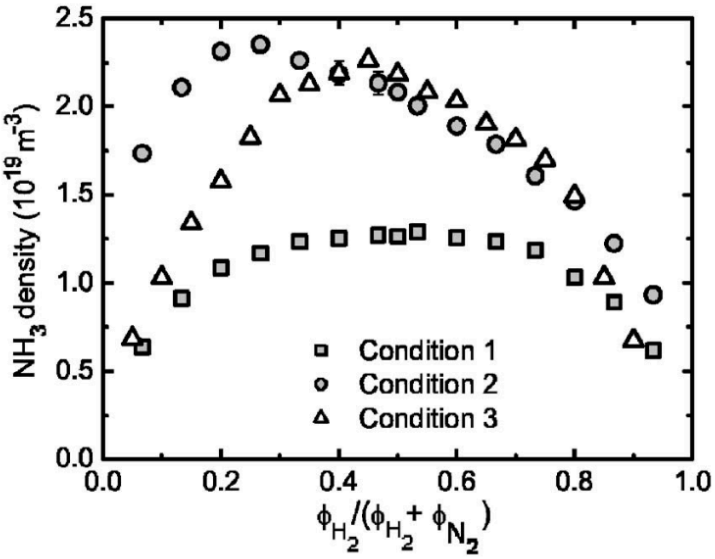

Figure 7.6: Ammonia density in an expanding Ar plasma with H_2 and N_2 injected in the background. Taken from [25]

5. **Medium-range pressure regimes (up to 5×10^3 Pa), synthesis of semi-conductors:** Nitrogen finds another field of application into the synthesis of hexagonal boron nitride (h-BN) and the LSPM proved to be an emerging research center in this field. Recent studies [46,191] performed on a micro-hollow cathode discharge (MHCD) proved how this source, working at approximatively 3.5×10^3 Pa, can effectively generate BN materials with stoichiometry 1:1, as presented by the Energy Dispersive X-ray Spectroscopy (EDS) results shown in Figure 7.7.

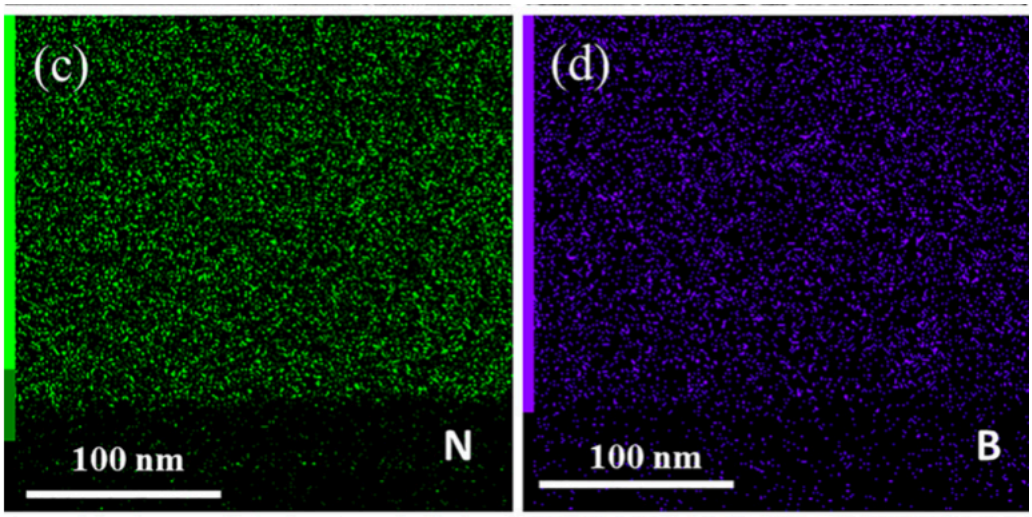

Figure 7.7: EDS mapping of (left) nitrogen and (right) boron. Taken from [46]

Quantification of N-atom density in the plasma process would be of prime importance in terms of optimization purpose. Therefore, the work devoted to TALIF in nitrogen-containing plasmas in this thesis can be very useful if applied in the MHCD reactor developed at LSPM.

6. **High pressure regimes (up to atmospheric pressure), applications in diamond synthesis:** It will be of interest to make studies on higher pressure conditions. At LSPM, there are other plasma sources such as the resonant cavity [97,98], working from 10 - 300 mbar, or a locally-designed MW torch, working from 50 mbar – 1 atm. One of the main studies performed in the same reactor had the goal to start investigating in the brand-new technologies based on solid-states quantum systems. Structures such as the one shown in Figure 7.8(a), inserted in specific positions of a centered cubic lattice in highly-pure diamonds synthetized via chemical vapor deposition (CVD), are featured by the replacement of a N atom and a vacancy (NV defect structures) to two carbon atoms. These structures are polarized by optical pumping and exhibit a spin-dependent photoluminescence. When a magnetic field is applied, the Electron Spin Resonance (ESR) is shifted because of Zeeman effect providing a quantitative measurement of the magnetic field. Because of complicated mechanisms described in the same reference, the NV defects have the potential to improve the speed of transfers of information in modern technologies.

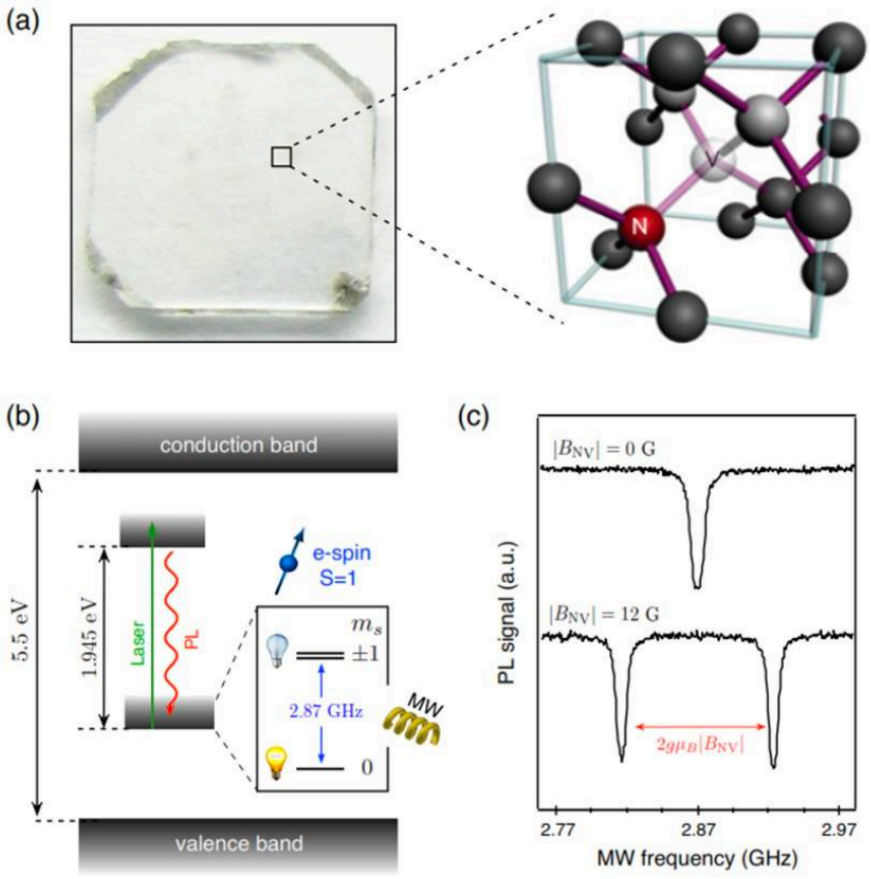

Figure 7.8: (a) a high-purity diamond synthetized via CVD, bearing a NV defect having a structure pointed on the right side. (b) Energy level scheme describing the spin-dependent photoluminescence. (c) Shift of the ESR transitions due to Zeeman effect. Taken from [1]

One more time, N- and H- atoms quantification by TALIF in the gas phase would be a key parameter to measure to improve the process. A detailed characterization of the discharges involved in this synthesis process might nevertheless be carried out by ps-pulsed laser and, therefore, by ultrafast TALIF spectroscopy, such as a ps- or fs-TALIF. The addition of a streak camera further powers up the setup and allows to capture the fluorescence decay time or quenching rates at higher pressures.

7. **ps-TALIF applied to determine the fluorescence decay time:** As shown in section 3.6, one of the difficulties with performing ns-TALIF with hydrogen was that the fluorescence decay time is too small for the detector to resolve and it is necessary to make models to predict the fluorescence decay rates. This obstacle is well known in the community of ns-based diagnostics, as large densities plasmas prove to be optically thick and quenching phenomena heavily limit the use of these diagnostics [192]. Unfortunately, as discussed in thesis, there is no clarity on the processes dominating the depletion of hydrogen excited states H(n=3) and there are several methods used in

the literature. This is especially true for very low pressures like that used in this thesis. It will be encouraging to use the ps-TALIF to study the fluorescence decay times of hydrogen at different operating conditions. This will help us to understand and identify the important processes that cause the depletion of H(n=3) states and improve the prediction of atomic hydrogen in the plasma.

A study on a ps-TALIF setup has been recently performed at the LSPM [193], highlighting promising results on Kr and the possibility to measure its lifetime in much higher pressures than those explored in this thesis. Nevertheless, one of the limitations posed by ps- and fs-based diagnostics is the control of the laser energy. In fact, ultrafast lasers present much higher instantaneous and similar average power than ns ones. This can be an issue in the study of pulsed discharges, where steep density gradients are observed in µm-scale dimensions and highly focused beams would be required to reach satisfying spatial resolutions. In a ps-laser, this would dramatically increase the chances of reaching locally-high energies, leading to photolytic effects or different way to deplete excited states, such as photoionization or amplified stimulated emission [149]. An example of these issues was reported by [193], the same author of the Figure 7.9, where the effects of laser energy and pressure on the excited state lifetime are pointed out in different pressures Kr plasmas.

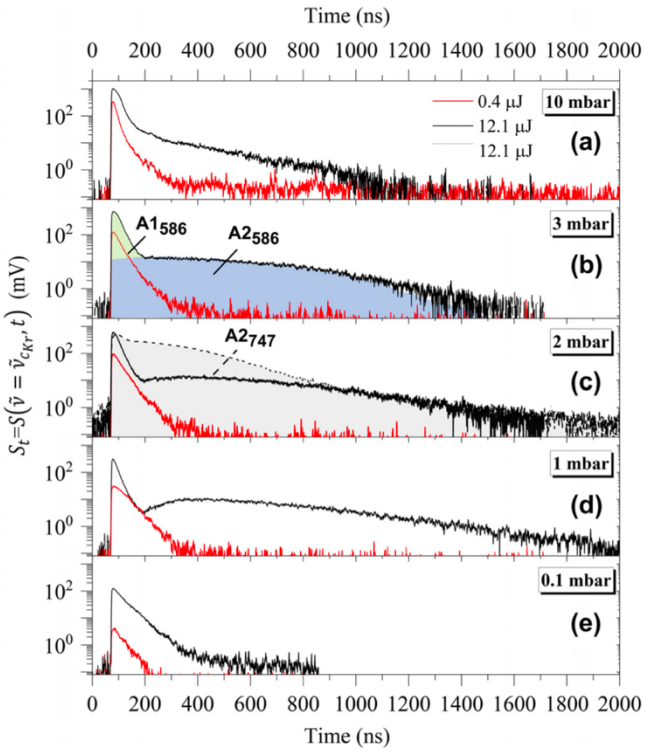

Figure 7.9: PMT signals of Kr-atoms in different pressures and laser energies. Reproduced from [193]

Ongoing studies on the ps-laser setup assembled in the LSPM already proved the detection of H-atom lifetime decay being possible, even at pressure of 2×10^4 Pa, as shown in Figure 7.10.

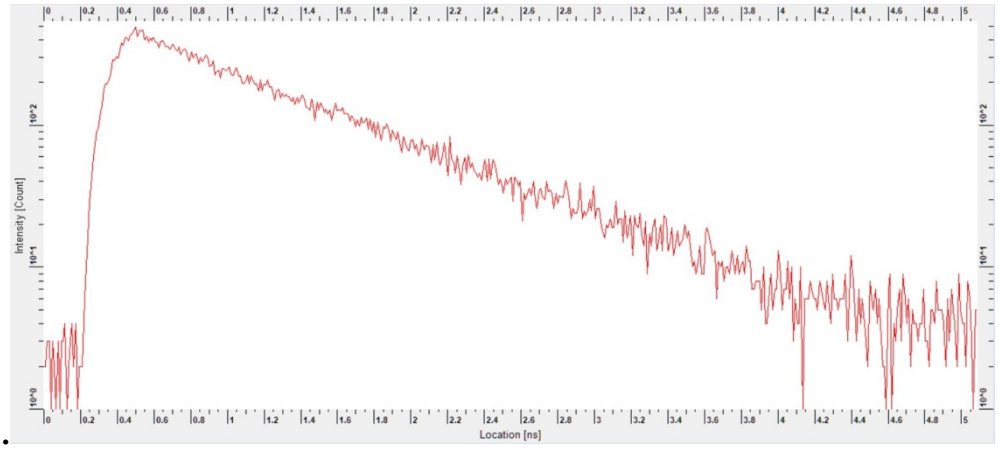

Figure 7.10: TALIF signal obtained in a 2×10⁴ Pa plasma, recorded using a streak camera.

Therefore, further analysis using similar tools might be of great help in determining quenching influence in high-pressure nitrogen discharges.

List of figures

References

[1] Achard J, Jacques V and Tallaire A 2020 Chemical vapour deposition diamond single crystals with nitrogen-vacancy centres: a review of material synthesis and technology for quantum sensing applications *J. Phys. D: Appl. Phys.* **53** 313001, DOI: 10.1088/1361-6463/ab81d1

[2] Achard J, Silva F, Tallaire A, Bonnin X, Lombardi G, Hassouni K and Gicquel A 2007 High quality MPACVD diamond single crystal growth: high microwave power density regime *J. Phys. D: Appl. Phys.* **40** 6175 , DOI: 10.1088/0022-3727/40/20/S04

[3] Silva F, Achard J, Brinza O, Bonnin X, Hassouni K, Anthonis A, De Corte K and Barjon J 2009 High quality, large surface area, homoepitaxial MPACVD diamond growth *Diamond and Related Materials* **18** 683–97 , DOI: 10.1016/j.diamond.2009.01.038

[4] Greenwood N N and Earnshaw A 1997 *Chemistry of the elements* (Oxford ; Boston: Butterworth-Heinemann) , ISBN: 978-0-7506-3365-9

[5] Malvaldi M 2017 *L'architetto dell'invisibile, ovvero, come pensa un chimico* (Raffaello Cortina Editore) , ISBN: 978-88-6030-946-4

[6] Bolin B and Arrhenius E 1977 Nitrogen: An Essential Life Factor and a Growing Environmental Hazard Report from Nobel Symposium No. 38 *Ambio* **6** 96–105

[7] Bottomley P J and Myrold D D 2007 14 - BIOLOGICAL N INPUTS *Soil Microbiology, Ecology and Biochemistry (Third Edition)* ed E A Paul (San Diego: Academic Press) pp 365–87, ISBN: 978-0-12-546807-7

[8] Robertson G P and Vitousek P M 2009 Nitrogen in Agriculture: Balancing the Cost of an Essential Resource 34

[9] Robertson G P and Groffman P M 2007 NITROGEN TRANSFORMATIONS *Soil Microbiology, Ecology and Biochemistry* (Elsevier) pp 341–64 , ISBN: 978-0-12-546807-7

[10] Sparacino-Watkins C, Stolz J F and Basu P 2014 Nitrate and periplasmic nitrate reductases *Chem. Soc. Rev.* **43** 676–706, DOI: 10.1039/C3CS60249D

[11] Kawai Y, Chen S, Honda Y, Yamaguchi M, Amano H, Kondo H, Hiramatsu M, Kano H, Yamakawa K, Den S and Hori M 2011 Achieving high-growth-rate in GaN homoepitaxy using high-density nitrogen radical source *physica status solidi c* **8** 2089–91, DOI: https://doi.org/10.1002/pssc.201000969

[12] Navarro-González R, McKay C P and Nna Mvondo D 2001 A possible nitrogen crisis for Archaean life due to reduced nitrogen fixation by lightning *Nature* **412** 61–4

[13] Lundberg J O, Gladwin M T, Ahluwalia A, Benjamin N, Bryan N S, Butler A, Cabrales P, Fago A, Feelisch M, Ford P C, Freeman B A, Frenneaux M, Friedman J, Kelm M, Kevil C G, Kim-Shapiro D B, Kozlov A V, Lancaster J R, Lefer D J, McColl K, McCurry K, Patel R P, Petersson J,

Rassaf T, Reutov V P, Richter-Addo G B, Schechter A, Shiva S, Tsuchiya K, van Faassen E E, Webb A J, Zuckerbraun B S, Zweier J L and Weitzberg E 2009 Nitrate and nitrite in biology, nutrition and therapeutics *Nat Chem Biol* **5** 865–9, DOI: 10.1038/nchembio.260

[14] Gallon J R 2001 N_2 fixation in phototrophs: adaptation to a specialized way of life 10

[15] Fryzuk M D 2009 Side-on End-on Bound Dinitrogen: An Activated Bonding Mode That Facilitates Functionalizing Molecular Nitrogen *Acc. Chem. Res.* **42** 127–33, DOI: 10.1021/ar800061g

[16] Müller T, Walter B, Wirtz A and Burkovski A 2006 Ammonium Toxicity in Bacteria *Curr Microbiol* **52** 400–6, DOI: 10.1007/s00284-005-0370-x

[17] King N L R and Bradbury J H 1968 The Chemical Composition of Wool V. The Epicuticle *Aust. Jnl. Of Bio. Sci.* **21** 375–84, DOI: 10.1071/bi9680375

[18] Bhavsar P, Zoccola M, Patrucco A, Montarsolo A, Mossotti R, Rovero G, Giansetti M and Tonin C 2016 Superheated Water Hydrolysis of Waste Wool in a Semi-Industrial Reactor to Obtain Nitrogen Fertilizers *ACS Sustainable Chem. Eng.* **4** 6722–31, DOI: 10.1021/acssuschemeng.6b01664

[19] Kavanagh K L, Guo K, Dunford J E, Wu X, Knapp S, Ebetino F H, Rogers M J, Russell R G G and Oppermann U 2006 The molecular mechanism of nitrogen-containing bisphosphonates as antiosteoporosis drugs *PNAS* **103** 7829–34 , DOI: 10.1073/pnas.0601643103

[20] Takami A, Iijima H, Iwakubo M and Okada Y 2007 Nitrogen-containing compounds having kinase inhibitory activity and drugs containing the same

[21] Nishizawa R, Takaoka Y and Shibayama S 2011 Nitrogen-containing heterocyclic derivatives and drugs containing the same as the active ingredient

[22] Xie H and Cao Z 2010 Enzymatic Reduction of Nitrate to Nitrite: Insight from Density Functional Calculations *Organometallics* **29** 436–41, DOI: 10.1021/om9008197

[23] Li S, Medrano J A, Hessel V and Gallucci F 2018 Recent Progress of Plasma-Assisted Nitrogen Fixation Research: A Review *Processes* **6** 248, DOI: 10.3390/pr6120248

[24] Smill V and Streatfeild R A 2002 Enriching the Earth: Fritz Haber, Carl Bosch, and the Transformation of World Food (review) *Technology and Culture* **43** 622–3, DOI: 10.1353/tech.2002.0114

[25] van Helden J H, Wagemans W, Yagci G, Zijlmans R a. B, Schram D C, Engeln R, Lombardi G, Stancu G D and Röpcke J 2007 Detailed study of the plasma-activated catalytic generation of ammonia in N_2-H_2 plasmas *Journal of Applied Physics* **101** 043305, DOI: 10.1063/1.2645828

[26] Hong J, Pancheshnyi S, Tam E, Lowke J J, Prawer S and Murphy A B 2017 Kinetic

modelling of NH_3 production in N_2–H_2 non-equilibrium atmospheric-pressure plasma catalysis *Journal of Physics D: Applied Physics* **50** 154005

[27] Van Alphen S, Vermeiren V, Butterworth T, van den Bekerom D C M, van Rooij G J and Bogaerts A 2020 Power Pulsing To Maximize Vibrational Excitation Efficiency in N_2 Microwave Plasma: A Combined Experimental and Computational Study *J. Phys. Chem. C* **124** 1765–79, DOI: 10.1021/acs.jpcc.9b06053

[28] Tanabe Y and Nishibayashi Y 2013 Developing more sustainable processes for ammonia synthesis *Coordination Chemistry Reviews* **257** 2551–64, DOI: 10.1016/j.ccr.2013.02.010

[29] Anastasopoulou A, Wang Q, Hessel V and Lang J 2014 Energy Considerations for Plasma-Assisted N-Fixation Reactions *Processes* **2** 694–710, DOI: 10.3390/pr2040694

[30] Wang W, Patil B, Heijkers S, Hessel V and Bogaerts A 2017 Nitrogen fixation by gliding arc plasma: better insight by chemical kinetics modelling. *European Chemical Societies Publishing* 14

[31] Liu D and Lu X 2014 Introduction *Low Temperature Plasma Technology* (Taylor & Francis Group) pp 3–11, ISBN: 978-0-367-57636-3

[32] Goossens M 2003 *An Introduction to Plasma Astrophysics and Magnetohydrodynamics* vol 294 (Dordrecht: Springer Netherlands), ISBN: 978-94-007-1076-4

[33] Langmuir I 1928 Oscillations in ionized gases *Proc Natl Acad Sci U S A.* **14** 627–37, DOI: 10.1073/pnas.14.8.627

[34] Tonks L and Langmuir I 1929 Oscillations in Ionized Gases *Phys. Rev.* **33** 195–210, DOI: 10.1103/PhysRev.33.195

[35] Eliezer Y and Eliezer S 2001 *The fourth state of matter: an introduction to plasma science* (Bristol, UK; Philadelphia: IOP), ISBN: 978-0-7503-0740-6

[36] Samukawa S, Hori M, Rauf S, Tachibana K, Bruggeman P, Kroesen G, Whitehead J C, Murphy A B, Gutsol A F, Starikovskaia S, Uwe Kortshagen, Boeuf J-P, Sommerer T J, Kushner M J, Czarnetzki U and Mason N 2012 The 2012 Plasma Roadmap *J. Phys. D: Appl. Phys.* **45** 253001, DOI: 10.1088/0022-3727/45/25/253001

[37] Otorbaev D K, Sanden M C M van de and Schram D C 1995 Heterogeneous and homogeneous hydrogen kinetics in plasma chemistry *Plasma Sources Sci. Technol.* **4** 293–301, DOI: 10.1088/0963-0252/4/2/013

[38] Baudrillart B, Nave A S C, Hamann S, Bénédic F, Lombardi G, van Helden J H, Röpcke J and Achard J 2017 Growth processes of nanocrystalline diamond films in microwave cavity and distributed antenna array systems: A comparative study *Diamond and Related Materials* **71** 53–62, DOI: 10.1016/j.diamond.2016.11.018

[39] Dvořák P, Talába M, Obrusník A, Kratzer J and Dědina J 2017 Concentration of atomic hydrogen in a dielectric barrier discharge measured by two-photon absorption fluorescence *Plasma Sources Science and Technology* **26** 085002, DOI: 10.1088/1361-6595/aa76f7

[40] Tsuda M, Nakajima M and Oikawa S 1986 Epitaxial Growth Mechanism of Diamond Crystal in CH_4-H_2 Plasma *J. Am. Chem. Soc.* **108** 5780–3, DOI: 10.1002\/chin.198705153

[41] Ausschnitt C P, Bjorklund G C and Freeman R R 1978 Hydrogen plasma diagnostics by resonant multiphoton optogalvanic spectroscopy *Appl. Phys. Lett.* **33** 851–3, DOI: 10.1063/1.90211

[42] Adams S F and Miller T A 1998 Two-photon absorption laser-induced fluorescence of atomic nitrogen by an alternative excitation scheme *Chemical Physics Letters* **295** 305–11, DOI: 10.1016/S0009-2614(98)00972-5

[43] Czerwiec T, Greer F and Graves D B 2005 Nitrogen dissociation in a low pressure cylindrical ICP discharge studied by actinometry and mass spectrometry *J. Phys. D: Appl. Phys.* **38** 4278–89, DOI: 10.1088/0022-3727/38/24/003

[44] Ono R, Teramoto Y and Oda T 2009 Measurement of Atomic Nitrogen in N_2 Pulsed Positive Corona Discharge Using Two-Photon Absorption Laser-Induced Fluorescence *Jpn. J. Appl. Phys.* **48** 122302, DOI: 10.1143/JJAP.48.122302

[45] Gleiman S, Chen C-K, Datye A and Phillips J 2002 Melting and spheroidization of hexagonal boron nitride in a microwave-powered, atmospheric pressure nitrogen plasma *Journal of Materials Science* **37** 3429–40, DOI: 10.1023/A:1016502804363

[46] Kabbara H, Kasri S, Brinza O, Bauville G, Gazeli K, Santos Sousa J, Mille V, Tallaire A, Lombardi G and Lazzaroni C 2020 A microplasma process for hexagonal boron nitride thin film synthesis *Appl. Phys. Lett.* **116** 171902, DOI: 10.1063/1.5143948

[47] Lazzaroni C, Kabbara H, Kasri S, William L, Mille V, Aubert X, Lombardi G and Tallaire A 2018 Synthesis of boron nitride using a micro hollow cathode discharge deposition reactor. LW1.057

[48] Mazouffre S, Foissac C, Supiot P, Vankan P, Engeln R, Schram D and Sadeghi N 2001 Density and temperature of N atoms in the afterglow of a microwave discharge measured by a two-photon laser-induced fluorescence technique *Plasma Sources Science and Technology* **10** 168, DOI: 10.1088\/0963-0252\/10\/2\/306

[49] Guerra V, Dias F M, Loureiro J, Sa P A, Supiot P, Dupret C and Popov T 2003 Time-dependence of the electron energy distribution function in the nitrogen afterglow *IEEE Transactions on Plasma Science* **31** 542–51, DOI: 10.1109/TPS.2003.815485

[50] Gaboriau F, Cvelbar U, Mozetic M, Erradi A and Rouffet B 2009 Comparison of TALIF and catalytic probes for the determination of nitrogen atom density in a nitrogen plasma afterglow *J. Phys. D: Appl. Phys.* **42** 055204, DOI: 10.1088/0022-3727/42/5/055204

[51] Es-sebbar E, C-Gazeau M, Benilan Y, Jolly A and Pintassilgo C D 2010 Absolute ground-state nitrogen atom density in a N_2/CH_4 late afterglow: TALIF experiments and modelling studies *J. Phys. D: Appl. Phys.* **43** 335203, DOI: 10.1088/0022-3727/43/33/335203

[52] Es-Sebbar E, Benilan Y, Jolly A and Gazeau M 2009 Characterization of an N_2 flowing microwave post-discharge by OES spectroscopy and determination of absolute ground-state nitrogen atom densities by TALIF *Journal of Physics D: Applied Physics* **42** 135206, DOI: 10.1088\/0022-3727\/42\/13\/135206

[53] Repsilber T, Baeva M and Uhlenbusch J 2004 Spatial and temporal characteristics of atomic nitrogen in a pulsed microwave discharge *Plasma Sources Science and Technology* **13** 58–67, DOI: 10.1088/0963-0252/13/1/008

[54] Sá P, Guerra V, Loureiro J and Sadeghi N 2003 Self-consistent kinetic model of the short-lived afterglow in flowing nitrogen *Journal of Physics D: Applied Physics* **37** 221, DOI: 10.1088\/0022-3727\/37\/2\/010

[55] Jafarpour S M, Puth A, Dalke A, Böcker J, Pipa AndreiV, Röpcke J, van Helden J-P H and Biermann H 2020 Solid carbon active screen plasma nitrocarburizing of AISI 316L stainless steel in cold wall reactor: influence of plasma conditions *Journal of Materials Research and Technology* **9** 9195–205, DOI: 10.1016/j.jmrt.2020.06.041

[56] Henrion G, Fabry M, Hugon R and Bougdira J 1992 Spectroscopic investigation of a temporal post-discharge plasma for iron nitriding *Plasma Sources Sci. Technol.* **1** 117–21, DOI: 10.1088/0963-0252/1/2/007

[57] Es-Sebbar E-T, Sarra-Bournet C, Naudé N, Massines F and Gherardi N 2009 Absolute nitrogen atom density measurements by two-photon laser-induced fluorescence spectroscopy in atmospheric pressure dielectric barrier discharges of pure nitrogen *Journal of Applied Physics* **106** 073302, DOI: 10.1063/1.3225569

[58] Rouffet B, Gaboriau F and Sarrette J 2010 Pressure dependence of the nitrogen atom recombination probability in late afterglows *Journal of Physics D: Applied Physics* **43** 185203, DOI: 10.1088\/0022-3727\/43\/18\/185203

[59] Pointu A-M, Ricard A, Odic E and Ganciu M 2008 Nitrogen Atmospheric Pressure Post Discharges for Surface Biological Decontamination inside Small Diameter Tubes *Plasma Processes and Polymers* **5** 559–68, DOI: 10.1002/ppap.200800016

[60] Wagenaars E, Gans T, O'Connell D and Niemi K 2012 Two-photon absorption laser-induced fluorescence measurements of atomic nitrogen in a radio-frequency atmospheric-pressure plasma jet *Plasma Sources Sci. Technol.* **21** 042002, DOI: 10.1088/0963-0252/21/4/042002

[61] Dumitrache C, Gallant A, Stancu G D and Laux C O 2019 Measurements of ground state atomic nitrogen in high-pressure NRP discharges using fs-TALIF (Naples, Italy), DOI: 10.1088\/0963-0252\/14\/2\/S05

[62] Dumitrache C, Gallant A, Stancu G-D and Laux C O 2019 Femtosecond Two-Photon Absorption Laser Induced Fluorescence (fs-TALIF) Imaging of Atomic Nitrogen in Nanosecond Repetitive Discharges *AIAA Scitech 2019 Forum* AIAA Scitech 2019 Forum (San Diego, California: American Institute of Aeronautics and Astronautics), DOI: 10.2514/6.2019-1507

[63] Mézerette D, Belmonte T, Hugon R, Czerwiec T, Henrion G and Michel H 2001 Surface cleaning and passivation of an iron foil by a nitrogen post-discharge surface treatment *Surface and Coatings Technology* **142–144** 761–6, DOI: 10.1016/S0257-8972(01)01116-1

[64] Lukas C, Spaan M, Gathen V S der, Thomson M, Wegst R, Döbele H F and Neiger M 2001 Dielectric barrier discharges with steep voltage rise: mapping of atomic nitrogen in single filaments measured by laser-induced fluorescence spectroscopy *Plasma Sources Science and Technology* **10** 445, DOI: 10.1088\/0963-0252\/10\/3\/308

[65] Stancu G D 2020 Two-photon absorption laser induced fluorescence: rate and density-matrix regimes for plasma diagnostics *Plasma Sources Sci. Technol.* **29** 054001, DOI: 10.1088/1361-6595/ab85d0

[66] Teramoto Y, Ono R and Oda T 2012 Production mechanism of atomic nitrogen in atmospheric pressure pulsed corona discharge measured using two-photon absorption laser-induced fluorescence *Journal of Applied Physics* **111** 113302, DOI: 10.1063\/1.4722317

[67] Mazouffre S, Bakker I, Vankan P, Engeln R and Schram D 2002 Two-photon laser induced fluorescence spectroscopy performed on free nitrogen plasma jets *Plasma Sources Science and Technology* **11** 439, DOI: 10.1088\/0963-0252\/11\/4\/311

[68] Bekeschus S, Schmidt A, Weltmann K-D and von Woedtke T 2016 The plasma jet kINPen–a powerful tool for wound healing *Clinical Plasma Medicine* **4** 19–28, DOI: 10.1016\/j.cpme.2016.01.001

[69] Schmidt-Bleker A, Winter J, Bösel A, Reuter S and Weltmann K-D 2015 On the plasma chemistry of a cold atmospheric argon plasma jet with shielding gas device *Plasma Sources Sci. Technol.* **25** 015005, DOI: 10.1088/0963-0252/25/1/015005

[70] Ju Y and Sun W 2015 Plasma assisted combustion: Dynamics and chemistry *Progress in Energy and Combustion Science* **48** 21–83, DOI: 10.1016\/j.pecs.2014.12.002

[71] Bittner J, Lawitzki A, Meier U and Kohse-Höinghaus K 1991 Nitrogen atom detection in low-pressure flames by two-photon laser-excited fluorescence *Appl. Phys. B* **52** 108–16, DOI: 10.1007/BF00357664

[72] Lo A, Cessou A, Boubert P and Vervisch P 2014 Space and time analysis of the nanosecond scale discharges in atmospheric pressure air: I. Gas temperature and vibrational distribution function of N_2 and O_2 *J. Phys. D: Appl. Phys.* **47** 115201, DOI: 10.1088/0022-3727/47/11/115201

[73] Amorim J, Baravian G and Jolly J 2000 Laser-induced resonance fluorescence as a diagnostic technique in non-thermal equilibrium plasmas *Journal of Physics D: Applied Physics* **33** R51, DOI: 10.1088\/0022-3727\/33\/9\/201

[74] Cacciatore M, Cappelli M and Gorse C 1982 Non-equilibrium dissociation and ionization of nitrogen in electrical discharges: The role of electronic collisions from vibrationally excited molecules *Chemical Physics* **66** 141–51, DOI: 10.1016/0301-0104(82)88013-0

[75] Gudmundsson J T and Hecimovic A 2017 Foundations of DC plasma sources *Plasma Sources Sci. Technol.* **26** 123001, DOI: 10.1088/1361-6595/aa940d

[76] Fridman A 2008 *Plasma Chemistry* (Cambridge), ISBN: 978-1-107-68493-5

[77] Laroussi M, Alexeff I, Richardson J P and Dyer F F 2002 The resistive barrier discharge *IEEE Transactions on Plasma Science* **30** 158–9, DOI: 10.1109/TPS.2002.1003972

[78] Ebert U, Rafatov I R and Šijačic D D 2007 Structure formation in a DC-driven ”barrier” discharge: stability analysis and numerical solutions 28th ICPIG (Prague, Czech Republic) p 3

[79] Mehdizadeh M 2015 Chapter 10 - Plasma applicators at RF and microwave frequencies *Microwave/RF Applicators and Probes (Second Edition)* ed M Mehdizadeh (Boston: William Andrew Publishing) pp 335–63, ISBN: 978-0-323-32256-0

[80] Becker K H, Schoenbach K H and Eden J G 2006 Microplasmas and applications *J. Phys. D: Appl. Phys.* **39** R55–70, DOI: 10.1088/0022-3727/39/3/R01

[81] Uhm H S, Hong Y C and Shin D H 2006 A microwave plasma torch and its applications *Plasma Sources Sci. Technol.* **15** S26–34, DOI: 10.1088/0963-0252/15/2/S04

[82] Lombardi G 2016 *Études de procédés plasmas micro-ondes: applications à la synthèse de matériaux et à l’interaction plasma-surface* (Université Paris 13)

[83] Hashizume H, Ohta T, Fengdong J, Takeda K, Ishikawa K, Hori M and Ito M 2013 Inactivation effects of neutral reactive-oxygen species on Penicillium digitatum spores using non-equilibrium atmospheric-pressure oxygen radical source *Appl. Phys. Lett.* **103** 153708

[84] Adamovich I, Baalrud S D, Bogaerts A, Bruggeman P, Cappelli M, Colombo V, Czarnetzki U, Ebert U, Eden J, Favia P, Graves, D, Hamaguchi S, Hieftje G, Hori M, Kaganovich I, and others

2017 The 2017 Plasma Roadmap: Low temperature plasma science and technology *Journal of Physics D: Applied Physics* **50** 323001, DOI: 10.1063/1.4824892

[85] Bartschat K and Kushner M J 2016 Electron collisions with atoms, ions, molecules, and surfaces: Fundamental science empowering advances in technology *PNAS* **113** 7026–34, DOI: 10.1073/pnas.1606132113

[86] Elliott D B 2016 *Two Photon Absorption Laser Induced Fluorescence for Fusion Class Plasmas* (West Virginia University)

[87] *https://www.sairem.com/*

[88] Dumitrache C, Gallant A, Minesi N, Stepanyan S, Stancu G D and Laux C O 2019 Hydrodynamic regimes induced by nanosecond pulsed discharges in air: mechanism of vorticity generation *J. Phys. D: Appl. Phys.* **52** 364001, DOI: 10.1088/1361-6463/ab28f9

[89] Klochko A V, Lemainque J, Booth J P and Starikovskaia S M 2015 TALIF measurements of oxygen atom density in the afterglow of a capillary nanosecond discharge *Plasma Sources Sci. Technol.* **24** 025010, DOI: 10.1088/0963-0252/24/2/025010

[90] Chng T L, Lepikhin N D, Orel I S, Popov N A and Starikovskaia S M 2020 TALIF measurements of atomic nitrogen in the afterglow of a nanosecond capillary discharge *Plasma Sources Sci. Technol.* **29** 035017, DOI: 10.1088/1361-6595/ab6f9c

[91] Orel I 2020 *Measurements of electric field and dissociated species in nanosecond discharges for kinetic and biological applications* (Institut Polytechnique de Paris)

[92] Hopwood J, Hoskinson A R and Gregório J 2014 Microplasmas ignited and sustained by microwaves *Plasma Sources Science and Technology* **23** 064002, DOI: 10.13039\/100000181

[93] Iza F and Hopwood J 2005 Split-ring resonator microplasma: microwave model, plasma impedance and power efficiency *Plasma Sources Science and Technology* **14** 397, DOI: 10.1088\/0963-0252\/14\/2\/023

[94] Choi J, Iza F, Do H J, Lee J K and Cho M H 2009 Microwave-excited atmospheric-pressure microplasmas based on a coaxial transmission line resonator *Plasma Sources Sci. Technol.* **18** 025029, DOI: 10.1088/0963-0252/18/2/025029

[95] Holtrup S and Heuermann H 2009 Fundamentals and ignition of a microplasma at 2.45 GHz *Microwave Conference, 2009. EuMC 2009. European* (IEEE) pp 1607–9

[96] Hassouni K, Duten X, Rousseau A and Gicquel A 2001 Investigation of chemical kinetics and energy transfer in a pulsed microwave H_2/CH_4 plasma *Plasma Sources Science and Technology* **10** 61–75, DOI: 10.1088/0963-0252/10/1/309

[97] Prasanna S, Michau A, Rond C, Hassouni K and Gicquel A 2017 Self-consistent simulation studies on effect of methane concentration on microwave assisted H_2-CH_4 plasma at low pressure *Plasma Sources Sci. Technol.* **26** 097001, DOI: 10.1088/1361-6595/aa8062

[98] Prasanna S, Rond C, Michau A, Hassouni K and Gicquel A 2016 Effect of buoyancy on power deposition in microwave cavity hydrogen plasma source *Plasma Sources Sci. Technol.* **25** 045017, DOI: 10.1088/0963-0252/25/4/045017

[99] Stancu G, Janda M, Kaddouri F, Lacoste D, Rolon J, Laux C and Pai D 2008 Two Photon Absorption Laser Induced Fluorescence Study of Repetitively Pulsed Nanosecond Discharges in Atmospheric Pressure Air *39th Plasmadynamics and Lasers Conference* (American Institute of Aeronautics and Astronautics), DOI: 10.2514\/6.2008-3882

[100] Stancu G D, Kaddouri F, Lacoste D A and Laux C O 2010 Atmospheric pressure plasma diagnostics by OES, CRDS and TALIF *J. Phys. D: Appl. Phys.* **43** 124002, DOI: 10.1088/0022-3727/43/12/124002

[101] Rusterholtz D L, Lacoste D A, Stancu G D, Pai D Z and Laux C O 2013 Ultrafast heating and oxygen dissociation in atmospheric pressure air by nanosecond repetitively pulsed discharges *J. Phys. D: Appl. Phys.* **46** 464010, DOI: 10.1088/0022-3727/46/46/464010

[102] Lo A, Cessou A and Vervisch P 2014 Space and time analysis of the nanosecond scale discharges in atmospheric pressure air: II. Energy transfers during the post-discharge *J. Phys. D: Appl. Phys.* **47** 115202, DOI: 10.1088/0022-3727/47/11/115202

[103] Popov N A 2001 Investigation of the mechanism for rapid heating of nitrogen and air in gas discharges *Plasma Phys. Rep.* **27** 886–96, DOI: 10.1134/1.1409722

[104] Capitelli M, Ferreira C M, Gordiets B F and Osipov A I 2013 *Plasma kinetics in atmospheric gases* vol 31 (Springer Science & Business Media), ISBN: 978-3-662-04158-1

[105] Popov N 2013 Fast gas heating initiated by pulsed nanosecond discharge in atmospheric pressure air *51st AIAA Aerospace Sciences Meeting including the New Horizons Forum and Aerospace Exposition* (Gravepine, TX: American Institute of Aeronautics and Astronautics), DOI: 10.2514\/6.2013-1052

[106] Capitelli M, Colonna G, D'Ammando G, Laporta V and Laricchiuta A 2014 Nonequilibrium dissociation mechanisms in low temperature nitrogen and carbon monoxide plasmas *Chemical Physics* **438** 31–6, DOI: 10.1016/j.chemphys.2014.04.003

[107] Colonna G and Capitelli M 2001 Self-Consistent Model of Chemical, Vibrational, Electron Kinetics in Nozzle Expansion *Journal of Thermophysics and Heat Transfer* **15** 308–16, DOI: 10.2514/2.6627

[108] Popov N A 2013 Vibrational kinetics of electronically-excited $N_2(A^3\Sigma^+_u,v)$ molecules in nitrogen discharge plasma *J. Phys. D: Appl. Phys.* **46** 355204, DOI: 10.1088/0022-3727/46/35/355204

[109] Popov N 2013 Dissociation of nitrogen in a pulse-periodic dielectric barrier discharge at atmospheric pressure *Plasma Physics Reports* **39** 420–4, DOI: 10.1134\/s1063780x13050085

[110] Laity G, Fierro A, Dickens J, Frank K and Neuber A 2014 A passive measurement of dissociated atom densities in atmospheric pressure air discharge plasmas using vacuum ultraviolet self-absorption spectroscopy *Journal of Applied Physics* **115** 123302, DOI: 10.1063/1.4869895

[111] Polak L, Slovetskii D and Sokolov A 1972 Predissociation and quenching probabilities for the vibrational levels of the $B^3\Pi_g$ state of molecular nitrogen *Energ.* **6** 396

[112] Mintoussov E I, Pendleton S J, Gerbault F G, Popov N A and Starikovskaia S M 2011 Fast gas heating in nitrogen–oxygen discharge plasma: II. Energy exchange in the afterglow of a volume nanosecond discharge at moderate pressures *J. Phys. D: Appl. Phys.* **44** 285202, DOI: 10.1088/0022-3727/44/28/285202

[113] Popov N A 2008 Effect of a pulsed high-current discharge on hydrogen-air mixtures *Plasma Physics Reports* **34** 376–91, DOI: 10.1134/S1063780X08050048

[114] Armenise I, Capitelli M, Garcia E, Gorse C, Laganà A and Longo S 1992 Deactivation dynamics of vibrationally excited nitrogen molecules by nitrogen atoms. Effects on non-equilibrium vibrational distribution and dissociation rates of nitrogen under electrical discharges *Chemical Physics Letters* **200** 597–604, DOI: 10.1016/0009-2614(92)80097-U

[115] Guerra V, Sá P A and Loureiro J 2004 Kinetic modeling of low-pressure nitrogen discharges and post-discharges *Eur. Phys. J. Appl. Phys.* **28** 125–52, DOI: 10.1051/epjap:2004188

[116] Latrasse L, Radoiu M, Lo J and Guillot P 2016 2.45-GHz microwave plasma sources using solid-state microwave generators. ECR-type plasma source *Journal of Microwave Power and Electromagnetic Energy* **50** 308–21, DOI: 10.1080/08327823.2016.1260880

[117] Latrasse L, Radoiu M, Nelis T and Antonin O 2017 Self-matching plasma sources using 2.45 GHz solid-state generators: microwave design and operating performance *Journal of Microwave Power and Electromagnetic Energy* **51** 237–58, DOI: 10.1080/08327823.2017.1388338

[118] Latrasse L, Radoiu M, Lo J and Guillot P 2017 2.45-GHz microwave plasma sources using solid-state microwave generators. Collisional-type plasma source *Journal of Microwave Power and Electromagnetic Energy* **51** 43–58, DOI: 10.1080/08327823.2017.1293589

[119] Bisceglia E, Prasanna S, Gazeli K, Aubert X, Duluard C Y, Lombardi G and Hassouni K 2021 Investigation of $N(^4S)$ kinetics during the transients of a strongly emissive pulsed ECR plasma using ns-TALIF *Plasma Sources Sci. Technol.* **30** 095001, DOI: 10.1088/1361-6595/ac0da1

[120] Latrasse L and Radoiu M 2018 Elementary device for producing a plasma, having a coaxial applicator, Patent number: US10103006B2

[121] Villermaux J 1999 *Génie de la réaction chimique* (TECHNIQUE & DOC), ISBN: 978-2-85206-759-2

[122] Scacchi G, Bouchy M, Foucaut J-F, Zahraa O and Fournet R 2011 *Cinétique et catalyse* (TECHNIQUE & DOC), ISBN: 978-2-7430-1392-9

[123] Bokor J, Freeman R, White J and Storz R 1981 Two-photon excitation of the n=3 level in H and D atoms *Physical Review A* **24** 612, DOI: 10.1109\/jqe.1981.1071042

[124] Bischel W K, Perry B E and Crosley D R 1981 Two-photon laser-induced fluorescence in oxygen and nitrogen atoms *Chemical Physics Letters* **82** 85–8, DOI: 10.1016\/0009-2614(81)85112-3

[125] Bengtsson G J, Larsson J, Svanberg S and Wang D D 1992 Natural lifetimes of excited states of neutral nitrogen determined by time-resolved laser spectroscopy *Phys. Rev. A* **45** 2712–5, DOI: 10.1103/PhysRevA.45.2712

[126] Boogaarts M G H, Mazouffre S, Brinkman G J, van der Heijden H W P, Vankan P, van der Mullen J A M, Schram D C and Döbele H F 2002 Quantitative two-photon laser-induced fluorescence measurements of atomic hydrogen densities, temperatures, and velocities in an expanding thermal plasma *Review of Scientific Instruments* **73** 73–86, DOI: 10.1063/1.1425777

[127] Niemi K, Gathen V S der and Döbele H F 2001 Absolute calibration of atomic density measurements by laser-induced fluorescence spectroscopy with two-photon excitation *J. Phys. D: Appl. Phys.* **34** 2330–5, DOI: 10.1088/0022-3727/34/15/312

[128] Mrkvičková M, Ráheľ J, Dvořák P, Trunec D and Morávek T 2016 Fluorescence (TALIF) measurement of atomic hydrogen concentration in a coplanar surface dielectric barrier discharge *Plasma Sources Science and Technology* **25** 055015, DOI: 10.1088/0963- 0252/25/5/055015

[129] Duluard C Y and Aubert X 2019 Precautions for using krypton as a calibration species for Two-Photon Absorption Laser Induced Fluorescence of hydrogen and nitrogen atoms 13th Frontiers in Low-Temperature Plasma Diagnostics (Bad Honnef, Germany) p 1

[130] Preppernau B L, Pearce K, Tserepi A, Wurzberg E and Miller T A 1995 Angular momentum state mixing and quenching of n=3 atomic hydrogen fluorescence *Chemical Physics* **196** 371–81, DOI: 10.1016/0301-0104(95)00086-4

[131] van der Heijden H W P, Boogaarts M G H, Mazouffre S, van der Mullen J A M and Schram D C 2000 Time-resolved experimental and computational study of two-photon laser-induced fluorescence in a hydrogen plasma *Physical Review E* **61** 4402–9, DOI: 10.1103/PhysRevE.61.4402

[132] Gicquel A, Chenevier M, Hassouni Kh, Tserepi A and Dubus M 1998 Validation of actinometry for estimating relative hydrogen atom densities and electron energy evolution in plasma assisted diamond deposition reactors *Journal of Applied Physics* **83** 7504–21, DOI: 10.1063/1.367514

[133] Broc A, De Benedictis S and Dilecce G 2004 LIF investigations on NO, O and N in a supersonic N_2/O_2/NO RF plasma jet *Plasma Sources Sci. Technol.* **13** 504, DOI: 10.1088/0963-0252/13/3/017

[134] Marchal F, Merbahi N, Wattieaux G, Piquemal A and Yousfi M 2017 Measurements of Absolute Atomic Nitrogen Density by Two-Photon Absorption Laser-Induced Fluorescence Spectroscopy in Hot Air Plasma Generated by Microwave Resonant Cavity *JASMI* **07** 93–115, DOI: 10.4236/jasmi.2017.74008

[135] Kang N, Gaboriau F, Oh S and Ricard A 2011 Modeling and experimental study of molecular nitrogen dissociation in an Ar–N_2 ICP discharge *Plasma Sources Sci. Technol.* **20** 045015, DOI: 10.1088/0963-0252/20/4/045015

[136] Adams S F and Miller T A 2000 Surface and volume loss of atomic nitrogen in a parallel plate rf discharge reactor *Plasma Sources Sci. Technol.* **9** 248–55, DOI: 10.1088/0963-0252/9/3/302

[137] Bruggeman P J, Sadeghi N, Schram D C and Linss V 2014 Gas temperature determination from rotational lines in non-equilibrium plasmas: a review *Plasma Sources Science and Technology* **23** 023001, DOI: 10.1088/0963-0252/23/2/023001

[138] Šimek M 2014 Optical diagnostics of streamer discharges in atmospheric gases *J. Phys. D: Appl. Phys.* **47** 463001, DOI: 10.1088/0022-3727/47/46/463001

[139] Dekkar D, Puth A, Bisceglia E, Moreira P W P, Pipa A V, Lombardi G, Röpcke J, van Helden J H and Bénédic F 2020 Effect of the admixture of N_2 to low pressure, low temperature H_2-CH_4-CO_2 microwave plasmas used for large area deposition of nanocrystalline diamond films *J. Phys. D: Appl. Phys.* **53** 455204, DOI: 10.1088/1361-6463/aba7df

[140] Zhao T-L, Xu Y, Song Y-H, Li X-S, Liu J-L, Liu J-B and Zhu A-M 2013 Determination of vibrational and rotational temperatures in a gliding arc discharge by using overlapped molecular emission spectra *J. Phys. D: Appl. Phys.* **46** 345201, DOI: 10.1088/0022- 3727/46/34/345201

[141] Laux C O, Gessman R J, Kruger C H, Roux F, Michaud F and Davis S P 2001 Rotational temperature measurements in air and nitrogen plasmas using the first negative system of N_2^+ *Journal of Quantitative Spectroscopy and Radiative Transfer* **68** 473–82, DOI: 10.1016/S0022-4073(00)00083-2

[142] Pipa A V 2004 *On Determination of the Degree of Dissociation of Hydrogen in Non-*

Equilibrium Plasmas by Means of Emission Spectroscopy (Greifswald: Ernst-Moritz-Arndt-Universität Greifswald)

[143] Goehlich A, Kawetzki T and Döbele H F 1998 On absolute calibration with xenon of laser diagnostic methods based on two-photon absorption *J. Chem. Phys.* **108** 9362–70

[144] Tachiev G I and Fischer C F 2002 Breit-Pauli energy levels and transition rates for nitrogen-like and oxygen-like sequences *A&A* **385** 716–23, DOI: 10.1063/1.476388

[145] Dzierżęga K, Volz U, Nave G and Griesmann U 2000 Accurate transition rates for the 5p-5s transitions in Kr I *Phys. Rev. A* **62** 022505, DOI: 10.1103/PhysRevA.62.022505

[146] Döbele H, Mosbach T, Niemi K and Schulz-Von Der Gathen V 2005 Laser-induced fluorescence measurements of absolute atomic densities: concepts and limitations *Plasma Sources Science and Technology* **14** S31, DOI: 10.1088\/0963-0252\/14\/2\/s05

[147] Agrup S, Ossler F and Aldén M 1995 Measurements of collisional quenching of hydrogen atoms in an atmospheric-pressure hydrogen oxygen flame by picosecond laser-induced fluorescence *Applied Physics B Lasers and Optics* **61** 479–87, DOI: 10.1007/BF01081277

[148] Chang R S F, Horiguchi H and Setser D W 1980 Radiative lifetimes and two-body collisional deactivation rate constants in argon for Kr(4p ^{5}5p) and Kr(4p ^{5}5p′) states *J. Chem. Phys.* **73** 778–90, DOI: 10.1063/1.440185

[149] Gazeli K, Lombardi G, Aubert X, Duluard C Y, Prasanna S and Hassouni K 2021 Progresses on the Use of Two-Photon Absorption Laser Induced Fluorescence (TALIF) Diagnostics for Measuring Absolute Atomic Densities in Plasmas and Flames *Plasma* **4** 145–71, DOI: 10.3390/plasma4010009

[150] Wiese W L, Smith M W and Glennon B M 1966 *Atomic Transition Probabilities. Volume I. Hydrogen through Neon,* (NATIONAL STANDARD REFERENCE DATA SYSTEM)

[151] Hofmann S, van Gessel A F H, Verreycken T and Bruggeman P 2011 Power dissipation, gas temperatures and electron densities of cold atmospheric pressure helium and argon RF plasma jets *Plasma Sources Science and Technology* **20** 065010, DOI: 10.1088/0963- 0252/20/6/065010

[152] Colina Delacqua L 2012 *Modélisation/diagnostic de production de poussières dans un plasma H2 au contact d'une cible C/W. Contribution à l'étude des interactions plasma/surface dans les machines de fusion thermonucléaire.* (Université Paris 13)

[153] Venkateshan S P 2015 *Mechanical Measurements* (John Wiley & Sons), ISBN: 978- 1-119-11558-8

[154] Wolberg J 2006 *Data Analysis Using the Method of Least Squares: Extracting the Most Information from Experiments* (Springer Science & Business Media), ISBN: 978-3-540- 31720-3

[155] Annaloro J 2013 *Elaboration of collisional-radiative models applied to atmospheric entry*

into the Earth and Mars atmospheres (Université de Rouen)

[156] Guerra V, Tejero-del-Caz A, Pintassilgo C D and Alves L L 2019 Modelling N_2–O_2 plasmas: volume and surface kinetics *Plasma Sources Sci. Technol.* **28** 073001, DOI: 10.1088/1361-6595/ab252c

[157] Hassouni K, Gicquel A, Capitelli M and Loureiro J 1999 Chemical kinetics and energy transfer in moderate pressure H_2 plasmas used in diamond MPACVD processes *Plasma Sources Sci. Technol.* **8** 494–512, DOI: 10.1088/0963-0252/8/3/320

[158] Laricchiuta A 2012 The Phys4Entry database *APS Annual Gaseous Electronics Meeting Abstracts* APS Meeting Abstracts

[159] Biagi S *Fortran program, MAGBOLTZ, versions 8.9 and after*

[160] Bacri J and Medani A 1982 Electron diatomic molecule weighted total cross section calculation: III. Main inelastic processes for N_2 and N_2^+ *Physica B+C* **112** 101–18, DOI: 10.1016/0378-4363(82)90136-X

[161] Wang Y, Zatsarinny O and Bartschat K 2014 B -spline R -matrix-with-pseudostates calculations for electron-impact excitation and ionization of nitrogen *Physical Review A* **89** 062714, DOI: 10.1103/PhysRevA.89.062714

[162] Teulet P, Sarrette J P and Gomes A M 1999 Calculation of electron impact inelastic cross sections and rate coefficients for diatomic molecules. Application to air molecules *Journal of Quantitative Spectroscopy and Radiative Transfer* **62** 549–69, DOI: 10.1016/S0022-4073(98)00129-0

[163] Annaloro J, Bultel A and Omaly P 2014 Collisional-Radiative Modeling Behind Shock Waves in Nitrogen *Journal of Thermophysics and Heat Transfer* **28** 608–22, DOI: 10.2514/1.T4263

[164] Esposito F, Armenise I and Capitelli M 2006 N–N_2 state to state vibrational-relaxation and dissociation rates based on quasiclassical calculations *Chemical Physics* **331** 1–8, DOI: 10.1016/j.chemphys.2006.09.035

[165] Kossyi I A, Kostinsky A Y, Matveyev A A and Silakov V P 1992 Kinetic scheme of the non-equilibrium discharge in nitrogen-oxygen mixtures *Plasma Sources Sci. Technol.* **1** 207, DOI: 10.1088/0963-0252/1/3/011

[166] Kramida A and Ralchenko Y 2020 NIST Atomic Spectra Database

[167] Marinov D, Guaitella O, Arcos T de los, Keudell A von and Rousseau A 2014 Adsorption and reactivity of nitrogen atoms on silica surface under plasma exposure *J. Phys. D: Appl. Phys.* **47** 475204, DOI: 10.1088/0022-3727/47/47/475204

[168] Cartry G, Magne L and Cernogora G 2000 Atomic oxygen recombination on fused silica: modelling and comparison to low-temperature experiments (300 K)* *J. Phys. D: Appl. Phys.* **33** 1303–14, DOI: 10.1088/0022-3727/33/11/309

[169] Cartry G, Magne L and Cernogora G 1999 Atomic oxygen recombination on fused silica: experimental evidence of the surface state influence *J. Phys. D: Appl. Phys.* **32** L53–6, DOI: 10.1088/0022-3727/32/15/101

[170] Gordiets B, Ferreira C M, Pinheiro M J and Ricard A 1998 Self-consistent kinetic model of low-pressure - flowing discharges: II. Surface processes and densities of N, H, species *Plasma Sources Sci. Technol.* **7** 379–88, DOI: 10.1088/0963-0252/7/3/015

[171] Scott C D, Farhat S, Gicquel A, Hassouni K and Lefebvre M 1996 Determining electron temperature and density in a hydrogen microwave plasma *Journal of Thermophysics and Heat Transfer* **10** 426–35, DOI: 10.2514/3.807

[172] Brown P N, Byrne G D and Hindmarsh A C 1989 VODE: A Variable-Coefficient ODE Solver *SIAM J. Sci. and Stat. Comput.* **10** 1038–51, DOI: 10.1137/0910062

[173] Supiot P, Blois D, Benedictis S D, Dilecce G, Barj M, Chapput A, Dessaux O and Goudmand P 1999 Excitation of N2(B 3Πg) in the nitrogen short-lived afterglow *J. Phys. D: Appl. Phys.* **32** 1887–93, DOI: 10.1088\/0022-3727\/32\/15\/317

[174] Šimek M, DeBenedictis S, Dilecce G, Babický V, Clupek M and Sunka P 2002 Time and space resolved analysis of $N_2(C^3\Pi_u)$ vibrational distributions in pulsed positive corona discharge *J. Phys. D: Appl. Phys.* **35** 1981, DOI: 10.1088/0022-3727/35/16/312

[175] Lavrov B P, Pipa A V and Röpcke J 2006 On determination of the degree of dissociation of hydrogen in non-equilibrium plasmas by means of emission spectroscopy: I. The collision-radiative model and numerical experiments *Plasma Sources Science and Technology* **15** 135–46, DOI: 10.1088/0963-0252/15/1/020

[176] Biloiu C, Scime E E, Biloiu I A and Sun X 2007 Nitrogen dissociation degree in the diffusion region of a helicon plasma source obtained by atomic lines to molecular band intensities ratio *Journal of Applied Physics* **102** 053303, DOI: 10.1063/1.2777998

[177] Euler J, Ullrich J, Schmidt-Böcking H and Vogt H 1990 Determination of the degree of dissociation of an atomic hydrogen target by a recoil-ion time-of-flight method *Nuclear Instruments and Methods in Physics Research Section A: Accelerators, Spectrometers, Detectors and Associated Equipment* **287** 374–7, DOI: 10.1016/0168-9002(90)91550-U

[178] Monnin C F and Prok G M 1969 Energy transfer and ion cost in a hydrogen plasma 21

[179] Coquery F 2021 *Caractérisation spectroscopique et couplage thermique de plasmas micro-onde dans des capillaires* (Université Paris-Saclay)

[180] Treanor C E, Rich J W and Rehm R G 1968 Vibrational Relaxation of Anharmonic Oscillators with Exchange-Dominated Collisions *The Journal of Chemical Physics* **48** 1798–807, DOI: 10.1063/1.1668914

[181] Lofthus A and Krupenie P H 1977 The spectrum of molecular nitrogen *Journal of Physical and Chemical Reference Data* **6** 113–307, DOI: 10.1063/1.555546

[182] Guerra V and Loureiro J 1997 Electron and heavy particle kinetics in a low-pressure nitrogen glow discharge *Plasma Sources Science and Technology* **6** 361, DOI: 10.1088\/0963-0252\/6\/3\/013

[183] Zhu X-M and Pu Y-K 2010 Optical emission spectroscopy in low-temperature plasmas containing argon and nitrogen: determination of the electron temperature and density by the line-ratio method *J. Phys. D: Appl. Phys.* **43** 403001, DOI: 10.1088/0022-3727/43/40/403001

[184] Robert F, Tartèse R, Lombardi G, Reinhardt P, Roskosz M, Doisneau B, Deng Z and Chaussidon M 2020 Mass-independent fractionation of titanium isotopes and its cosmochemical implications *Nature Astronomy* **4** 762–8, DOI: 10.1038/s41550-020-1043-1

[185] Touchard S, Mougenot J, Rond C, Hassouni K and Bonnin X 2019 AMMONX: A kinetic ammonia production scheme for EIRENE implementation *Nuclear Materials and Energy* **18** 12–7, DOI: 10.1016/j.nme.2018.11.020

[186] Ouaras K 2016 *Mécanismes de formation et dynamique du transport des poussières de carbone et de tungstène dans un plasma Micro-Onde magnétisé et non-magnétisé* (Université Paris 13)

[187] Oberkofler M, Meisl G, Hakola A, Drenik A, Alegre D, Brezinsek S, Craven R, Dittmar T, Keenan T, Romanelli S G, Smith R, Douai D, Herrmann A, Krieger K, Kruezi U, Liang G, Linsmeier C, Mozetic M, Rohde V, team the A U, Team the Euro M and Contributors J E T 2016 Nitrogen retention mechanisms in tokamaks with beryllium and tungsten plasma-facing surfaces *Phys. Scr.* **2016** 014077, DOI: 10.1088/0031-8949/T167/1/014077

[188] Ogorodnikova O V, Sugiyama K, Markin A, Gasparyan Y, Efimov V, Manhard A and Balden M 2011 Effect of nitrogen seeding into deuterium plasma on deuterium retention in tungsten *Phys. Scr.* **2011** 014034, DOI: 10.1088/0031-8949/2011/T145/014034

[189] Ouaras K, Redolfi M, Vrel D, Quirós C, Lombardi G, Bonnin X and Hassouni K 2018 Tungsten Blister Formation Kinetic as a Function of Fluence, Ion Energy and Grain Orientation Dependence Under Hydrogen Plasma Environment *J Fusion Energ* **37** 144–53, DOI: 10.1007/s10894-018-0161-6

[190] Quiros C L 2017 *Bulk and surface modifications of metals submitted to hydrogen plasmas: the case of aluminum and tungsten*

[191] Kasri S, William L, Aubert X, Lombardi G, Tallaire A, Achard J, Lazzaroni C, Bauville G, Fleury M, Gazeli K, Pasquiers S and Sousa J S 2019 Experimental characterization of a ns-pulsed micro-hollow cathode discharge (MHCD) array in a N_2/Ar mixture *Plasma Sources Sci. Technol.* **28** 035003, DOI: 10.1088/1361-6595/ab0079

[192] Patnaik A K, Adamovich I, Gord J R and Roy S 2017 Recent advances in ultrafast-laser-based spectroscopy and imaging for reacting plasmas and flames *Plasma Sources Science and Technology* **26** 103001, DOI: 10.13039\/100006602

[193] Gazeli K, Aubert X, Prasanna S, Duluard C Y, Lombardi G and Hassouni K 2021 Picosecond two-photon absorption laser-induced fluorescence (ps-TALIF) in krypton: The role of photoionization on the density depletion of the fluorescing state Kr $5p'[3/2]_2$ *Physics of Plasmas* **28** 043301, DOI: 10.1063/5.0041471